DIRECT TORQUE CONTROL OF

BRUSHLESS DOUBLY FED RELUCTANCE MACHINES

A thesis submitted in partial fulfilment of the requirements of the

Northumbria University

For the degree of Doctor of Philosophy

By

Jian Yu

June 2004

Abstract

Theoretical and Experimental results of research on the Direct Torque Control (DTC) of the Brushless Doubly Fed Reluctance Machine (BDFRM) are presented in this thesis. The main motivation for this work has been found in the relative simplicity of the DTC strategy and attractive properties of the BDFRM drive, foremost its cost-effectiveness associated with the use of a partially rated power electronics, and reliability of brushless structure of the machine itself. It is hoped that the project outcomes will be extremely helpful to the further study of the machine in light of its application in wind power generation and/or large pump systems.

The thesis is essentially divided into three main parts. The first part is the theory development, which involves the analysis of the fundamental principles of DTC and BDFRM operation.

The second part presents the comprehensive simulation studies of the developed control scheme for the machine in both sensor and sensorless modes. The computer studies have been performed to examine the performance of the controller based on a linear (ideal) machine model. The parameters used for this model have been obtained by off-line testing of a small Axially Laminated BDFRM prototype at Northumbria University, UK.

The third part of the thesis contains a comprehensive set of experimental results that have successfully verified the control algorithm for the machine. Based on the Simulink® program, a Digital Signal Processor (DSP) control board from dSPACE® has been used to control a conventional IGBT inverter bridge.

Acknowledgements

There are many people to whom I should express my sincere and deep gratitude for their warm-hearted help and friendship during the course of my PhD research work.

I should first thank my supervisor, Dr. Milutin Jovanovic for scientific attitude and optimistic style that will influence me in the days to come. His invaluable support and knowledge in electrical drives area enabled the project to be finished on time.

I should thank Jie for her love, confidence and patience.

The friendly environment of the research group, the Senior and Junior research students, kept me looking at the bright side of life always. I should thank Mark Leach who is really an English gentleman, Chatchai, Mehash, Forag, Ng , Lee and all the others.

The effective technical support in the School of Engineering and Technology at Northumbria University is another important contributing element to the project success. Dr. Ghanium Putrus provided invaluable advices. Mr.Vince J Hinksman provided very useful suggestions and help in the hardware design and laboratory experiments. Mr. Glan Dawson and Mr. Denis Henderson helped enormously to mechanically couple and mount the drive system components. I would also like to sincerely acknowledge the staff members for their assistance.

Finally, special acknowledgements are due to the Engineering and Physical Science Research Council (EPSRC) for financial support (GR/N34550).

Contents

Nomenclature

'V_{dp}, V_{qp}' indicate the primary d and q voltage respectively;

'V_{ds}, V_{qs}' indicate the secondary d and q voltage respectively;

'ω, ω_r' indicate the angular velocity of reference frame and rotor speed respectively;

'ω_{rm}' is the rotor mechanical angular velocity, under steady state conditions when $\theta_{rm} = \omega_{rm} \cdot t$;

'p' is the primary stator winding pole number; 'q' is the secondary stator winding pole number; 'p_r' is the rotor pole number;

'$L_p, L_s and L_m$' are primary inductance, secondary inductance and mutual inductance;

'λ_p' is primary flux, 'λ_{pq}' is the primary q-axis flux, 'λ_{pd}' is the primary d-axis axis;

'λ_s' is secondary flux, 'λ_{sq}' is the secondary q-axis flux, 'λ_{sd}' is the secondary d-axis axis, 'λ_{st}' is secondary flux at instant time 't',' λ_{s0}' is secondary flux original value;

'δ' is the angle between secondary flux and secondary d-axis in its own frame;

'F( )' is the winding revolving MMF per air gap;

' R_p' primary stator resistance, ' R_s' secondary stator resistance;

' i_p' primary stator current; ' i_{pd}' primary stator current along d-axis; ' i_{pq}' primary stator current along q-axis;

' i_s' secondary stator current, ' i_{sd}' secondary stator current along d-axis; ' i_{sq}' secondary stator current along q-axis;;

'T_e' electro-magnetic torque;

's' slip;

'$\mathbf{u}_p$' primary voltage vector, '$\mathbf{u}_s$' secondary voltage vector

Chapter 1 Introduction

This thesis is primarily concerned with the Direct Torque Control (DTC) of a Brushless Doubly Fed Reluctance Machine (BDFRM), both with and without a shaft position sensor. The BDFRM design is quite unusual in the sense that its stator has two stator windings with different pole numbers and different applied frequencies. One winding, known as primary or power winding, is connected directly to a fixed voltage and frequency mains supply, while the other, called the secondary or control winding, is inverter fed. However, as a member of the reluctance machine family, it is named after its reluctance rotor structure. A reluctance machine normally develops its electromagnetic torque because of the tendency of the rotor to take up a minimum reluctance position for the stator flux. This position occurs when the high permeance rotor axis (termed as the d-axis) is aligned with the stator field axis.

The first section of this chapter gives a brief induction of machine design characteristics. While the detailed machine review will be elaborated in Chapter 2, different rotor structures are shown in this section. In section 1.2. the mathematic process leading to the frequency relationship is shown. The problem formation of this project is given in section 1.3. This list will work effectively as the benchmark in project management. The thesis contribution can be found in 1.4. This section concludes some obvious achievements during and after the project is successfully

conducted. To make it easier for the reader, section 1.5. outlines the main content for the following chapters.

1.1 Machine Design Characteristics

Research on the Synchronous Reluctance Machine (Syncrel) [1,2] has shown that two crucial parameters that determine the machine performance are: L_d / L_q and $L_d - L_q$ (L_d and L_q are the inductances along d-axis and q-axis respectively). In order to optimise the machine operation, the rotor should be designed with maximum L_d and minimum L_q as this condition allows the above parameters to be as large as possible. Evolution of reluctance rotors has been an effort to accomplish this goal.

While the rotor optimum design aspects are out of the scope of this thesis, it is necessary to provide a brief discussion of various Syncrel rotor configurations that can be equally used for the BDFRM.

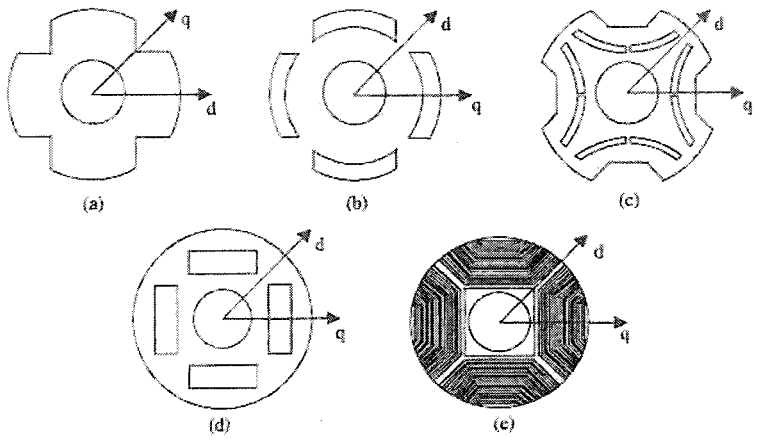

Figure 1.1 Four-pole rotor designs: (a)Conventional salient pole; (b) Segmental; (c) Double barrier; (d) Single barrier;(e) Axially laminated [1, 4]

Compared with other structures shown in Figure 1.1, an Axially Laminated Anisotropic (ALA) rotor (corresponding 'e' in Figure 1.1) can achieve very high values of saliency ratio [1,2]. The ALA rotor (Figure 1.2) is made of multiple thin aluminium sheets interleaved with insulation material. A large number of flux barriers are perpendicular to the low permeance q-axis resulting in most of the flux being guided along the high permeance d-axis. This flux path leads to a reduction of L_q but also to an increase of L_d.

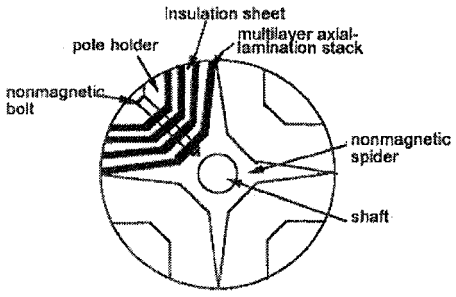

Figure 1.2 The configuration of Axially Laminated Anisotropic (ALA) rotor [1]

The special structure of BDFRM makes the field distribution in the air-gap complicated. There have been many attempts to understand the magnetic field behaviour; the latest works have been carried out using the Finite Element (FE) method[3]. Unlike a conventional designed machine, it is possible for a BDFRM to have odd number rotor poles. For example, analysis of the flux distribution in a 3-pole rotor BDFRM is given in [3]. Figure 1.3 shows that there is sinusoidal variation of machine mutual inductances with rotor position despite the non-sinusoidal air-gap flux density.

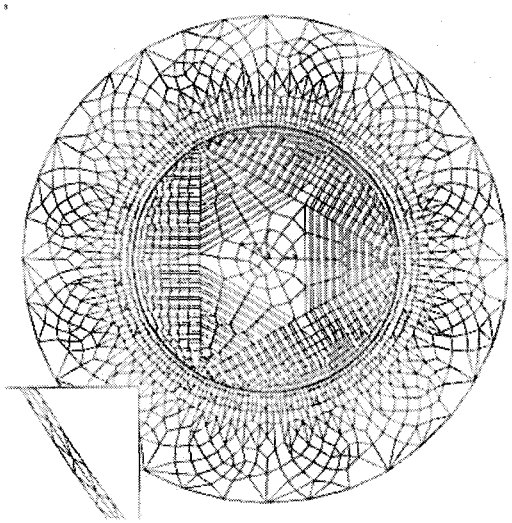

Figure 1.3 The Finite element analysis of flux distribution [3]

Unlike traditional AC machines, such as induction or synchronous machines, the BDFRM has an air-gap field distribution, which comes from the interaction of two revolving fields of different pole numbers modulated through the rotor saliency. These two fields are synchronous with respect to a rotor observer in such a way that the peak of the two Magneto-Motive Force (MMF) waves coincide periodically on a pair of rotor poles. It is seen that local saturation occurs on all of these occasions. Therefore cross coupling will be created between magnetizing and torque producing currents.[3]

There are two types of flux linkages particularly associated with the BDFRM, these are self and mutual flux linkages. In principle, the self flux linkage is used to measure the flux generating capability of the windings. The mutual flux linkage is used to measure the degree of mutual coupling between the two stator-windings. It can be seen from paper [3] that the self flux linkage is almost constant for a 6-pole stator

winding while the mutual flux linkage for the 2-pole stator winding varies as a sinusoid according to the rotor position.

1.2 Basic Frequency Relationships

The fundamental principles of BDFRM operation and its torque production [2,4,5] are quite unusual and interesting and are considered in this section. It will be shown in Chapter 2 that there is close similarity between BDFRM and Brushless Doubly Fed Induction Machine (BDFIM) even in frequency relationships[7,12,15,17]. The details of the *dq*-axis machine model will be the topic of Chapter 3. The relationship between the stator windings' frequencies and rotor speed are of primary concern of this section. Flux density distributions $B(\theta,\theta_{rm})$ can be calculated for each of the two windings using the following well-known expression [4]:

$$B(\theta,\theta_{rm}) = \mu_0 g^{-1}(\theta,\theta_{rm})F(\theta) \tag{1.2}$$

where $F(\ )$ is the winding revolving MMF per air gap, θ is the angle around the stator circumference and the subscript '*rm*' denotes the rotor mechanical angle. The stator and rotor angles have been defined with respect to the same reference point i.e. the phase-a axis for example.

The generic inverse air gap function in (1.2) can be expressed as [4]:

$$g^{-1}(\theta,\theta_m) = \frac{G}{2}[1+\cos p_r(\theta-\theta_{rm})] \tag{1.3}$$

where p_r is the number of rotor poles (not pole-pairs) and G is some constant dependent on the machine design parameters.

The above expression is an approximation [4]. By substituting (1.3) together with the conventional expression for the resultant MMF into (1.2), the primary winding flux density distribution can be obtained:

$$B_p(\theta,\theta_{rm}) = \mu_0 \frac{G}{2}[1+\cos p_r(\theta-\theta_{rm})][F_{pm}\cos(\omega_1 - p\theta)]$$
$$= \frac{\mu_0 G F_{pm}}{2}[\cos(\omega_1 t - p\theta) + \cos(\omega_1 t - p\theta)\cos p_r(\theta-\theta_{rm})] \quad (1.4)$$

After trigonometric manipulation, the above expression can be rearranged into the following form:

$$B_p(\theta,\theta_{rm}) = \frac{\mu_0 G F_{pm}}{2}[\cos(\omega_1 t - p\theta) + \frac{1}{2}\cos(\omega_1 t - p\theta + p_r(\theta-\theta_{rm}))$$
$$+\frac{1}{2}\cos(\omega_1 t - p\theta - p_r(\theta-\theta_{rm}))] \quad (1.5)$$

Since $\theta_{rm} = \int \omega_{rm} dt$, where ω_{rm} is the rotor mechanical angular velocity, under steady state conditions when $\theta_m = \omega_{rm} \cdot t$, (1.5) can be further simplified as:

$$B_p(\theta,\theta_{rm}) = \frac{\mu_0 G F_{pm}}{2}\{\cos(\omega_1 t - p\theta) + \frac{1}{2}\cos[(\omega_1 - p_r\omega_{rm})t - (p-p_r)\theta]$$
$$+\frac{1}{2}\cos[(\omega_1 + p_r\omega_{rm})t - (p+p_r)\theta]\} \quad (1.6)$$

There are three terms on the right hand side of (1.6). The first one is clearly the fundamental component, but unlike a conventional machine, this is not rotor position dependent and as such does not couple with the complementary winding MMF of different pole numbers and angular velocity. Therefore this parasitic component appears as leakage in the machine and does not participate in the electromechanical energy conversion. This is certainly one of the serious limitations of the machine,

which results in relatively weak magnetic coupling between the windings and modest torque production [3,4,7].

The other two components of (1.6) are the harmonic side-bands rotating at $\omega_1 - p_r\omega_{rm1}$ and $\omega_1 + p_r\omega_{rm1}$ respectively. The relative direction of rotation of these components depends on the specific values of the pole numbers and the angular velocity of the rotor. More importantly, they are rotor position dependent which is a pre-requisite for torque to be produced from the machine. However, in order for this to occur the rotor pole number and velocity must be such that there is a frequency match in both temporal and spatial terms with the complementary winding MMF. Issues related to this are discussed in the following.

A similar derivation procedure can be carried out for the secondary winding. The resultant flux density distribution in this case is (ignoring phase angles for convenience of this semi-heuristic analysis):

$$\begin{aligned} B_s(\theta,\theta_{rm}) &= \frac{\mu_0 GF_{sm}}{2}[\cos(\omega_2 t - q\theta) + \frac{1}{2}[\cos(\omega_2 t - q\theta + p_r(\theta - \theta_{rm})) \\ &+ \cos(\omega_2 t - q\theta - p_r(\theta - \theta_{rm}))] \\ &= \frac{\mu_0 GF_{sm}}{2}[\cos(\omega_2 t - q\theta) + \frac{1}{2}[\cos((\omega_2 - p_r\omega_{rm})t - (q - p_r)\theta) \\ &+ \cos((\omega_2 + p_r\omega_{rm})t - (q + p_r)\theta)] \end{aligned} \tag{1.7}$$

There is obviously a close similarity between (1.6) and (1.7). The resultant secondary flux density waveform can be again resolved into a fundamental (leakage) component plus two harmonic side-bands.

Under certain rotor speed and pole number combinations, one of the two side-bands for each of the windings will couple with the complementary winding fundamental MMF. Consider, for instance, the first harmonic component of the primary winding flux density in (1.6). The following relationship must be satisfied:

$$\cos((\omega_1 - p_r\omega_{rm})t - (p - p_r)\theta) \quad = \cos(\omega_2 t - q\theta) \tag{1.8}$$

By equating the temporal and spatial terms in (1.8), it follows that:

$$\omega_1 - p_r\omega_{rm} = \omega_2 \text{ if } p - p_r = q \tag{1.9}$$

Or $\omega_1 - p_r\omega_{rm} = -\omega_2$ if $p - p_r = -q$

This leads to the following conditions:

$$\omega_{rm} = \frac{\omega_1 - \omega_2}{p_r} \text{ and } p_r = p-q \tag{1.10}$$

or

$$\omega_{rm} = \frac{\omega_1 + \omega_2}{p_r} \text{ and } p_r = p+q \tag{1.11}$$

The angular velocity and pole number relationships contained in (1.10) are almost never encountered in practice as the rotor pole number can end up being negative if p

< q which physically does not make sense. The same conditions can be derived looking at the secondary winding quantities. Therefore, the conditions for the machine torque production are represented by (1.11). The same angular velocity relationship in (1.11) applies to a conventional cascaded induction machines [10,12].

1.3 Problem Formulation

The purpose of this Section is to identify the tasks to be completed as part of this project. The work is divided into two categories: one contains theoretical problems and the other practical problems. The first group of problems is concerned with theoretical aspects of DTC. The difficulty here is in the BDFRM untraditional structure and unusual torque producing mechanism, which impose some necessary deviations from a traditional DTC approach. The key point of this topic is therefore the extension of the fundamental DTC principle to the BDFRM case. In keeping with this, issues related to torque and flux estimation as well as look-up tables for optimal inverter switching, have been addressed in detail.

The second group of problems deals with the development and experimental verification of the Direct Torque Control algorithms developed as a result of the theoretical analysis of the test machine. The effective solution of these problems would make it possible to apply the DTC to the BDFRM either with or without a shaft sensor.

1.3.1 SUMMARY OF THE PROJECT TASKS

Having read the relevant literature on the subject, the following important observations about the project and the necessary steps for its successful completion can be made:

1. The DTC theory for the BDFRM. Most concerns of industrial and research community about DTC implementation are focused on conventional single fed machines at the moment. The principle of torque production of a BDFRM is different due to its structural characteristics and unusual operation. Therefore, some modifications of the traditional DTC concept, which is very well elaborated in the literature and can be found in many text-books, are to be made in order to be able to successfully apply DTC to the BDFRM. To achieve this, an optimal switching-table based DTC strategy for a BDFRM needs to be generated. It is envisaged that hysteresis flux and torque control will be used to fire the inverter in conjunction with the table created.
2. Modelling of the machine. There are generally two ways of representing the dynamic model equations for the machine - one can either use three-phase or D-Q quantities. The latter approach will be adopted as it provides fewer rotor-position independent variables in the equations than the three-phase one and as such is computationally less intensive. Consideration of the saturation and iron losses of the real machine is out of scope of this project. It should be

mentioned however that parameter variations due to saturation effects are small in this particular machine because of its nearly constant flux operation.

3. The starting procedure. Soft starting is required to prevent overloading of a partially rated inverter during start-up. The starting method will first be simulated in software and then practically implemented on a real system.
4. Development of a suitable model-based rotor speed (position) estimation algorithm. It is intended to design a viable weakly parameter dependent method that performs well down to zero speed with no voltage integration problems.
5. Simulations. Since there is very little or no previously published work on the DTC application to the BDFRM, computer simulations are a necessary tool at an early stage of the project to test the developed DTC algorithm for the machine. A Simulink® programme will be created to test the BDFRM behaviour under the developed DTC in both 'sensor' and closed loop sensorless speed control modes.
6. Real-time implementation. After making sure that the DTC algorithm is fully operational in simulations, the controller for real time implementation of the control has to be developed. The use of a dSPACE® platform for this purpose has significantly increased the portability of the controller simulation code owing to its compatibility with Matlab®/Simulink® environment. Despite this convenience, some adaptations of the Simulink® programme are still necessary to enable the controller simulator to be used and work well in real

time. It is understood that practical effects, such as noise, measurement quantisation and DC offset, may have an adverse impact on the controller performance. The controller should therefore be designed to be as robust as possible.

7. Peripheral Interfaces. Interfaces between the dSPACE® I/O box and other hardware components i.e. inverter, shaft position encoder, and voltage/current transducers, have to be carefully designed and co-ordinated in such a way that actual samples of analogue measurements can be fed into a CPU for further processing and/or control calculations.

1.4 Thesis Contributions

The main contributions of this thesis are:

1. Scalar control of BDFRM is successfully achieved. The material has not been published before this work is done. The simple close-loop scalar control is used to verify the machine model. Some related aspects such as stable region are analysed.
2. Maximum Torque per Secondary Ampere (MTPSA) DTC strategy for the BDFRM is developed. General control-form expressions for the BDFRM that can serve for development of optimal conditions for the other control

properties of interest are derived using an ideal d-q model. A new estimation technique for control (secondary) flux estimation has been proposed.

3. Comprehensive computer studies of the DTC algorithm are carried out using the MTPSA control strategy as an example in order to confirm the DTC principles and optimum control aspects over the entire speed range and under various loading conditions of the BDFRM. This analysis has particularly focused on the DTC performance at low secondary frequencies down to zero when the machine is running at synchronous speed. Different switching strategies were compared and a simplified look-up table was verified to improve the transient response. The parameters obtained experimentally for the BDFRM 'proof-of-concept' machine are used for the simulation studies, and before these were made available, data published in [22] had served for this purpose.
4. The Simulink® program is adapted for real time software implementation using the dSPACE® system. The functional description of the control code developed and the experimental results generated on an axially laminated DBFRM prototype are given in Chapter 7. The controlled machine is shown to be capable of quality speed control: below, at and beyond synchronous speed.

The most significant contribution of the thesis is the development of a new DTC controller for the BDFRM that is capable of providing good machine performance down to synchronous speed (when the secondary winding is DC fed). The same

algorithm can largely be applied to double-excited wound rotor induction machines as well. This or similar kind of work for this particular machine or any other doubly-fed variable speed drive system has not been reported in the literature published to date. It is important to stress the fact that the developed DTC scheme has allowed the BDFRM to operate successfully at zero supply frequency of the secondary winding this being impossible to achieve with cage induction machines.

1.5 Thesis Outline

The remainder of the thesis is organised as follows:

- **Chapter 2** gives a critical review of the key papers published on the BDFRM and DTC technology in general. The emphasis here is more on the existing BDFRM work related to control, rather than design aspects.
- **Chapter 3** is the introductory part of mathematical machine model built in Simulink®. The model is used to design a scalar control algorithm for the machine, which has been subsequently tested by computer simulations.
- **Chapter 4** provides an understanding of the DTC principles in the BDFRM case. A traditional look-up table for cage induction machines has been used as a benchmark for the studies. The chapter also presents a proposed control scheme.
- **Chapter 5** presents a rotor position estimation technique and an angular velocity observer based sensorless algorithm for closed-loop speed control.
- **Chapter 6** intends to improve the machines dynamics by some modification of the traditional switching strategies. Special attention is paid to the impact of these

strategies on machine performance at synchronous speed. The simulation works as an effective tool to compare the results.

- **Chapter 7** describes in detail the main components of the BDFRM DTC controller simulator. Simulation results are presented for the Maximum Torque per Secondary Ampere (MTPSA) control methodology for both position sensor and sensor-less modes.
- **Chapter 8** addresses real-time implementation issues and describes the development of an experimental digital controller derived from the simulator design. The hardware components are introduced. A set of experimental results generated by executing the control algorithm is shown.
- **Chapter 9** concludes the thesis by giving conclusions and making some recommendations for future work.
- **Appendix A** considers various hardware components and the off-line testing methods for the identification of the test-machine parameters.
- **Appendix B** is a detailed description of the PC interface board - DS1103 from dSPACE®. The signal Input/Output interface is explained.
- **Appendix C** presents experimental hardware system photographs.
- **Appendix D** lists published papers those the thesis writer co-authored related to this project.

Chapter 2 Literature Review

The purpose of this Chapter is to give a critical appraisal of the most important work that has been published on the subject. A relatively limited number of papers have appeared in the relevant literature mainly due to the originality and uniqueness of the topic. Given the project title, the source of the papers is found in the two distinctive areas: one is about the Brushless Doubly Fed Reluctance Machine (BDFRM) itself, and the other is on the Direct Torque Control (DTC). Since Takahashi and Noguchi first proposed a DTC algorithm for the cage induction machine in 1985 [8], this control method has become an active research field and it has been successfully applied to almost all AC machines, but not to the BDFRM. It is even claimed to be the trend of control of AC drives after the company ABB produced the first commercial DTC induction machine in 1995 [9]. On the contrary, the amount of work published on the BDFRM to date is relatively small despite the fact that the basic operating principles of the machine have been established back in the early 1970's [10]. It is only in the last decade that the BDFRM has started receiving an increasing attention by the research and industrial community largely owing to its slip power recovery nature and the possibility of using a smaller inverter especially in applications with restricted speed ranges.

2.1 *BDFRM Literature Review*

2.1.1 INTRODUCTION TO BDFRM

The Brushless Doubly-Fed Machine (BDFM) is a descendent of the classic cascaded induction machines (Figure 2.1). This very old technology [14] was primarily developed to achieve low speed, high torque drives with some variable speed capability and the reliability of brushless structure. The two wound rotor machines, generally of different pole numbers, were mechanically coupled which allowed their rotor windings to be connected directly without brushes or slip rings (these are shown in Figure 2.1 just to indicate electrical connections of the rotors). In the original implementation [14], the speed control was obtained by external resistance variations in the stator circuit of the secondary 2q-pole machine, this effectively changing the perceived rotor resistance as seen by the primary (grid connected) 2p-pole machine.

If the stators are supplied with the frequencies f_p and f_s respectively, then the cascaded configuration is operated in the so called 'synchronous' mode at the shaft velocity of $\omega_r = 2\pi(f_p + f_s)/(p+q)$ [14]. Therefore, in a modern set-up where the 2q-pole machine is inverter fed (Figure 2.1), the speed can be controlled from zero up to the rated value by varying the corresponding frequency input f_s from $-f_p$ (the '-' sign denotes the opposite phase sequence) to the mains frequency f_p [4,7]. Apart from the absence of brush gear and associated problems, another advantage of this solution is the possibility of using a partially rated power electronic converter as this

machine only needs to process the slip power generated by the primary machine rotor. However, these good features seemed to be offset by serious limitations such as the bulky and costly construction and poor efficiency, all resulting from the requirement for the two machines operating at high slips (especially the primary one). Consequently, while intellectually interesting the traditional cascaded machines have been of little practical importance.

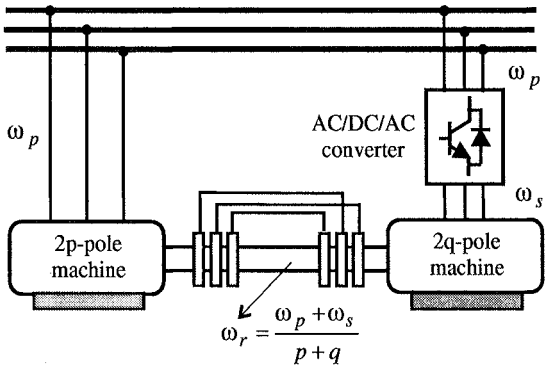

Figure 2.1 Double excited cascaded induction machine

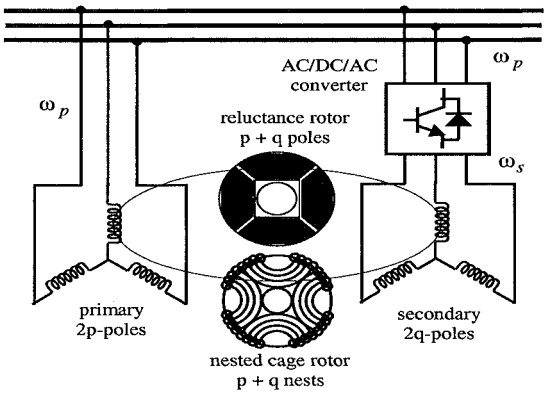

Figure 2.2 Brushless doubly fed machines (BDFMs)

The previous shortcomings have stimulated research into a more compact cascaded machine design and led to the Hunt's invention of the so-called self-cascaded machine at the turn of the last century [16]. The self-cascaded machine, similar to the cascaded

machine mentioned previously, is targeting medium and high power applications where limited speed variation is required and where the cost of power electronics is significant. The main idea was to build the two machines in the cascaded arrangement into the same frame by placing two separate windings of different pole numbers into the stator slots. This approach also involved a complicated wound rotor design to provide magnetic coupling between the stator windings. The Hunt's basic concept was later further extended [10] with the development of a new mixed-pole single stator winding, capable of simultaneously performing the dual winding function, and a special cage-type rotor of the "nested-loop" structure (Figure 2.2). These machines are now commonly known as Brushless Doubly-Fed Induction Machines (BDFIMs). Broadway [10] also investigated the use of a cageless axially-laminated rotor (Figure 2.2) and established the fundamental operating principles of another variant of the BDFM – the Brushless Doubly Fed Reluctance Machine (BDFRM). However, due to the lack of reliable power electronics, associated processor hardware and adequate mathematical models, the BDFMs were largely ignored until the 1990s.

The advent of fast microprocessors has opened up opportunities for better control and utilization of machines and contributed foremost to the revival of interests in the BDFMs mostly in the USA [17-26]. The significant work, done in the UK by Williamson *et al.* [27, 28], is related to the BDFIM only. D. Atkinson *et al.* [12,31] have made a comprehensive analysis of the field oriented control of the BDFIM, both theoretically and practically. A general theory [27,28,33], appropriate d-q models

[2,17,22] and vector control algorithms [12,17,18] based on these models have been developed and experimentally verified for both the BDFIM and the BDFRM. Despite the peculiar torque producing mechanism [29,34], which is quite distinct from their ancestor, the cascaded induction machine (Figure 2.1), the BDFM speed can still be represented using the same relationship. However, in order to achieve magnetic interaction between the stator windings, the number of nests (BDFIM) i.e. poles (BDFRM) on the rotor have to be half the total number of stator poles as illustrated in Figure 2.2. Therefore, unlike a conventional machine, the rotor may have an odd pole number if, for instance, the stator is equipped with 4/2 pole windings [24]. Yet, a BDFM with a 6/2 stator and a 4-pole rotor is the most frequent design reported in the published literature.

The main motivation for the recent growing attention to the BDFMs has been primarily found in the following:

- The cost of power electronic hardware (especially in larger drives) is often the dominant component of a total system cost. The fact that the supply converter has to handle only the slip power implies the possibility for considerable capital cost savings. It has been preliminary estimated that for the same power output these can be even 30% lower compared to a standard cage induction machine with a fully-rated inverter [3].

- Apart from the clear economic benefits, the BDFM has several other advantages over singly excited machines: (a) it can operate in sub-synchronous and super-synchronous modes in both motoring and generating regimes; and (b) it posses one more degree of freedom in control and performance parameter optimisation.

- In contrast to the static Kramer or Scherbius systems based on a doubly excited slip-ring induction machine [27,28], the BDFRM is brushless and thus more reliable, mechanically robust and requires lower maintenance. It has also a 'fail-safe' induction machine operating mode in case of the converter breakdown.

While both BDFM versions, the BDFIM and the BDFRM, share all the above salient features, the focus of this project is on the BDFRM as this machine has some additional favourable properties that make it superior in many respects to the BDFIM. These are:

1. The possibility of using a synchronous reluctance machine (SyncRel) rotor should offer the BDFRM the greater efficiency, the improved reliability and much easier control with respect to the BDFIM (control related issues will be addressed in more detail in the next section). Among various rotor forms [24],

an axially laminated design (Figure 2.2) gives the best performance as it does with the SyncRel [1,4,23].

2. The BDFRM operation is stable over the entire speed range whereas the BDFIM suffers from the inherent stability problems around the synchronous speed of the mains field when it produces no torque [19].

The previous virtues have made the BDFRM an ideal candidate and a viable alternative to wound rotor induction machines for large pumps (and similar applications) where the speed ranges required are relatively limited (typically 2:1 or less) [18]. The use of the BDFRM in these applications usually means the increased size of the machine itself [4,17], but this deficiency is in most cases more than compensated by the improved efficiency and considerable cost reduction of the feeding converter whose rating can be lowered to 25% that of the machine.

Another equally relevant application area, that has been intensively considered recently, is variable speed, constant frequency (VSCF) wind-power generation in both grid-connected [26] and stand-alone autonomous systems [25]. In these applications, the variable speed operation of the machine allows improved energy capture from the wind and superior turbine efficiency. Most VSCF wind turbine installations today mostly employ squirrel-cage induction generators connected to >100% rated converters. The advantages of using the BDFRM with a partially rated (about 25% as

for pump-type drives) power electronic hardware would be manifold: (a) competitive performance can be achieved at decreased capital cost; (b) both optimum wind energy capture and maximum power output (efficiency) are possible; (c) possibility of utility power factor correction avoiding shunt capacitors (in this case, however, a larger inverter would be needed); (d) improved power quality and lower line filtering requirements can be accomplished in grid connected systems as less harmonics are injected into the supply by the power electronics. It is recognised that conventional Doubly-Fed Induction Generator is now widely used in wind power generation due to its mature manufacture techniques.

2.1.2 PROJECT SCIENTIFIC/TECHNOLOGICAL RELEVANCE

The existing work on the BDFMs has been mainly of purely research nature and the 'proof-of-concept' machines have not seen any significant industrial use so far. An exception is the 45 KW pump drive in a waste-water treatment plant where a BDFIM prototype has replaced a wound-rotor induction motor with liquid rheostats [25]. For this and other non-demanding 'niche' markets, the BDFM technology is primarily targeted at, simple but sluggish closed-loop scalar control of speed and grid power factor (or some other performance indicator, usually efficiency) implemented on low cost micro-controllers seems to be a satisfactory solution since a fast dynamic response is not an imperative [25]. Nevertheless, as instability may occur if the inverter frequency (that can be estimated using the speed-frequency relationship introduced earlier) is changed too fast, field oriented control methods are generally

needed for higher performance applications [12,17,18]. In this sense, however, the BDFIM is not a preferable option due to: (a) the d-q model complexity imposed by the three-winding structure [10,27,28] and (b) consequent complicated, heavily parameter dependent and computationally intensive schemes requiring lower DSP control rates with compromised control quality [19].

The BDFM's reluctance form, the BDFRM, is believed to overcome all the above deficiencies thus increasing the machine's potential applicability and making it more attractive to industry. Apart from the higher efficiency, the principal advantage of the BDFRM over the BDFIM is the control simplicity resulting from the double winding design. More importantly, control of torque and primary winding reactive power is inherently decoupled and additional predictive algorithms, normally present with conventional vector controllers, are therefore not necessary [17]. It should be emphasised that the same holds for a doubly excited wound rotor induction machine (DEWRIM) since this has essentially identical d-q model [17,22] and can use similar control strategies as the BDFRM [19,22]. B.Hopfensperger and D.J. Atkinson gave comprehensive comparisons between doubly-fed machine in terms of their modelling similarity [13].

2.1.3 CONTROL ASPECTS OF THE BDFRM

Control methods for the BDFRM have been systematically reviewed and various control strategies for optimum machine performance proposed by Dr. Jovanovic and

his colleagues [33, 34, 60]. Xu and his group have published a significant amount of both theoretical and practical work on vector control of the machine in both motoring and generating regimes [3,17,22,26]. Many other authors have also followed this route [12,18, 22]. As previously mentioned, one of the most important advantages of the BDFRM and the DEWRIM compared to other machines with field-oriented control is that the expressions for torque and primary winding power factor are inherently decoupled.

When it comes to modelling aspects of the BDFRM, several important papers have also been published and different dynamic models have been proposed [17,18,19,20,21]. For example, O.Ojo and Z.Wu [21] have used the harmonic balance concept and the Manley-Rowe power frequency relationships (which consider harmonic energy) to derive the model equations. The main contribution of the paper is the consideration of the influence of magnetic saturation and core loss. The authors have also developed a close-loop speed control algorithm and have verified its performance both by simulations and experimentally. They have also performed stability studies of the machine operation under the conditions of this simple control method.

There is no doubt that most of the published work on the BDFRM control has been concerned with vector control, and for this reason, the fundamentals of this popular control method from a BDFRM point of view are reviewed in the following. Issues

related to scalar control, not previously been published, have been addressed in more detail in Chapter 3 mainly because of the suitability of this low-to-medium performance method for general-purpose applications and pump-drives.

The field-oriented control (FOC) for the BDFRM, as for any other machine, is based on desired positioning of the controllable secondary current vector in a d-q rotating reference frame. Therefore, one needs to control the respective d-q current components so that a particular performance parameter of the machine is optimised. The expressions relevant for the control are usually derived using a dynamic model of the machine[17,22]. It can be shown that in case of the primary flux oriented FOC (i.e. with the reference frame aligned with the primary flux vector) the active and reactive power of the primary winding can be expressed as [17,22,33]:

$$T_e = \frac{P_{out}}{\omega_{rm}} = \frac{3}{2} p_r \frac{L_{ps}}{L_p} \lambda_p i_{sq} \tag{2.1}$$

$$P = -1.5 \frac{L_{ps}}{L_p} \omega_p \lambda_{pd} i_{sq} \tag{2.2}$$

$$Q = 1.5 \frac{1}{L_p} \omega_p \lambda_{pd} (\lambda_{pd} - L_{ps} i_{sd}) \tag{2.3}$$

where λ_p is primary flux in stationary frame; λ_{pd} is d-axis component of primary flux; L_p is primary inductance; L_{ps} is mutual inductance; i_{sd} is the d-axis component of secondary current ; i_{sq} is the q-axis component of secondary current.

The above equations imply that the reference frame d-axis is locked with the primary winding flux (λ_p is fixed, line frequency and of approximately constant magnitude

due to the winding grid connection) and i_{sd} and i_{sq} are the controllable secondary current components lying along and orthogonal to λ_{pd} respectively (note that $\lambda_p = \lambda_{pd}$ i.e. $\lambda_{pq} = 0$) It is important to stress the fact that there is obviously no coupling between the expressions of real power and reactive power. This significantly facilitating the FOC scheme as additional decoupling techniques are not required.

The maximum torque per secondary ampere (MTPSA) is achieved if $i_{sd} = 0$ i.e. $i_{sq} = i_s$ and under these conditions the inverter current loading is the minimum possible for a given torque. Q_p is regulated by the amount of flux that is being produced in the primary via the mutual coupling from the secondary, which corresponds to the $L_{ps}\, i_{sd}$ term in (2.3). If necessary, the secondary can supply all the flux required for the machine magnetization (by keeping $i_{sd} = \lambda_p/L_{ps}$), and in this case $Q_p = 0$ i.e. the primary power factor is then unity. However, a larger inverter would be needed if the maximum power factor control is of interest [66,67]. If supplied from a dual-bridge PWM converter, the BDFRM (as well as the DEWRIM) can operate as an efficient reactive power compensator since it is possible to minimize total copper losses in the machine for a given torque by appropriately controlling i_{sd} and hence Q_p according to (2.3) [60]. The unity overall power factor control is accomplished by supplying the reactive power for the primary not from the grid or the inverter through the secondary winding but using the PWM rectifier.

The information on the secondary flux position is normally retrieved from the rotor and primary flux angles in a stationary frame. If the primary winding resistance is ignored the corresponding angular relationship can be written as [60]:

$$\theta_s = (\theta_v - \frac{\pi}{2}) - (p_1 + p_2)\theta_r \tag{2.4}$$

where θ_v represents the angular position of the primary voltage vector (can be easily obtained from phase measurements).

Finally, it should be mentioned that in order to achieve a full cost benefit of using the BDFRM, the supply inverter has to be partially rated which requires a starting procedure to avoid the inverter overloading during start-up. Fortunately, because of the operational-mode flexibility the BDFRM has, it is possible to start it as a conventional wound rotor induction machine. The starting steps are therefore as follows:

1. The machine is freely accelerated close to the synchronous speed with the secondary windings shorted directly or through a variable resistance.

2. After reaching the steady speed dictated by the no-load slip value, the inverter is connected to the secondary windings with either the top or bottom devices on so that zero 3-phase voltage is applied to the machine terminals.

3. Speed control is enabled simultaneously with the inverter connection to bring the machine to the desired (below or above synchronous) speed.

2.2 *Literature Review on Direct Torque Control*

The term 'Direct Torque Control (DTC)' is quite general for some researchers who include the PI–direct torque control [41,46] or direct self torque control in this topic as well. The basic difference between the direct torque control and the Direct Self Control (DSC) is the control property. In DSC the output frequency of the so-operated inverter is proportional to the V_i/λ^* ratio where V_i denotes the dc input voltage of the inverter and λ^* is the reference magnitude of the virtual flux. Specifically [41],

$$f_0 = \frac{1}{4\sqrt{3}} \frac{V_i}{\lambda^*} \tag{2.5}$$

where the virtual fluxes are calculated as time integrals of the line-to-line output voltages of the inverter.

Typically slow switches, such as GTOs, are employed in such inverters, and low switching frequencies are required. Therefore, in DSC drives, the inverter is made to operate in a mode similar to the square-wave one, with occasional zero states thrown in.

Direct Torque Control (DTC) now normally implies the hysteresis (or 'bang-bang') control of torque and flux of a machine. The fundamental principle of DTC is not difficult to understand and a good physical explanation of the method can be found in [39,41]. The relevant details will be discussed in the subsequent chapters in light of its application to the BDFRM.

Before the appearance of the DTC, advanced control strategies for PWM inverter fed induction motor drives have been based on the space vector approach, particularly the Field Oriented Control (FOC) or Vector Control the concept of which is diagrammatically shown in Figure 2.3. In control sense, an induction machine with FOC resembles a conventional dc machine where the control of field flux and torque is inherently decoupled. To achieve the same objective with induction machines, the spatial angular position of the rotor flux is either calculated (indirect control) or measured (direct control) [41]. In this case, torque control is indirect because of its position in the control algorithm prior to the vector control process. As illustrated in Figure 2.3, the reference value of torque comes from the speed control loop. However good torque response can be achieved. One limitation of the flux vector control is the requirement for an encoder [38].

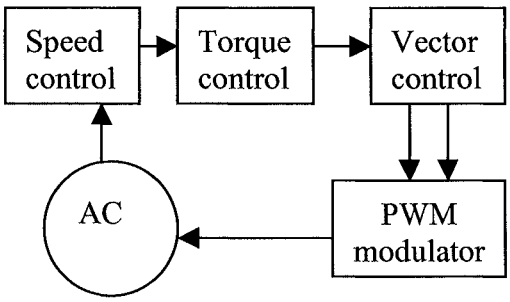

Figure 2.3 A simplified block diagram of flux vector control

The important advantage of the DTC over FOC is that the PI current control loops are omitted and instead hysteresis control of torque and stator flux in a stator frame is applied. In this way, because of the absence of co-ordinated transformations, much faster response and higher control rates can be obtained at the expense of higher switching losses and variable switching frequencies. The DTC schemes are also fewer machine parameter dependent, and in torque control mode, a shaft position sensor is generally not required as the control is stationary frame based. However, the main problem with DTC is the low frequency and/or speed operation as will be elaborated later in this chapter. In this respect, the DTC is clearly inferior to the FOC, which is generally applicable over the entire speed range of the machine. The corresponding block diagram is presented in Figure 2.4. It should be noted as well that some researchers have used the rotor flux as the controlled quantity instead of the stator one [18].

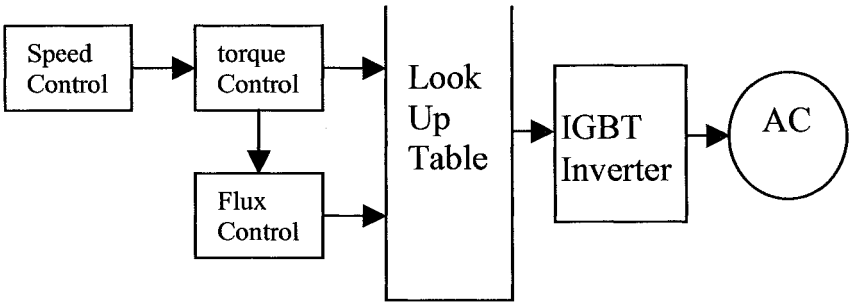

Figure 2.4 The block diagram of DTC

Since the DTC uses hysteresis comparators, it is worth mentioning the effects of the hysteresis band amplitude [32,43]. According to the main DTC principle, the torque presents a pulsation that is directly related to the amplitude of its hysteresis band. The torque ripple should be as small as possible because it causes vibration and acoustic noise. The flux hysteresis bandwidth is immediately reflected on the ripple of the stator flux, which in turn determines the corresponding distortion of the motor currents and therefore influences the harmonic copper losses [43]. In particular, high values of the flux hysteresis band mean high harmonic copper losses. On the other hand, smaller flux band amplitude implies higher switching frequency. The stator flux vector locus approaches a circle and the phase current waveform is nearly sinusoidal if the switching frequency is high enough [26,41]. The switching frequency and switching losses are mainly affected by the torque hysteresis band [32]. It is also notable that even with the zero hysteresis band, there is still the distortion due to a discrete nature of digital control implementation. The main limitation of the existing work on DTC is that a clear distinction of the effects caused by the two bands has not yet been established in the published literature. In most cases, the torque and flux

bands appear to be selected arbitrarily and they are often equal. For example, in [32] a typical value chosen is 7% for both torque and flux bands.

The voltage-vector selection strategy using a switching table is widely applied because it is simple in concept and easy to implement in practice. The combined use of hysteresis comparators and a look-up table eliminates the need for a traditional PWM modulator. The advantages of this approach are twofold: first, small signal delays associated with the modulator are eliminated and, second, the discrete constant carrier frequencies used by the modulator are no longer present. As any other control method, the traditional DTC has also some drawbacks. The switching frequency varies according to the motor speed and the hysteresis band of torque and flux [32,37]. Variable switching frequency is undesirable since the switching capabilities of the inverter are not fully utilized and also result in an unpredictable harmonics current flow. The choice of the hysteresis bands' width normally is based on the worse case [63], obviously this was limited by the thermal condition of the switching devices and not optimised.

If the switching frequency can be kept constant, the minimum torque ripple will be achieved. Therefore some papers can be found to achieve constant switching frequency strategy [49-52]. Another, more severe deficiency, is that the low speed operation down to standstill in most AC drives is difficult and almost impossible to achieve the reason being the voltage integration problems and consequent flux

estimation inaccuracies resulting mainly from the stator resistance effects. It will be shown in this project that this limitation can be overcome with the BDFRM and that stable operation in the entire speed range down to synchronous speed (when the secondary applied frequency is zero i.e. the winding is DC fed) is achievable. This property represents the principal advantage of the BDFRM over more traditional AC machines.

The inverter switching frequency is an important parameter in hardware implementation. From the report of Takashi and Ohmori [54], the torque frequency–response corner frequencies are above 2-kHz. For example, the mean switching frequency for operation with a torque reference frequency of $f_r = 5kHz$ is slightly higher than 1-kHz. Since the inverter has six switching devices (i.e. two per leg), the idealized switching pattern for this same operation would yield a somewhat lower mean switching frequency. From the work presented in [49] the sampling frequency of 10-kHz is sufficient for the induction machine to control the stator flux linkage. In practice, the switching frequency limit of IGBT whose power range is around 10-kW will be about 10-30 kHz. The sampling frequency should be at least double the switching frequency to get a satisfactory result.

The DTC consists in the bang-bang control of the torque and flux, being thus characterised by the fast response to control commands. However, in steady state, the DTC principle results in chaotic switching patterns in the inverter. Unless a high

average switching frequency is enforced by setting the hysteresis loops of the torque and flux controllers to low value, significant torque ripple and undesired acoustic and vibration effects associated with that ripple are produced. Therefore, one of the main goals of the switching improvements is to optimise the steady state flux/torque process [43].

For example, the starting performance is not good enough due to the low speed. In particular an overestimation of the primary resistance may cause undesired oscillations of the stator flux magnitude. This in turn, determines torque oscillation and acoustic noise. It should be noted that, besides stator resistor error, current sensor offsets affect the drive behaviour, particularly in the low speed range [57]. Efforts are made on switching frequency control by some scholars to improve starting performance and the transient response of the machine [32,36,37,43].

The popular space-vector PWM strategy for voltage-source inverters is widely recognised as a means for generating high-quality switching patterns. Such patterns result in low-ripple stator currents and, consequently, smooth flux and torque waveforms. Therefore a class of DTC techniques has been developed in which the control system generates a reference vector of stator voltage, instead of directly indicating the next state of the inverter. The reference voltage vector is then realised using the space-vector pulse width modulation [43].

BDFRM are its brushless structure and the slip power property allowing a smaller inverter to be used; thus having significant cost saving implications especially in larger drives with limited variable speed capability. The critical appraisal of existing work has also shown that most control related research activities have focused on Vector or Field Oriented Control of the machine but no paper has been published on Direct Torque Control of the BDFRM or any other doubly fed motor drive system, particularly in the UK. It is true that some papers have appeared on doubly fed wound rotor induction generators for wind turbines but this work is preliminary in nature and without experimental verification. This project has certainly filled this gap by proposing a viable sensorless direct torque control scheme suitable for the machine use in target applications with restricted speed ranges such as wind turbines and large pumps. The experimental results presented in the following chapters undoubtedly demonstrate that the algorithm allows the BDFRM successful and stable operation down to synchronous speed when the controllable secondary winding is DC supplied this being impossible to achieve with the cage induction machines. It is also important to say that the developed controller can be equally applied to the doubly-excited wound rotor induction machine, which is nowadays becoming an extremely attractive cost-effective solution for variable speed constant frequency wind power generation. It is believed that the BDFRM can be even a better candidate for these and similar systems (off-shore wind turbines in particular) due to the increased reliability afforded by the absence of slip rings and brush gear.

essentially applied to all other machines where the torque-angle dependence and the stator voltage equation are of a similar form as with induction machines. As shown in Chapter 5, the fundamental DTC theory for induction machines can even be used for the BDFRM despite the principally different operating and torque producing mechanisms. The reason for this is the model analogy that can be established between the machines.

Another work worth mentioning is the extension of the DTC concept to the Switched Reluctance Machine [65]. Due to the non-linearity and the fundamentally different operating principles, torque and current are not directly linked as with continuously excited machines. A simple but rather limited torque estimation can be performed by using a linear machine model. However the paper proposes an accurate model including the non-linear characteristics. The key part of the controller is a look-up table based on the traditional DTC concept.

2.3 Conclusions

The literature review on the BDFRM has been carried out from both machine and control point of views in order to properly position the research being undertaken as part of this project and also to fully realise its main scientific contribution and novelty. This literature search on the subject topic can also help one better understand the machine unusual operation and the ways it can be controlled especially considering its highly unconventional torque producing mechanism. One of the important conclusions of this work is that the main motivations for considering the

In this project, the poor starting performance of the DTC machine is elegantly avoided since the BDFRM is typically started as a wound rotor induction machine (as previously mentioned) with the inverter being connected and control enabled only after the machine reaches (or is near to) its synchronous speed. However, the low speed problems of conventional machines with DTC are still present with the BDFRM but in a limited speed range around synchronous speed when the secondary supply frequencies are small. The DTC algorithm proposed in this thesis allows one to overcome these low frequency difficulties and achieve stable and reliable operation of the machine even at synchronous speed with the secondary winding being DC in this case.

Most of the DTC research is still predominantly related to Induction Machines at present [32,36,37,41,43,45,46]. One example of a DTC drive other than induction machine is the work of L. Zhong and his colleagues [53]. Although there is no experimental result to support the developed theory, this paper has showed how the concept of DTC can be applied to other machines such as Permanent Magnet Synchronous Motor (PMSM). By ignoring the influence of harmonics in inductance and back EMF, together with saturation effects, they have implemented a control scheme similar to that for the induction machine after establishing that the torque-angle relationships is identical for the two machines and that the same look-up table can be used for both the PMSM and the induction machine. One important conclusion of this paper is that the switching strategy for induction machines can be

Chapter 3 Scalar Control of Brush-less Doubly-Fed Reluctance Machine

The key part of this project is to design the electrical controller that should be based on the correct understanding of BDFRM. It is therefore helpful to have a machine model built in software ready for the future use. Scalar control can serve as an examination tool at early stage of the simulation. This chapter will explain primarily how to built the mathematical machine model. There are two parts of Scalar Control, one is closed-loop control that normally employs a PI speed controller and the other is open constant voltage/ frequency (V/f) control. The scalar control methods are quite simple. The main task of this chapter is to confirm the theory and investigate the dynamics of model. This work has not been done so far. In section 3.1, the mathematical equation and the per-phase equivalent diagram of BDFRM are quoted. The concept of two reference frames is important in establishing the model. This rotating reference frame concept has nothing to do with the control method, but just as an effective way to understand and develop the machine principles. Based on this theory, a mathematical model was developed in section 3.3. The block diagram of the scalar control is shown in section 3.4. The rotor speed can be controlled by the secondary frequency. And the relationship between speed and secondary frequency is corresponding to the theory. The machine can be controlled to run either in super- or sub- synchronous speed. The speed plot in section 3.4 shows the stability limitation of

scalar control.

3.1 Mathematical Equations of The BDFRM

Due to the limitation of the length of this thesis, a detailed explanation of the machine model will not be included it can instead be found in the following works [7,17, 29,33]. The d-q model is to be used because it has less variables than the three-phase model. The result is shown below for convenience. If no zero sequence components exist the voltage equations become:

$$\begin{bmatrix} V_{dp} \\ V_{qp} \\ V_{ds} \\ V_{qs} \end{bmatrix} = \begin{bmatrix} r_p + L_p p & -\omega L_p & L_m p & -\omega L_m \\ \omega L_p & r_p + L_p p & \omega L_m & L_m p \\ L_m p & -(\omega - \omega_r) L_m & r_p + L_p p & -(\omega - \omega_r) L_s \\ (\omega - \omega_r) L_m & L_m p & (\omega - \omega_r) L_s & r_p + L_p p \end{bmatrix} \begin{bmatrix} i_{dp} \\ i_{qp} \\ i_{ds} \\ i_{ds} \end{bmatrix} \tag{3.1}$$

where 'V_{dp}, V_{qp}' indicate the primary d and q voltage respectively;

'V_{ds}, V_{qs}' indicate the secondary d and q voltage respectively;

'ω, ω_r' indicate the angular velocity of reference frame and rotor speed respectively

'p' is the sign of differentiation;

'$L_p, L_s and L_m$' are primary inductance, secondary inductance and mutual inductance;

by setting ω=0 and defining the " slip" as:

$$S = \frac{\omega_s}{\omega_p} = \frac{\omega_p - p_r \omega_{rm}}{\omega_p} \tag{3.2}$$

It can be seen that the equivalent circuit (Figure 3.1) for the steady state operation of DERM has exactly the same form as that of a conventional wound rotor induction machine except the peripherals conditions.

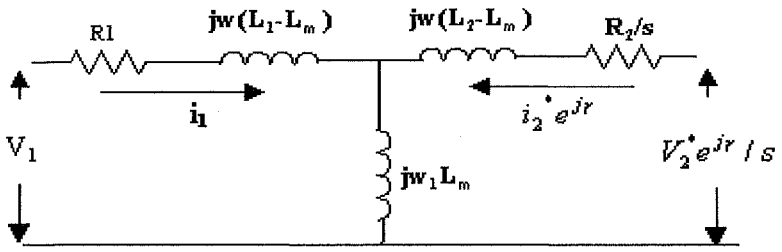

Figure 3.1 Per-phase steady state equivalent circuit of BDFRM

It is also interesting to observe that the equations in the d-q-n frame and equivalent circuits have exactly the same forms as those of a doubly fed wound rotor induction machine, which implies that the doubly excited reluctance machine is equivalent to a wound rotor induction machine with equivalent pole pair number of P_1+P_2.

3.2 Additional Equations For The Torque And Speed

The original torque producing formula in three-phase condition is (3.3).

$$T_e = i^T \frac{\partial \left[L_{ABC,abc} \right]}{\partial \theta_{rm}} i \tag{3.3}$$

where $i = \begin{bmatrix} i_{abc} \\ i_{ABC} \end{bmatrix}$ (3.4)

It can be shown that the torque equation after the Park transformation becomes

$$T_e = \frac{3}{2}(p_p + p_s)(\lambda_{dp} i_{qp} - \lambda_{qp} i_{dp}) \tag{3.5}$$

The speed definition can be traced from the balance of mechanical equations:

$$J \frac{d\omega_{rm}}{dt} = T_e - T_l \tag{3.6}$$

where J denotes the rotor inertia and T_e is the electrical torque and T_l is the load torque.

3.3 The Software Model of BDFRM

3.3.1 FLUX CALCULATION

If the expressions of (3.3) and (3.4) are written in the D-Q form, the flux model can be directly extrapolated in d-q form:

$$\begin{aligned}
\lambda_{pd} &= L_p i_{pd} + L_{ps} i_{sd} \\
\lambda_{pq} &= L_p i_{pq} - L_{ps} i_{sq} \\
\lambda_{sd} &= L_s i_{sd} + L_{ps} i_{pd} \\
\lambda_{sq} &= L_s i_{sq} - L_{ps} i_{pq}
\end{aligned} \tag{3.7}$$

it can also be written in the form of a matrix:

$$\begin{bmatrix} \lambda_{pd} \\ \lambda_{pq} \\ \lambda_{sd} \\ \lambda_{sq} \end{bmatrix} = \begin{bmatrix} L_p & & L_{ps} & \\ & L_p & & -L_{ps} \\ L_{ps} & & L_s & \\ & -L_{ps} & & L_s \end{bmatrix} \begin{bmatrix} i_{pd} \\ i_{pq} \\ i_{sd} \\ i_{sq} \end{bmatrix}; \tag{3.8}$$

so that the voltage equations can be written in the form:

$$\begin{aligned}
u_{pd} &= R_p i_{pd} + \frac{d\lambda_{pd}}{dt} - \omega \lambda_{pq} \\
u_{pq} &= R_p i_{pq} + \frac{d\lambda_{pq}}{dt} + \omega \lambda_{pd} \\
u_{sd} &= R_s i_{sd} + \frac{d\lambda_{sd}}{dt} - (\omega_r - \omega)\ \lambda_{sq} \\
u_{sq} &= R_s i_{sq} + \frac{d\lambda_{sq}}{dt} + (\omega_r - \omega)\ \lambda_{sd}
\end{aligned} \tag{3.9}$$

Speed, flux estimation techniques based on mathematical model will be discussed in section 7.2, Chapter 7.

3.3.2 STATE SPACE MODEL OF THE BDFRM

The model of the machine can be produced using the equations independently [31]. The use of state-space reduces the program length and speeds up the simulation. It can be expressed in state space form:

$$\begin{bmatrix} u_{pd} \\ u_{pq} \\ u_{sd} \\ u_{sq} \end{bmatrix} = \begin{bmatrix} R_p & & & \\ & R_p & & \\ & & R_s & \\ & & & R_s \end{bmatrix} \begin{bmatrix} i_{pd} \\ i_{pq} \\ i_{sd} \\ i_{sq} \end{bmatrix} + p \begin{bmatrix} \lambda_{pd} \\ \lambda_{pq} \\ \lambda_{sd} \\ \lambda_{sq} \end{bmatrix} + \omega \begin{bmatrix} -\lambda_{pq} \\ \lambda_{pd} \\ & \end{bmatrix} + (\omega_r - \omega) \begin{bmatrix} & \\ -\lambda_{sq} \\ \lambda_{sd} \end{bmatrix} \tag{3.10}$$

Substituting in the matrix of flux and re-organising the state space, yields:

$$\begin{bmatrix} u_{pd} \\ u_{pq} \\ u_{sd} \\ u_{sq} \end{bmatrix} - \omega \begin{bmatrix} -\lambda_{pq} \\ \lambda_{pd} \\ & \end{bmatrix} - (\omega_r - \omega) \begin{bmatrix} & \\ -\lambda_{sq} \\ \lambda_{sd} \end{bmatrix} = \begin{bmatrix} R_p & & & \\ & R_p & & \\ & & R_s & \\ & & & R_s \end{bmatrix} \begin{bmatrix} i_{pd} \\ i_{pq} \\ i_{sd} \\ i_{sq} \end{bmatrix} + p \begin{bmatrix} L_p & & L_{ps} & \\ & L_p & & -L_{ps} \\ L_{ps} & & L_s & \\ & -L_{ps} & & L_s \end{bmatrix} \begin{bmatrix} i_{pd} \\ i_{pq} \\ i_{sd} \\ i_{sq} \end{bmatrix} \tag{3.11}$$

Comparing this with the standard matrix:

$$\begin{aligned} \dot{X} &= AX + BU \\ Y &= CX + DU \end{aligned} \tag{3.12}$$

The X variable can be set as current, that is:

$$X = \begin{bmatrix} i_{pd} \\ i_{pq} \\ i_{sd} \\ i_{sq} \end{bmatrix}; \tag{3.13}$$

$$A = -inv \begin{bmatrix} L_p & & L_{ps} & \\ & L_p & & -L_{ps} \\ L_{ps} & & L_s & \\ & -L_{ps} & & L_s \end{bmatrix} \begin{bmatrix} R_p & & & \\ & R_p & & \\ & & R_s & \\ & & & R_s \end{bmatrix} \tag{3.14}$$

$$B = inv\begin{bmatrix} L_p & & L_{ps} & \\ & L_p & & -L_{ps} \\ L_{ps} & & L_s & \\ & -L_{ps} & & L_s \end{bmatrix} \tag{3.15}$$

$$U = \begin{bmatrix} u_{pd} \\ u_{pq} \\ u_{sd} \\ u_{sq} \end{bmatrix} - \omega \begin{bmatrix} -\lambda_{pq} \\ \lambda_{pd} \\ \\ \end{bmatrix} - (\omega_r - \omega) \begin{bmatrix} \\ \\ -\lambda_{sq} \\ \lambda_{sd} \end{bmatrix}$$

$$= \begin{bmatrix} u_{pd} \\ u_{pq} \\ u_{sd} \\ u_{sq} \end{bmatrix} - \omega \begin{bmatrix} & -L_p & & L_{ps} \\ L_p & & L_{ps} & \\ & & & \\ & & & \end{bmatrix} \begin{bmatrix} i_{pd} \\ i_{pq} \\ i_{sd} \\ i_{sq} \end{bmatrix} - (\omega_r - \omega) \begin{bmatrix} & & L_{ps} & -L_s \\ L_{ps} & & L_s & \\ & & & \\ & & & \end{bmatrix} \begin{bmatrix} i_{pd} \\ i_{pq} \\ i_{sd} \\ i_{sq} \end{bmatrix} \tag{3.16}$$

The output of the state-space will be the currents of the primary and secondary sides:

$$C = \begin{bmatrix} 1 & & & \\ & 1 & & \\ & & 1 & \\ & & & 1 \end{bmatrix} \tag{3.17}$$

D=0

Using the simulink blocks of MATLAB, the machine model is organised as Figure 3.2. It is important to note the ways in which voltages are fed into the model. The model is built with primary voltage in its reference frame (rotating at ω_p), while

secondary voltage is in its own frame (rotating at speed of ω_s with respect to the stationary frame). Therefore, the function of the voltage transformation is a pre-requisite of the model design.

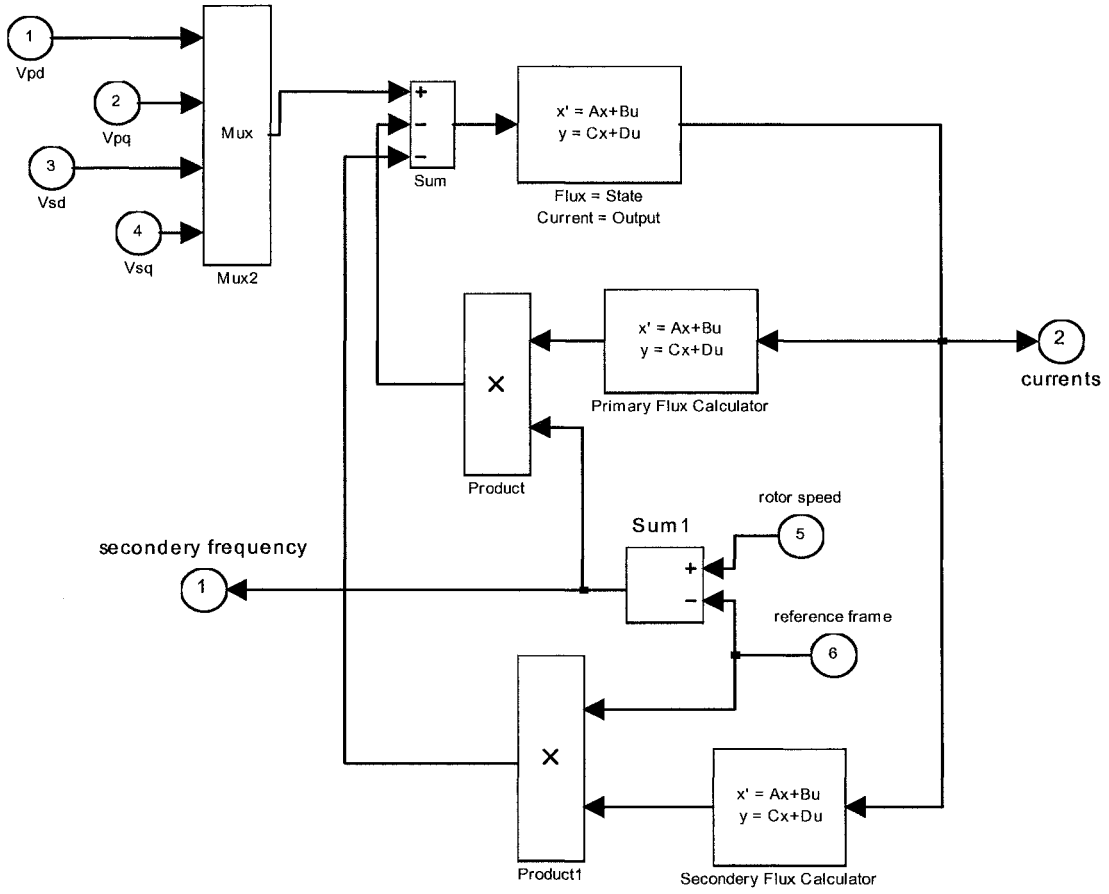

Figure 3.2 The model of machine

3.4 Scalar Control Of BDFRM

The model must now be verified against theoretical results to ensure it's correct operation. To prove the theory, simple control strategy is applied to the model. No

papers currently exist detailing a comparison between the simulation results of the two scalar control techniques used with BDFRM.

The two Scalar control techniques are open-loop constant Voltage/frequency control and close loop control.

3.4.1 OPEN-LOOP CONTROL ALGORITHM

As mentioned previously, not all of the signals fed into the motor are controllable; only the frequency and the voltage of secondary side can be controlled. That is why the secondary winding side is often referred to as the 'control side'. Basically open-loop constant Voltage/frequency control has been developed for induction machines. Having noticed the model similarity between the BDRFM and the induction machine, scalar control algorithms can be developed for the BDFRM using those already developed for the induction machine as a benchmark.

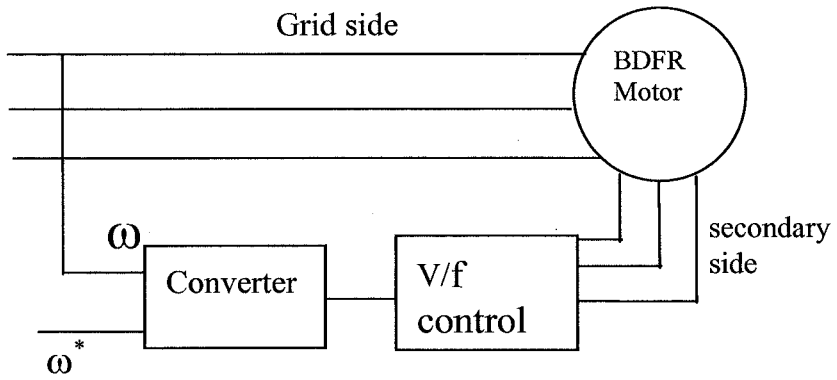

Figure 3.3 Open-loop Control Block Diagram

If the stator resistance is small enough to be ignored (which is the case compared to the stator voltage), the stator flux can be expressed as:

$$\lambda \cong \frac{V_s}{\omega} = \frac{V_s}{2\pi * f} \tag{3.18}$$

This means that to maintain the stator flux constant, typically rated level, the stator voltage should be adjusted in proportion to the supply frequency.

The key expression, which the BDFRM scalar control is based upon, is given in equation (3.2). The desired frequency is applied to the secondary (as a step or as a ramp change) and the machine is allowed to reach steady state without any speed feedback. The respective simplified block diagram is presented in Figure 3.3.

In the simulation model the voltage is supplied with d-q form. The conversion of the three-phase to d-q form is based on the principle of Park transform:

$$\begin{bmatrix} f_{q1} \\ f_{d1} \\ f_{n1} \end{bmatrix} = \frac{2}{3} \begin{bmatrix} \cos(\theta) & \cos(\theta - \frac{2\pi}{3}) & \cos(\theta + \frac{2\pi}{3}) \\ \sin(\theta) & \sin(\theta - \frac{2\pi}{3}) & \sin(\theta + \frac{2\pi}{3}) \\ \frac{1}{2} & \frac{1}{2} & \frac{1}{2} \end{bmatrix} f_{ABC} \tag{3.19}$$

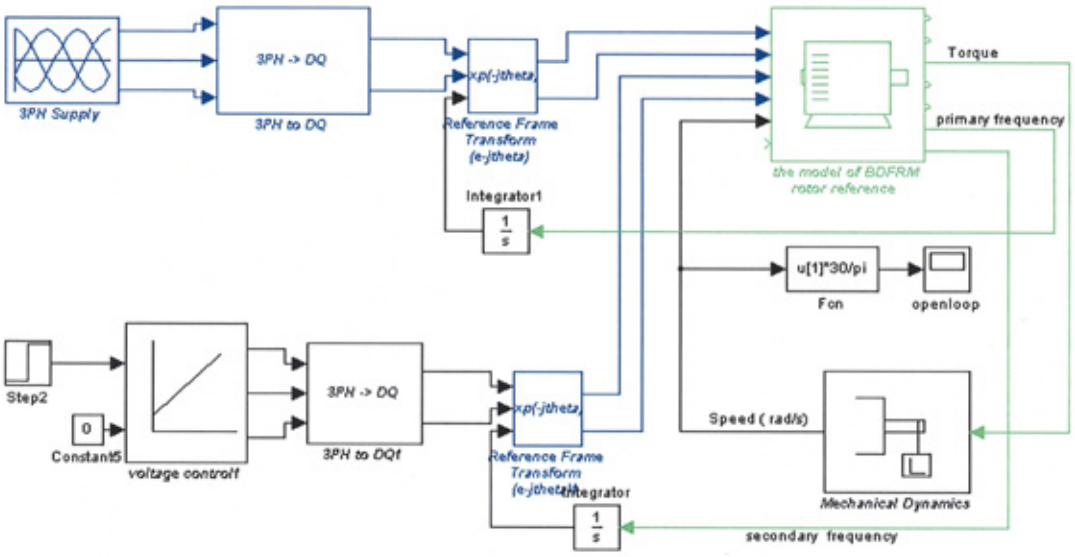

Figure 3.4 Model of open loop control of BDFRM

3.4.2 STARTING

One of the attractive properties of the BDFRM is the operational mode flexibility. This means that it can operate as an induction machine (by simply shorting the secondary terminals; this is an important 'fail-safe' operating mode in case of inverter breakdown), as a synchronous machine (by feeding the secondary, which plays the role of the field winding, with DC) or as a doubly fed machine (normal operation).

Starting the machine as an induction machine is a practical way for preventing inverter overloading (if this is fractionally rated) during start-up. Otherwise, a fully rated converter would be required. The simulation results corresponding to the machine acceleration from rest to a synchronous speed (with the DC fed secondary

i.e. when the applied frequency is zero) is presented in Figure 3.5. The BDFRM speed response is obviously quite similar to that of an induction machine. It can be seen from Figure 3.5 that the dynamics during 0-2s correspond machine start performance. There are some visible ripples in the steady state (after 2s). This is not expected since the model of machine is an ideal one. The ripple can be attributed to the simulation parameters chosen. These plots were acquired with the 'Solver Options' of 'variable step' and 'the step size ' set to 'auto'. By manually adjusting these simulation parameters, the simulation time is significantly reduced. Running the simulation with different solver options, it is seen that the ripple can be greatly reduced, under the correct conditions it should be possible to produce a ripple of negligible size.

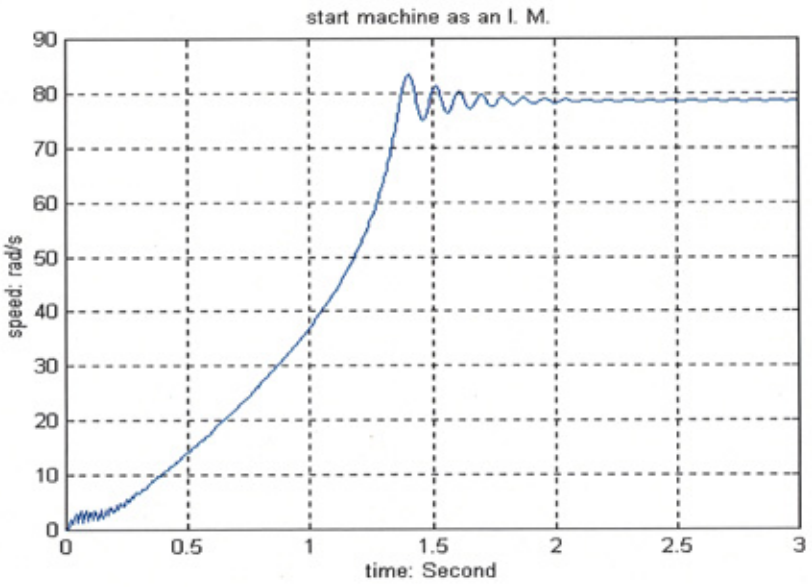

Figure 3.5 Starting the BDFRM with the secondary side short-circuited

3.4.3 BDFRM RESPONSE WITH OPEN-LOOP CONTROL

After the machine reaches its steady state operating at a synchronous speed, a reference frequency signal corresponding to a desired machine speed can be applied

to the secondary side. If this command frequency signal is positive, the MMFs generated by the two-stator windings will rotate in the same direction and the machine will increase its speed as shown in Figure 3.6. However, if a decrease in machine speed is desired then a 'negative' (this simply means that the opposite secondary winding sequence to the primary is used and therefore there is a counter-action, i.e. stalling effect, between the secondary mmf relative to the primary) frequency should be supplied to the secondary as follows from (3.2). The machine speed response in this case is illustrated in Figure 3.7. It should be noted that the open-loop control scheme in Figure 3.3 gives satisfactory results providing that the frequency step changes are relatively small. Otherwise, stability problems, that are inherent with open-loop control, may occur. This simulation result confirms a similar conclusion to Ojo[35].

3.4.4 OPEN-LOOP CONTROL WITH FREQUENCY RAMP

The previously mentioned deficiency of open-loop control may not be that severe in pump-type drives where the required speed variations are restricted and where the fast machine response is not imperative. Yet, for this and similar applications, improved stability and smoother operation is desirable and can be achieved with frequency ramping as shown in Figure 3.8 and Figure 3.9. From the simulation results it can be seen that the machine transient performance is considerably better with much lower speed oscillations than in Figure 3.5.

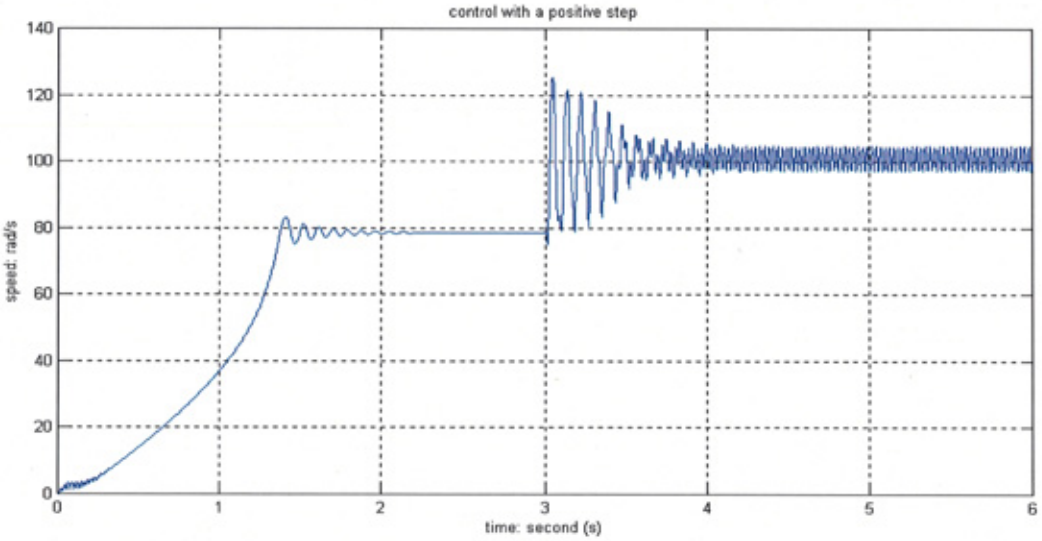

Figure 3.6 Control the BDFRM with a positive frequency step change

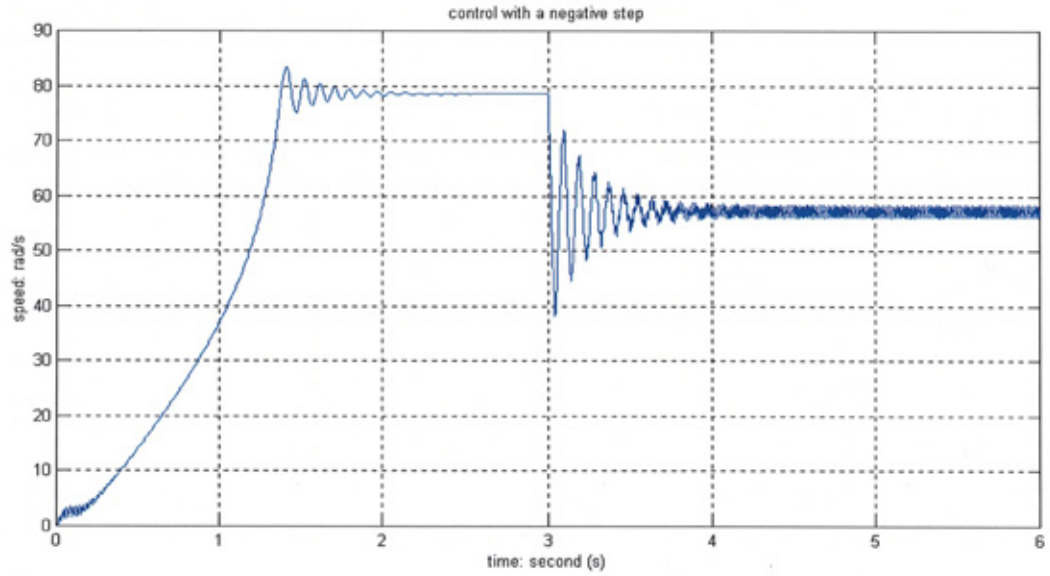

Figure 3.7 Control the BDFRM with a negative frequency step change

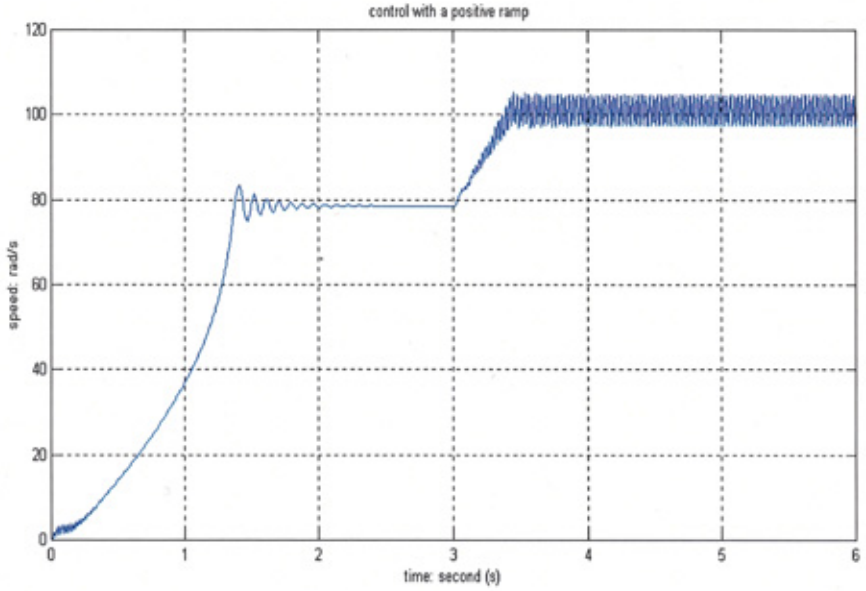

Figure 3.8 BDFRM control with positive ramp signal

Clearly, highly accurate speed control is not possible because the actual slip varies with the value of the load. It should be noted that the performance of the open-loop control could be improved. Many texts are available dealing with the voltage-drop compensation at low speed range of induction machines [58]. This method will not be dealt with in the later chapter due to the different approach to the flux (Chapter 4).

3.4.5 CLOSED-LOOP CONTROL OF BDFRM

Closed-loop P.I. control of the BDFRM (as for the other machines) allows generally superior performance compared to open-loop control in areas including; improved stability, faster dynamic response and cleaner waveforms. The simplified algorithm for closed-loop control is presented in Figure 3.10. where the motor speed is used as feedback (by measurement or estimation). The feedback of actual angular velocity is

compared with the reference speed. The speed error signal is then applied to the PI controller. The output of the PI controller is the frequency modified for the Voltage Source Inverter.

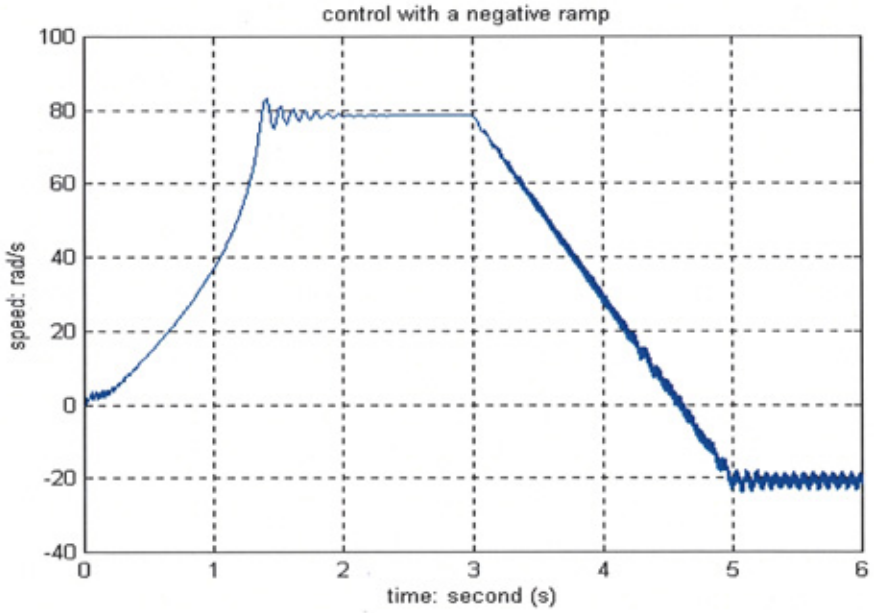

Figure 3.9 Control the BDFRM with a negative ramp signal

The main problem with PI controllers is in their optimal gain tuning, for different speeds, it may require re-tuning to produce the optimum result.

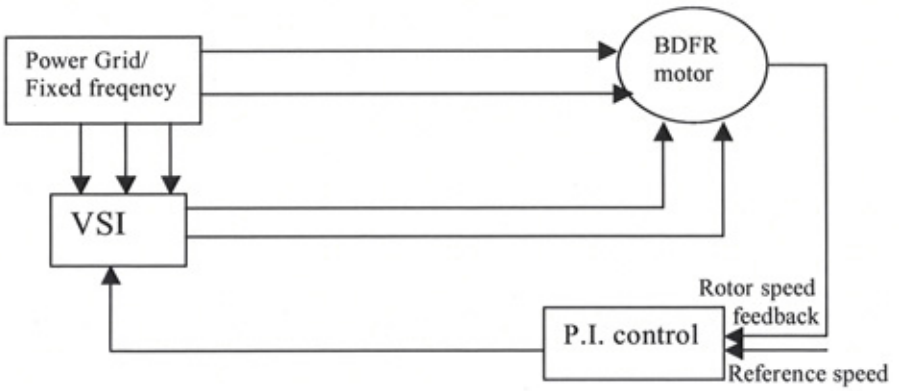

Figure 3.10 Block diagram of closed-loop control

In this report, however, optimal control is not an issue and a simple heuristic approach to the gain selection has been chosen for convenience. It can be seen from Figure 3.12 that the corresponding speed waveform is almost ripple-free in steady state as compared to the open-loop system in Figs 3.5-3.7 as expected. If the start method changed to the normal way, that is, the control side is not shorted from the beginning(which will have negative effects in practice of course), the dynamics can be seen from the Figure 3.12.

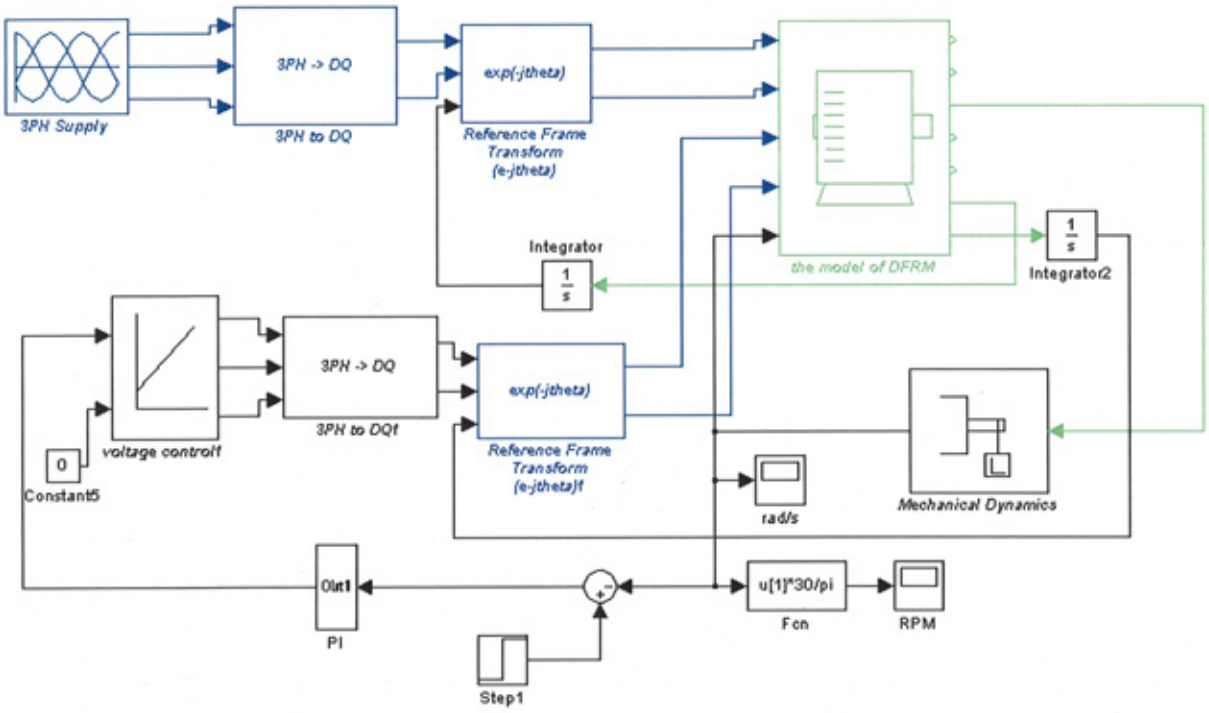

Figure 3.11 Simulation diagram of close loop control BDFRM

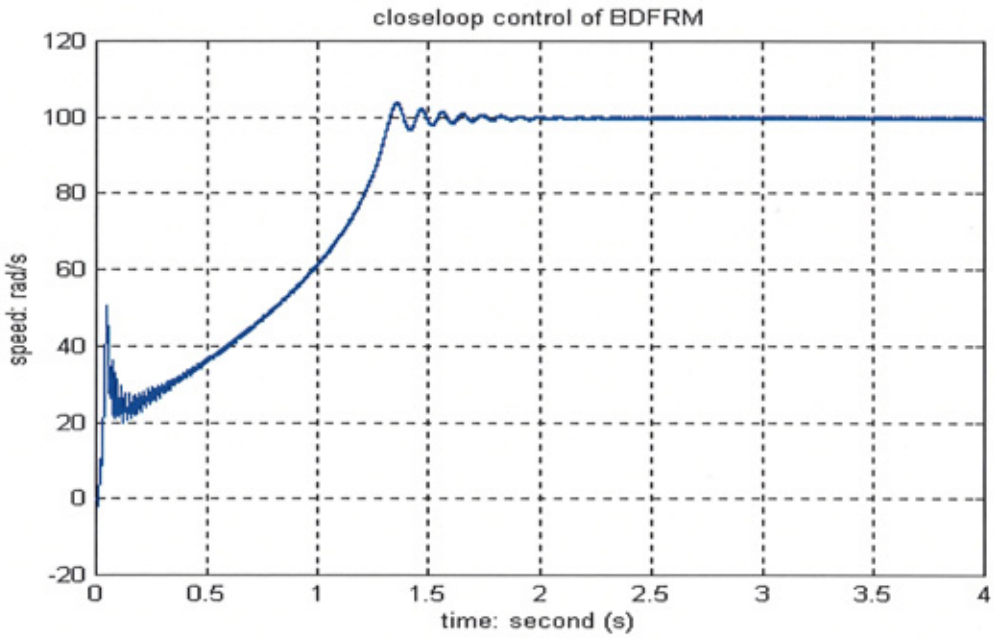

Figure 3.12 Simulation result of close-loop control

3.5 Conclusions

This chapter has presented a review of the basic operation and scalar control principles of the BDFRM. Fundamental modelling aspects have been also addressed and close model analogies of the BDFRM and the induction machine have been emphasised. It is interesting that these model similarities exist despite the fundamentally different torque producing mechanism of the two machines. This means that the existing control philosophies and achievements in wound rotor induction machine control are essentially applicable to the BDFRM.

Another important contribution of the chapter is the consideration of scalar control methods for BDFRM. This study has not yet been carried out in the literature

available on the subject. The plots in this chapter are the computer simulation results to illustrate the scalar control performance.

Chapter 4 Direct Torque Control of Brushless Doubly-Fed Reluctance Machine

Direct Torque Control (DTC) has been originally developed for high performance induction motors and most of the existing research on this method is related to this particular machine [32,36,37,41,43,45,46] although its applications to other high-speed brushless machines have also been reported in the literature [53,65]. The controllable parameters in this method are the stator flux and electromagnetic torque. Compared with other advanced control strategies such as Field Oriented Control (FOC), the DTC eliminates current control loops and is executed in a stationary reference frame hence avoiding the need for coordinated transformations and allowing much higher (but variable) control and switching rates without using a shaft position sensor in the torque controller.

The main aim of this project is the development and experimental evaluation of an algorithm for direct control of the secondary (inverter-fed) winding flux and electromagnetic torque of the BDFRM. It has not been used for doubly-excited drive systems so far despite the fact that DTC has been applied lots of conventional inverter-fed AC machines. From this point of view, and due to the modelling and control similarities between the BDFRM and the traditional wound rotor induction

machine, the work presented in this thesis can serve as a reference for DTC research on both machines. The original DTC strategy for cage induction machines is studied first in order to establish the fundamental DTC principles and to see how and if the traditional algorithm can be modified to be applicable to a doubly-fed machine, such as the BDFRM, having a principally different operating mechanism. The previous chapter (Chapter 3) have already introduced the dynamic model for the BDFRM, which will be used in this chapter to develop the DTC strategy for this machine.

The traditional DTC method has been successfully applied to the cage induction machine where the rotor flux is travelling at the speed of the stator flux: synchronous speed. Unlike the induction machine, however, the BDFRM has two stator windings of different pole numbers and with generally different applied frequencies, so that the resultant revolving fields by themselves are not mutually stationary. In the presence of a cageless reluctance rotor having half the total number of the stator poles, there is a modulating influence on the stator mmfs resulting in the magnetic coupling of the windings required for the torque production. As will be shown in the following sections, in the BDFRM case, due to this modulating action of the reluctance rotor, two flux sidebands are produced for each winding with only one of them coupling with the complementary winding mmf to generate torque. Therefore, it is not the fundamental flux that participates in the electromechanical energy conversion but the side-band components. As a consequence of this, the magnetic coupling between the windings is relatively weak (even for high saliency ratio rotors) and the

torque/volume of the BDFRM is inferior to the induction machine (i.e. a larger BDFRM is required for the same torque)[8,33]. Because of this quite peculiar and highly unconventional operating principle, an alternative DTC approach has to be established for the BDFRM.

From a machine point of view, the main motivation for considering the DTC method is the prospect for faster transient response[1] that can be achieved by varying the control variables in a 'bang-bang' fashion. Another reason is certainly the BDFRM amenability to DTC implementation afforded by its double feeding. The improved dynamic performance, together with the cost benefits associated with the lower inverter rating, should make the BDFRM competitive.

4.1 Mathematical Preliminaries

Among kinds of equivalent torque expressions developed in [29, 31, 33, 34], the following one is particularly suitable for explaining the DTC concept for the BDFRM:

$$T_e = \frac{3}{2} p_r \frac{L_{ps}}{L_p} \lambda_p i_{sq} \tag{4.1}$$

where $\lambda_{ps} = \frac{L_{ps}}{L_p} \lambda_p$ is the primary flux coupling the secondary winding that is rotating at the same speed as the secondary mmf i.e. at ω_s as illustrated in Figure

[1] This is compromised by the generally higher leakage inductances (compared to other conventional machines) of the BDFRM resulting from its unusual torque producing mechanism [8].

4.1. The secondary q-axis current (with the secondary frame d-axis being aligned with λ_{ps}), denoted by i_{sq} in (4.1), is shown in Figure 4.1 for convenience. Since the primary winding is grid-connected, the primary flux magnitude is nearly constant and so is the mutual flux component λ_{ps}. Therefore, the machine is virtually fully fluxed under all operating conditions (even when unloaded) meaning that the inductance variations due to saturation effects are small and can be neglected. Therefore, the mutual inductance L_{ps} and primary inductance L_p can be assumed constant.

It follows from (4.1) that the electromagnetic torque is directly proportional to i_{sq}. By defining a secondary current angle α as the angle depicting the secondary current vector position in a secondary frame (i.e. with respect to λ_{ps}), one can write $i_{sq} = i_s \cdot \sin\alpha$ and from (4.1) the torque per secondary ampere (TPIA) becomes:

$$\frac{T_e}{i_s} = \frac{3}{2} p_r \frac{L_{ps}}{L_p} \lambda_p \sin \alpha_s \tag{4.2}$$

Clearly the maximum torque per secondary winding ampere (MTPIA) is achieved for $\alpha_s = \pi/2$ i.e. if all of the secondary current is torque producing ($i_s = i_{sq}$). The MTPIA control strategy is important as it allows to minimise the inverter rating and improve the machine efficiency for a given torque output.

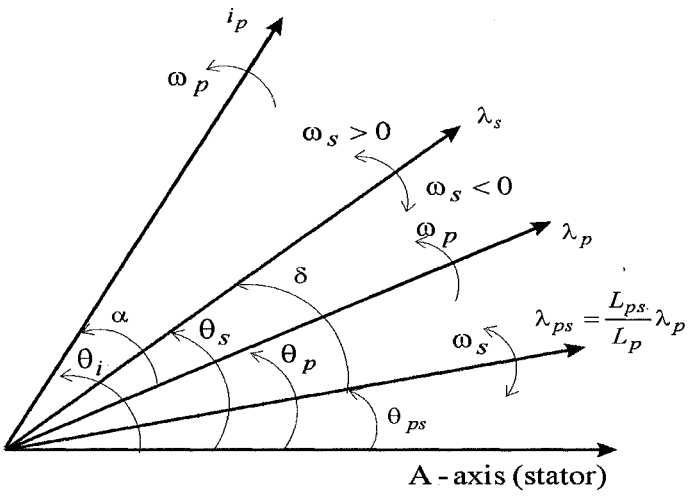

Figure 4.1 Reference frames for the BDFRM

The dynamic model equations for the BDFRM can be found in Chapter 3 and [17, 29, 60,64]. The d-q flux expressions in rotating reference frames are reproduced here for convenience of analysis:

$$\begin{aligned}
\lambda_{pd} &= L_p i_{pd} + L_{ps} i_{sd} \\
\lambda_{pq} &= L_p i_{pq} - L_{ps} i_{sq} \\
\lambda_{sd} &= L_s i_{sd} + L_{ps} i_{pd} \\
\lambda_{sq} &= L_s i_{sq} - L_{ps} i_{pq}
\end{aligned} \tag{4.3}$$

where the subscripts 'p' and 's' indicate the primary and secondary quantities respectively.

In case of the primary flux oriented control (when the primary reference frame d-axis, rotating at ω_p, is aligned with λ_p vector and the secondary reference frame d-axis,

rotating at ω_s lies along λ_{ps} vector in Figure 4.1), the above expression can be further simplified as:

$$\begin{aligned} \lambda_{pd} &= L_p i_{pd} + L_{ps} i_{sd} = \lambda_p \\ \lambda_{pq} &= L_p i_{pq} - L_{ps} i_{sq} = 0 \end{aligned} \tag{4.4}$$

Substituting (4.4) into (4.3):

$$\lambda_{sq} = L_s i_{sq} - L_{ps} i_{pq} = (L_s - \frac{L_{ps}^2}{L_p}) i_{sq} \tag{4.5}$$

while

$$\lambda_{sq} = \lambda_s \sin\delta \tag{4.6}$$

where 'δ' denotes the secondary flux angle in the respective reference frame i.e. the angle between the secondary flux and mutual flux $\lambda_{ps} = \frac{L_{ps}}{L_p} \lambda_p$ (secondary d-axis) as can be seen from Figure 4.1.

Defining $K = L_s - \frac{L^2 ps}{L_p}$, the machine torque now can be expressed as:

$$T_e = \frac{3 p_r}{2 K} \frac{L_{ps}}{L_p} \lambda_p \lambda_s \sin \delta \tag{4.7}$$

Notice that the torque expression (4.7) is commonly encountered in the fundamental DTC theory for the induction machine (this analogy again reinforces the strong modelling link that exists between the two machines). It can be easily concluded from (4.7) that λ_{sq} is actually a torque-producing secondary flux component as it is directly related to i_{sq} as shown in (4.5). Therefore, by increasing (decreasing) λ_{sq}

i.e. δ and thus $\theta_s = \delta + \theta_{ps}$, the machine's instantaneous torque would increase (decrease). Note that, $\theta_{ps} = \int \omega_s dt \approx const$ as the secondary frame position variation during such a short transient is generally negligible, and especially at small ω_s values, which is normally the case. More importantly, this means that one can implement DTC in a stationary frame as is usual for this method.

The secondary flux expression using vector notation is:

$$\boldsymbol{\lambda}_s = \int (\mathbf{u}_s - \mathbf{i}_s R_s) dt \tag{4.8}$$

From this point of view the voltage applied will influence the flux linkage and in turn the electrical torque as with induction machines. However, it is well known that if implemented by the controller this expression causes estimation problems at low frequencies when the resistance effects are more pronounced (as $u_s \approx R_s i_s$) giving erroneous estimates. Fortunately, owing to the BDFRM double feeding, it is possible to avoid using (4.8) for the secondary flux estimation and instead obtain estimates from measurements of the primary quantities (voltages and currents) having smooth, ripple-free waveforms at line frequency. Issues related to this have been addressed in detail in Chapter 6.

4.2 Direct Torque Control

According to the fundamental DTC theory [4,2,41], the flux locus is a circle and can be divided into six sectors each being associated with one of the six non-zero (active) voltage vectors of a PWM Voltage Source Inverter (VSI) shown in Figure 4.2.

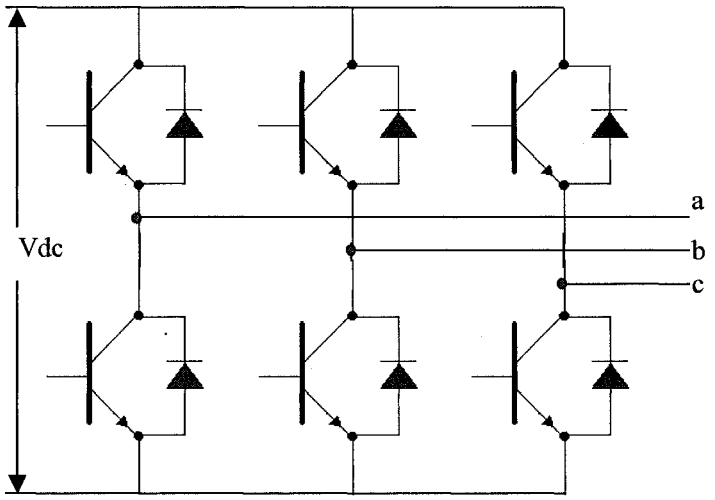

Figure 4.2 Diagram of IGBT bridge

The conventional six-step Voltage Source Inverter (VSI) has six active (non-zero) and two zero voltage states (shown in Figure 4.3). The non-zero voltage space vectors are displaced by π/3 radians (Figure 4.3) and can be formulated as follows (in a stationary frame):

$$u_k = u_{ds} + u_{qs} = ue^{j\beta} = \frac{2}{3}V_{dc}e^{j(k-1)\pi/3} \tag{4.9}$$

where k = 1, 2, … 6.

The corresponding vectors (including the zero ones) and their binary codes are presented in Figure 4.3 below, where '1' signifies the top device in a particular leg

'ON' and the bottom 'OFF' and '0' indicates the opposite states i.e. the top devices 'OFF' and the bottom ones 'ON'. The two zero vectors are for the case when either all the top devices are 'ON' and the bottom ones 'OFF' (111) or vice-versa i.e. all the top devices are 'OFF' and the bottom counterparts are 'ON' (000). The sequence of three bits indicates the three inverter legs, the most significant bit corresponding to phase A, the middle one to phase B and the least significant bit is for phase C (see Figure 4.2).

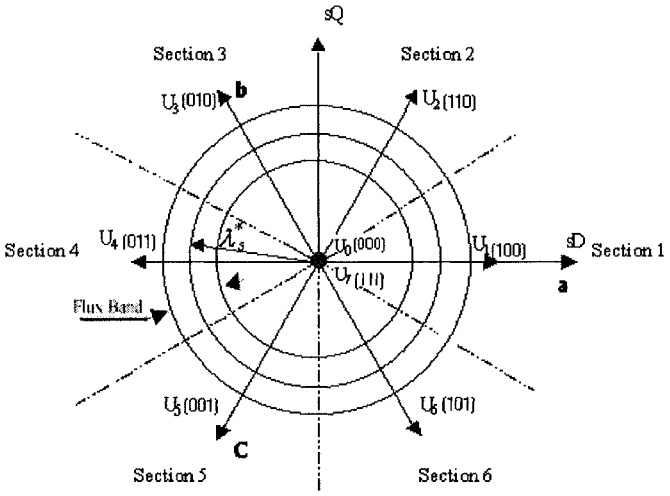

Figure 4.3 Stationary frame plane divided into six sectors with secondary flux hysteresis band denoted by two circles

From equation (4.9), choosing an appropriate non-zero (active) switching state will decrease or increase the stator flux-linkage space vector depending on a desired action. During a very short time interval t one can use the Euler's approximation of the differential in (4.9), in which case the voltage applied by the inverter will influence the instantaneous flux as follows:

$$\lambda_{st} = \mathbf{u}_s t + \lambda_{s0} \tag{4.10}$$

where the subscript '*s0*' indicates the original value of flux (i.e. at the beginning of the time interval t) while '*st*' shows the resultant flux value at the end of the time interval. This voltage effect on the flux magnitude is graphically illustrated in the following figure.

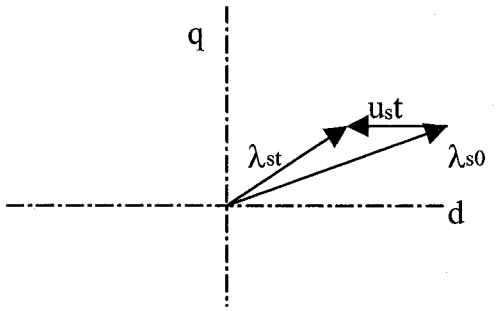

Figure 4.4 Illustration of the impact of voltage vector on the flux linkage

The vector diagram in Figure 4.4 shows that the applied voltage can change both the direction and modulus of the flux. In the BDFRM, the secondary voltage is controllable by the inverter and it is this voltage that will influence the secondary flux magnitude and angle, and therefore the machine torque as follows from (4.7). A suitable sequence of zero and active switching vectors can be applied to the secondary terminals to obtain the required flux-linkage locus and keep the modulus of the stator flux-linkage space vector within a user-specified hysteresis band (bounded by the two circles in Figure 4.5) [4,2].

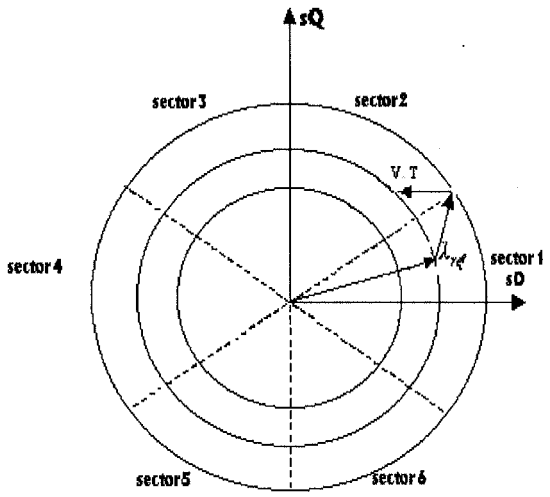

Figure 4.5 Sectors of flux linkage with hysteresis band

As shown in Figure 4.4, the secondary flux-linkage space vector can be termed the integral of the secondary–voltage space vector if the secondary winding resistance can be ignored. The case indicated in the figure above is the voltage vector ($\mathbf{V}_4$) decreasing the modulus and increasing the stationary frame angle (and hence the angle δ in Figure 4.1) of the secondary flux. Of course, if some other voltage vectors are applied, the net effect can be totally different. Consequently, both the magnitude of secondary flux and the developed torque can be directly controlled by a proper selection of voltage space vectors, that is, the selection of consecutive inverter states in order to minimise the inverter switching losses. The rules of voltage vectors over flux can be generalised as follows [93,95]:

- Non-zero voltage vectors whose misalignment with the stator flux vector does not exceed ±90° cause the flux to increase.

- Non-zero voltage vectors whose misalignment with the stator flux vector exceeds ±90° cause the flux to decrease.

If the stator flux-linkage space vector lies in the k-th sector, where k = 1,2...6, its magnitude can be increased by using the switching vectors u_k, u_{k-1}, u_{k+1}; however, the magnitude is decreased if the switching vectors $u_{k+2}, u_{k-2}, u_{k+3}$ are applied. Only one optimum vector will be chosen at the basis of minimum switch quantity. This is illustrated in the example of Figure 4.5, where the reference value of the stator flux-linkage space is λ_{ref}.

It can be seen from (4.7) that the torque is proportional to a sine of the flux angle in the secondary rotating frame (Figure 4.1) i.e. sinδ. It can therefore be concluded that the voltage vector in advance of the direction of the flux linkage rotation will increase electrical torque (by increasing δ) while the voltage vector behind the direction of the flux linkage will cause the instantaneous torque to decrease. It should be noted that the mutual primary to secondary flux (λ_{ps}) vector is nearly stationary during a short transient and especially due to the fact that this vector is rotating at ω_s, which is generally small. This phenomenon is obviously analogous to the induction machine case where the rotor winding can be said to play the role of the secondary BDFRM winding and vice-versa. A similar dual relationship can be of course established between the stator winding of the induction machine and the primary winding of the BDFRM.

A suitable look-up table can be made to summarise the effects the secondary voltages have on the secondary flux and torque magnitudes for a particular sector dependence of the flux vector. The inputs to the switching look-up table should be the results of comparison between the reference values and estimated flux and torque. The output of a two-level flux comparator can be defined as [39]:

$$d\lambda = \begin{cases} 1, & \lambda_{ref} - \lambda \geq \Delta\lambda \\ 0, & \lambda_{ref} - \lambda \leq -\Delta\lambda \end{cases} \tag{4.11}$$

and that of a three-level torque comparator as [2,4]:

$$dT = \begin{cases} 1, & T_{ref} - T \geq \Delta T \\ 0, & T_{ref} - T = 0 \\ -1, & T_{ref} - T \leq -\Delta T \end{cases} \tag{4.12}$$

where $\Delta T > 0$ and $\Delta\lambda > 0$ indicate the half width of the torque and flux hysteresis bands respectively. As shown in Figure 4.4, accurate knowledge of the secondary flux vector position is crucial in order to properly determine the voltage vector to be applied so that a desired control action is achieved. The relevant voltage vectors for a particular combination of the comparators' outputs and depending on a sector in which the secondary flux phasor is located are given in the following table. Notice that Table 4.1 is optimum in the sense that it allows the minimum switching frequency and related losses. Note also that the same look-up table is used for

induction machines with DTC. This is not surprising given the fact that the same torque expression is applicable to both machines. It is interesting however that this is the case despite the fundamentally distinct operating principles of the machines.

Table4.1. Optimum voltage switching look-up table

$d\lambda$	dT	$\alpha(1)$ I	$\alpha(2)$ II	$\alpha(3)$ III	$\alpha(4)$ IV	$\alpha(5)$ V	$\alpha(6)$ VI
1	1	u_2	u_3	u_4	u_5	u_6	u_1
	0	u_7	u_0	u_7	u_0	u_7	u_0
	-1	u_6	u_1	u_2	u_3	u_4	u_5
0	1	u_3	u_4	u_5	u_6	u_1	u_2
	0	u_0	u_7	u_0	u_7	u_0	u_7
	-1	u_5	u_6	u_1	u_2	u_3	u_4

In Table 4.1, the symbol $\alpha(n)$ indicates a particular 60^0 section centered around the attributed voltage vector position. For example, $\alpha(1)$ encompasses the area from -30^0 to $+30^0$ the associated voltage vector being U_1 (100). It is extremely important to exactly identify the meanings of '1', '0' and '-1' in (4.12) and the actions of the respective switching vectors. The function of row '1' vectors is to increase the machine instantaneous torque in its actual (not absolute) sense where the assumption is that the torque is positive if acting counter-clockwise. The function of '-1' vectors is opposite to '1' ones i.e. they decrease the machine instantaneous torque in its actual sense. However, the influence of '0' vectors on the machine torque variations is

ambiguous and is subject to the rotor speed value: if the machine is operated above the synchronous speed ($\omega_s > 0$ in this region) they allow torque decrease; else, i.e. at sub-synchronous speeds when $\omega_s < 0$, the torque would increase. The correct interpretation of the conditional relationships in (4.12) implies that the torque comparator is latched as long as one of the remaining two conditions becomes satisfied when dT is changed accordingly. This effectively means that for super-synchronous speed operation, the torque is controlled within the bottom half band using '0' and '1' vectors; in the sub-synchronous mode, on the other hand, '0' and '-1' vectors are applied to keep the torque within the top half band. If the torque is out of the band then '1' or '-1' vectors are used to pull it back in. These influences of switching voltage vectors on the machine instantaneous torque for both directions of rotation i.e. positive (anti-clockwise, $\omega_{rm} > 0$) and negative (clockwise, $\omega_{rm} < 0$) will be further discussed in Chapter 6.

A simplified block diagram in Figure 4.6 (the flux and torque estimation value calculated from equations developed from (4.2) and (4.3);) and shows how the DTC algorithm works. The torque and flux are calculated from measurements to be input to the comparators together with the desired values. The look-up table is the key part of the controller. The output of this look-up table will determine which voltage vector will be applied.

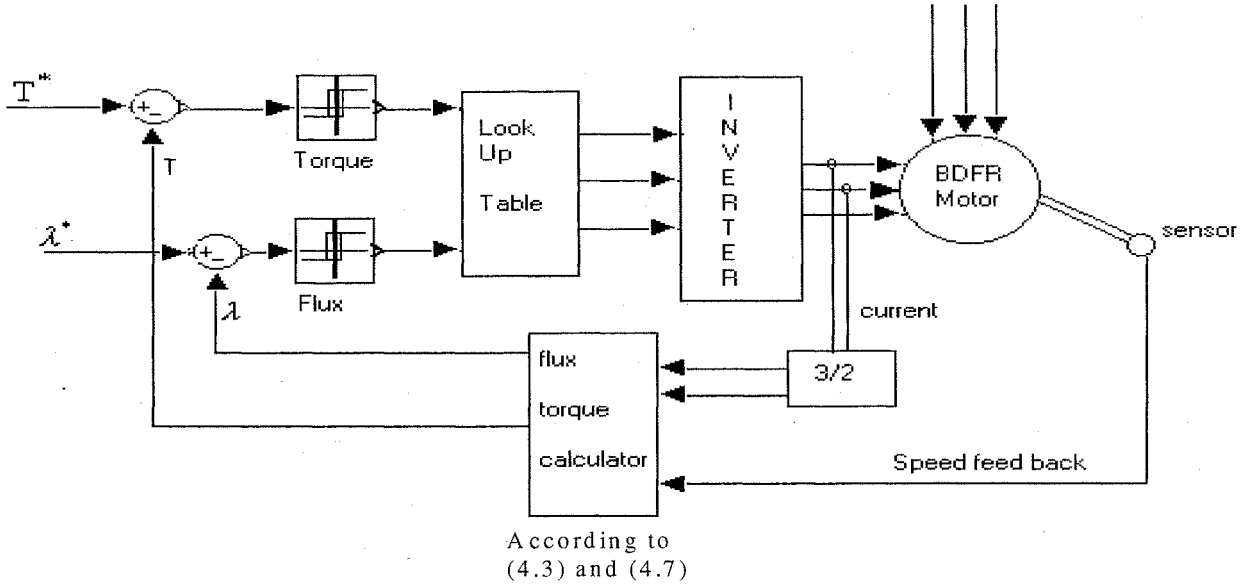

Figure 4.6 Block diagram of DTC of BDFRM

The most serious problem with a traditional DTC induction motor drive is the low speed (down to zero) operation. There are a few reasons which contribute this problem. Literature reports can be found in terms of flux estimation technique, switching methods to improve the performance at low speed region as described in Chapter 2. In Chapter 3, the close similarity has been noticed between mathematical models of induction drive and BDFRM. If the same look-up table is to be used in the control of BDFRM, it is expected then to have some problem in achieving the instant control at synchronous speed ($\omega_s = 0$) or the region around synchronous speed.

It is advised that estimators or observers should be used to get the accurate value of resistance. To avoid the problem of on-line estimation, other methods might make use of some detected current values. Apart from the improvement of flux estimation techniques, the switching look-up table can be adapted. This will be discussed in the

following Chapter (Chapter 6). It is impossible though to get the flux totally parameter independent. The accuracy of the monitored voltages and currents might have errors due the hardware problem, magnitude errors due to the conversion factors and gain, offsets in the measurement system, quantisation errors in the digital system and etc.

4.3 Conclusions

This chapter has focused on the application of the traditional Directly Torque Control (DTC) theory to the BDFRM. The reason for considering this control method for this particular machine is mainly to improve its transient response, which is inherently sluggish due to the unusual operating principle and large leakage inductances compared to conventional machines, foremost the cage induction motors. It has been shown that there is a close modelling similarity between the BDFRM and the induction machine despite their totally different torque producing mechanisms. This analogy has significantly facilitated the development of the DTC algorithm for the BDFRM. In fact, the well-established DTC principles for induction machines have served as a basis in this development. Although the switching look-up tables applicable to the induction machines can largely be used for the BDFRM some modifications are necessary to account for the fact that the doubly-fed machine can operate in steady-state as a motor (or a generator) in both super-synchronous (above synchronous speed) and sub-synchronous (below synchronous speed) modes. In other

words, at super-synchronous speeds the primary and secondary fields are rotating in the same direction and the torque is developed in much the same manner as in induction or any other traditional machine. However, if the BDFRM speed is below the synchronous value this is not the case and the two fields are counter-acting each other rotating in the opposite directions. However, despite this, the primary flux coupling the secondary winding (which is participating in the electro-mechanical energy conversion) is still rotating in the same direction as the secondary winding mmf (as a result of the rotor modulating action) so that the machine can produce motoring torque (to support rotation) even in this speed region. It is well known that this is not possible with the cage induction machines, which is under dynamic braking (transient) conditions whenever the stator and rotor revolving fields are of opposite sign.

Aspects of implementation of the proposed DTC scheme will be discussed in the following chapters, specifically in Chapters 7 and 8, which present simulation and experimental results respectively. A thorough analysis of the algorithm structure is performed in Chapter 6 which deals with simulation studies.

Chapter 5 Sensorless Control

Some drive control methods do not require a closed-loop control algorithm. For example, induction machines for low performance (general purpose) applications can be controlled by the open-loop V/f method. Within a closed-loop control system, feedback is used to minimise the difference between the actual and demanded outputs with the main control variable being either the angular velocity or shaft position. The overall performance of the system is then largely dependent on the quality of feedback information, which can be obtained either using some sort of a shaft position/speed sensor (such as an encoder or resolver) or by applying appropriate sensorless estimation techniques. For the experimental test system considered in this thesis, a high precision incremental encoder has been used (relevant details can be found in Appendix B.3).

The thesis examines both sensor and sensorless control of BDFRM based on Matlab®/Simulink®. In simulation, the rotor position information may be retrieved directly from the machine model (rotor) if a sensor control mode is chosen. However, the primary focus of this chapter is on sensorless control aspects. In this case, estimation techniques make use of the machine model to determine the rotor speed or position from measurements of the current and/or supply voltage. Clearly, the estimation technique is machine parameter dependent and practical effects, such as magnetic saturation and stator resistance variation as well as noise and quantisation

errors, may have a significant impact on the control accuracy. This chapter develops expressions for on-line estimation of rotor position and angular speed of the BDFRM and discusses the main features of the associated estimation technique, its advantages and limitations. The entire sensorless control algorithm and its main functional components are outlined in the later chapters. The influence of ignoring the stator resistance on the quality of flux estimates is also considered in the following.

5.1 Sensor Control

High performance control (FOC for example) of the BDFRM (or any other machine) requires an accurate knowledge of rotor position to convert the measurable stator frame quantities into their rotating counterparts. Even in the case of Direct Torque Control (DTC), which has no rotating frame transformation, knowledge of the rotor speed is extremely important for the control. The most common approach is the direct measurement of the rotor position by means of optical encoders (either incremental or absolute) or by using devices applying electromagnetic principles (inherently absolute). The electromagnetic solution is often preferred for synchronous machines due to the need for absolute rotor position feedback in order to achieve decoupling [55]. While it is true that the use of sensors increases the system cost, the main limitation is certainly the reduced system reliability by the presence of cables connecting the sensor with the control computer, especially if the latter is remotely located (for example, in submersible or similar environmentally hostile applications).

However, in most cases these deficiencies are offset by the much better performance that can be achieved compared to sensorless controllers.

Optically based encoders are widely used for position measurements. An encoder with a single track will allow the magnitude of the speed to be measured; the direction of rotation will be determined by the addition of a second track or an additional sensor to produce a quadrature signal. The speed and position are measured using pulse-counting techniques, the resolution being determined by the size of the counter and the encoder. The number of lines per rotation specifies an encoder's resolution. Thus an optical encoder usually having 1024 signals per revolution and two rectangular pulse trains can be used to measure the rotor position. The phase shift between the two pulses is dependent on the direction of rotation. However since the two channels of encoder are shifted by 90 electrical degrees, it is possible to divide each encoder cycle into four. The details of the encoder can be found in Chapter 8 and Appendix B.3.

Neither sensor nor sensorless technology measures velocity directly. To estimate velocity from position measurements, some form of recursive algorithm based on past position is generally used. Such algorithms are implemented either via hybrid analogue/digital hardware or via software [57].

To estimate velocity, the least complicated algorithm is based on the same form as the differential calculus limit definition of the derivative (known as Euler's

approximation):

$$\omega(k) = \frac{\theta(k) - \theta(k-1)}{T} \tag{5.1}$$

where T is the sampling time interval for the velocity loop, and k is the sample index number. It is important to point out the following two important aspects of (5.1):

Accuracy. It is only estimating the average velocity over the previous sample interval. During instantaneous periods caused by a sudden change in demanded torque, such an estimate will clearly be in error. The quality of this information will be dependent on the sampling frequency; if the interval 'T' is too small, it will require higher calculation speed and might produce numerical error. Generally the machine is running in steady state, therefore, the optimised sampling frequency should be selected to provide the most accurate information in both steady and dynamic states.

Quantization. The coarseness of the velocity resolution is limited directly by the angular resolution of the position transducer and the sample time.

This type of estimator is often improved by digitally filtering the past values by using appropriate real number filter coefficients (which will introduce time delay). Both Finite Impulse Response (FIR, moving average) and Infinite Impulse Response (IIR, recursive) digital filters may be used for this purpose. Such filtering will produce a velocity resolution improvement but the instantaneous accuracy is still compromised by using older position samples. At steady state velocities, such an approach can

produce a very accurate, high-resolution velocity estimates. The transient performance during acceleration is however compromised in order to achieve this [58,70].

5.2 *Sensorless Control*

5.2.1 INTRODUCTION

In the BDFRM case, one favourable feature is that the rotor position can be estimated from the flux equations owing to the fact that both machine sides are externally accessible. This means that the use of an encoder can be avoided in the control system. The use of observers to estimate unmeasured variables offers a significant advantage over classical estimators in both accuracy and quantisation. To understand the reason for this improvement, it is instructive to review some of the basic principles of observer theory [58].

The mathematical model (Chapter 3) of the BDFRM has been built on an ideal linear assumption. The primary flux expression in a stationary reference frame, as shown before[64], can be written as:

$$\boldsymbol{\lambda}_{ps} = L_p \mathbf{i}_{ps} + L_{ps} \mathbf{i}_{ss}^{*} e^{j\theta r} \tag{5.2}$$

Rearranging gives:

$$e^{j\theta_r} = \frac{\boldsymbol{\lambda}_{ps} - L_p \mathbf{i}_{ps}}{L_{ps} \mathbf{i}_{Ss}^{*}} \Rightarrow \theta_r = \ln \frac{\lambda_{ps} - L_p i_{ps}}{L_{ps} i_{Ss}^{*}} \tag{5.3}$$

in which λ_{ps} is mutual flux and it can be estimated by formula $\lambda_{ps} = \frac{L_{ps}}{L_p} \lambda_p$. It is obvious from (5.3) that the rotor position is the angular difference between the vectors $\boldsymbol{\lambda}_{ps} - L_p \mathbf{i}_{ps}$ and $L_{ps} \mathbf{i}_{Ss}^{*}$, and that the respective expression is dependent on the machine

inductances. Therefore, apart from the noise effects in the measurements, the accuracy of the inductance L_p and the mutual inductance L_{ps} estimates, obtained by off-line testing (see Appendix A.1), has a direct influence on the estimated position value.

The position estimates generated by using (5.3) can be fed as an input to an angular velocity observer to predict the machine speed [2,33]. The observer algorithm is derived from the conventional mechanical equation:

$$T_e = J\frac{d\omega}{dt} + T_{load} + f\omega \tag{5.4}$$

where J is the inertia constant of the drive system (machine and load) and f here represents the friction coefficient. The corresponding block-diagram is shown in Figure 5. 1.

Since there is no information of load torque to feed into the observer, the gains K_1, K_2 and K_3 have to be appropriately adjusted and should be high enough in order to successfully reject this unknown load disturbance and achieve a fast observer response. High estimation accuracy, insensitivity to both model and load parameter errors, and compensation for the state disturbances caused by a load torque T_{load} can be accomplished using the estimated position feedback and position error integrator. One should also mention that the same observer algorithm is effectively a low pass filter providing not only the instant velocity estimates but also predictions for rotor position.

In the sensorless DTC application, the dynamic performance of the observer has to be

compromised to some extend because of the noisy θ_{est} estimates produced by the position estimator. Therefore the observer gains have to be tuned with this in mind. The convergence of the control algorithm and machine operating stability are simply a matter of appropriately tuning the gains, the main criteria being the quality of θ_{est}. If the estimates are known to be accurate then the feedback gain is increased, otherwise it is decreased. Clearly this implies that gain scheduling is required to obtain good estimates throughout the entire speed range of the machine.

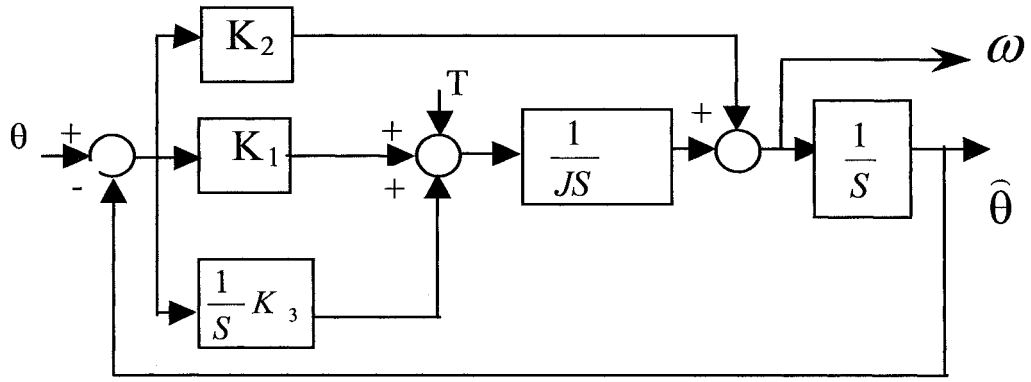

Figure 5. 1 Block diagram of the velocity and position observer

From control theory, the expression of this block diagram in time domain can be written as:

$$\dot{\hat{\omega}} = \frac{T_e}{J} + \frac{K_1}{J}(\theta - \hat{\theta}) + K_3 \int (\theta - \hat{\theta}) dt - b\frac{\hat{\omega}}{J} \tag{5.5}$$

Since the friction is very small in comparison to the load torque, b is generally set to zero. K_2 is set to zero as well in this case.

The open-loop observer can be thought of as a real-time simulation of the physical system, which is running in parallel with the actual system. The simulation (observer)

is receiving the same manipulation or control inputs as the actual system. This is based on command feed forward theory, which is equivalent to using the dynamic equation of motion to calculate the instantaneous torque needed to follow a command trajectory. The resolution of such open-loop observers is limited only by the numerical resolution of the simulation computations. Such resolution can easily be designed to be superior to the feedback device. The limitation of this open-loop approach is that it is only correct when the observer model and its parameters are identical to the actual physical system. Thus they are parameter dependent.

The merit of using an observer is that both angular velocity ω and position θ can be accurately predicted without any knowledge of past information. This means that there is no filter delay, which is crucial for high performance control. A digital form of the filter is implemented using an optimal sequence of forward and backward approximations for the three integrators so that the delay through the algorithm is reduced to a minimum. This type of observer is clearly superior to either classical filtering or recursive estimation approaches for this application [33]

It should be noted however that although a sensorless BDFRM drive is undoubtedly lower cost and more mechanically robust, there is a control performance trade-off when compared to the sensed drive. Furthermore, real time implementation of sensorless algorithms is generally more complicated and consequently only a few experimental schemes are available in the literature [7,25,97].

The details of sensorless control algorithm and the corresponding simulation results are studies in Chapter 7.

5.2.2 ASPECTS OF OBSERVER PRACTICAL REALISATION

A powerful dSPACE® DSP system will be used for real time implementation of the developed controller. The most significant advantage of all the dSPACE® platforms is their compatibility with Matlab®/Simulink® environment and user-friendly input/output interface. One limitation of the version 3.4 dSPACE® used is that the associated real-time compilers do not accept any user-programmed functions. This limitation requires the entire model to be based on the functional blocks available in the dSPACE® (i.e. Simulink®) library.

The block diagram of Figure 5.1 reveals the principle of the speed estimator. Note that if the model is simulating unloaded conditions, i.e. $T_{load} = 0$, and the values of $K_{2,3}$ are to be set to zero, this diagram in fact represents the mechanical equation (5.4).

5.2.3 Sensorless Control Algorithm

The heart of the simplified sensorless algorithm for the BDFRM (Figure 5. 2) are the position and torque estimators, both based on the mathematic model of Chapter 3. The functionality of the respective two blocks (flux and torque) will be discussed in detail in the Section 7.2, Chapter 7.

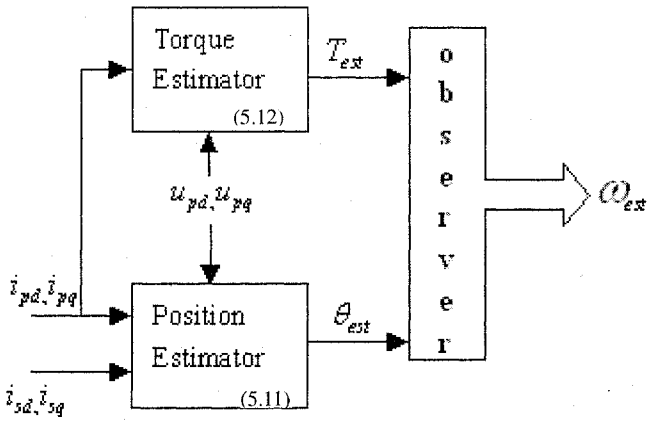

Figure 5. 2 A conceptual block diagram of the observer-based sensorless scheme

5.3 Stator Resistance Effects

Owing to the hysteresis ('bang-bang') control of flux and torque, DTC is capable of producing a fast machine response despite its inherent simplicity. One of the main, well-known, limitations of the DTC is the use of a back-emf based approach for the estimation of stator flux (either primary or secondary in the BDFRM). The temperature variation of stator resistance introduces errors in the flux linkage vector (and indirectly in the torque estimates) and deteriorates the drives performance at lower applied frequencies of the inverter-fed (secondary) winding of the BDFRM when the resistive voltage drop becomes comparable to the secondary supply voltage magnitude. Several control schemes have been proposed for induction machines to overcome the problem of stator resistance variation [8,9].

In this section, the influence of stator resistance variations on the stator flux linkage of the BDFRM has been examined. The initial study shows that the drive system may

become unstable if the stator resistance used in the primary flux estimator differs from the actual value. The potential use of PI compensation can minimise the problem to a very large extent [70].

In a DTC drive, the stator flux is estimated by integrating the back-emf. If there is no change in R_s, the actual stator flux (λ_s), estimated stator flux (λ_{est}), the actual torque (T), and estimated torque (T_{est}) of the machine are given by (using standard notation):

$$\lambda_s = \lambda_{est} = \int (\mathbf{v}_s - \mathbf{i}_s R_s) dt \tag{5.11}$$

$$T = T_{est} = \frac{3}{2} P_r (\mathbf{i}_{qs} \lambda_{ds} - \mathbf{i}_{ds} \lambda_{qs}) \tag{5.12}$$

If the stator resistance of the motor changes by ΔR, a change of $\Delta \mathbf{i}_s$ will result in the stator current vector $\mathbf{i}_s$. The corresponding variations of the respective d- and q-axes currents are $\Delta \mathbf{i}_{ds}$ and $\Delta \mathbf{i}_{qs}$, respectively. If the controller uses the unchanged value of resistance for calculations while the actual motor resistance has changed the actual variables will be:

$$\lambda_{ds} + \Delta\lambda_{dsm} = \int [\mathbf{v}_{ds} - (\mathbf{i}_{ds} + \Delta \mathbf{i}_{ds})(R_s + \Delta R_s)] dt \tag{5.13}$$

$$\lambda_{qs} + \Delta\lambda_{qsm} = \int [\mathbf{v}_{qs} - (\mathbf{i}_{qs} + \Delta \mathbf{i}_{qs})(R_s + \Delta R_s)] dt \tag{5.14}$$

$$\lambda_s + \Delta\lambda_s = \int [\mathbf{v}_s - (\mathbf{i}_s + \Delta \mathbf{i}_s)(R_s + \Delta R_s)] dt \tag{5.15}$$

$$T_e + \Delta T_e = \frac{3}{2} P_r [(\mathbf{i}_{qs} + \Delta \mathbf{i}_{qs})(\lambda_{ds} + \Delta\lambda_{ds}) - (\mathbf{i}_{ds} + \Delta \mathbf{i}_{ds})(\lambda_{qs} + \Delta\lambda_{qs})] \tag{5.16}$$

The estimated controller variables are:

$$\lambda_{ds} + \Delta\lambda_{dest} = \int [\mathbf{v}_{ds} - (\mathbf{i}_{ds} + \Delta\mathbf{i}_{ds})R_s]dt \tag{5.17}$$

$$\lambda_{qs} + \Delta\lambda_{qest} = \int [\mathbf{v}_{qs} - (\mathbf{i}_{qs} + \Delta\mathbf{i}_{qs})R_s]dt \tag{5.18}$$

$$\lambda_s + \Delta\lambda_{est} = \int [\mathbf{v}_s - (\mathbf{i}_s + \Delta\mathbf{i}_s)R_s]dt \tag{5.19}$$

$$T_e + \Delta T_{est} = \frac{3}{2} P_r[(\mathbf{i}_{qs} + \Delta\mathbf{i}_{qs})(\lambda_{ds} + \Delta\lambda_{dest}) - (\mathbf{i}_{ds} + \Delta\mathbf{i}_{ds})(\lambda_{qs} + \Delta\lambda_{est})] \tag{5.20}$$

The errors in the estimated flux linkage and torque from the actual flux linkage and torque of the motor can be expressed as:

$$\Delta\lambda_{ds} = \Delta\lambda_{dsm} - \Delta\lambda_{dest} = \int (\mathbf{i}_{ds} + \Delta\mathbf{i}_{ds})\Delta R_s dt \tag{5.21}$$

$$\Delta\lambda_{qs} = \Delta\lambda_{qsm} - \Delta\lambda_{qest} = \int (\mathbf{i}_{qs} + \Delta\mathbf{i}_{qs})\Delta R_s dt \tag{5.22}$$

$$\Delta\lambda_s = \Delta\lambda_s - \Delta\lambda_{est} = \int (\mathbf{i}_s + \Delta\mathbf{i}_s)\Delta R_s dt \tag{5.23}$$

$$\Delta T_e = \Delta T_{ec} - \Delta T_{est} = \frac{3}{2} P_r[(\mathbf{i}_{qs} + \Delta\mathbf{i}_{qs})\int (\mathbf{i}_{ds} + \Delta\mathbf{i}_{ds})\Delta R_s dt - (\mathbf{i}_{ds} + \Delta\mathbf{i}_{ds})\int (\mathbf{i}_{qs} + \Delta\mathbf{i}_{qs})\Delta R_s dt] \tag{5.24}$$

Equations (5.23) and (5.24) represent the errors in stator flux linkage and torque due to the change of stator resistance. The estimated stator flux and torque may differ significantly from their actual values, which may deteriorate the overall performance of a DTC system. Errors in the stator flux vector position are generally more significant as they can cause the controller to select a wrong switching state often compromising the stability of the machine operation. Therefore, accurate knowledge of the stator resistance is important.

The computer simulation plots below (Figure 5.3 – Figure 5.6) have been generated under the following conditions:

1) Before 2.5-s, the BDFRM was soft started(by short-circuit secondary windings);
2) At 2.5-s, the sensorless DTC control algorithm(explained in previous sections and Chapter 6) is applied on the machine;
3) The machine has reached steady state (specifically at 3.6-s) and the secondary stator inductance has increased by 10% when the system lost control.

To illustrate the difference, the original simulation results with constant stator resistance (Figure 5.3 for the speed response and Figure 5.5 for the flux response) are also presented for comparison. It can be seen from Figs 5.3 and 5.5 that machine corresponded the control described above. The sampling time was set to 5e-5 s. These comparable plots reveal that the observer is parameter sensitive, as predicted. The small parameters [22](for example, 0.03 H for mutual inductance) used in the machine model (due to its limited power output) have also contributed to the loss of control.

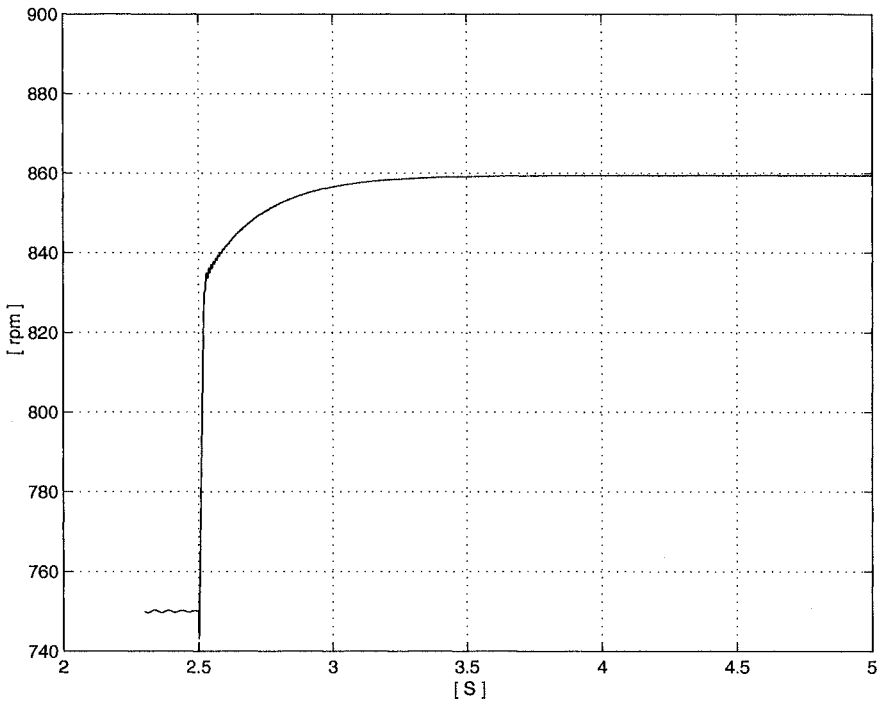

Figure 5. 3 The speed response with constant parameters

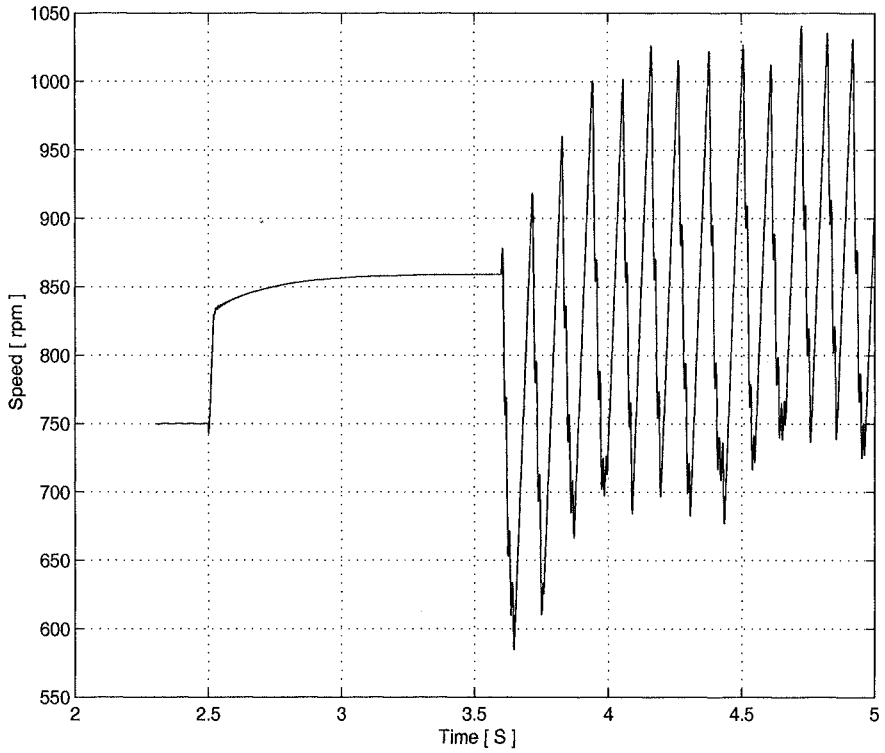

Figure 5. 4. Speed response with changed parameters

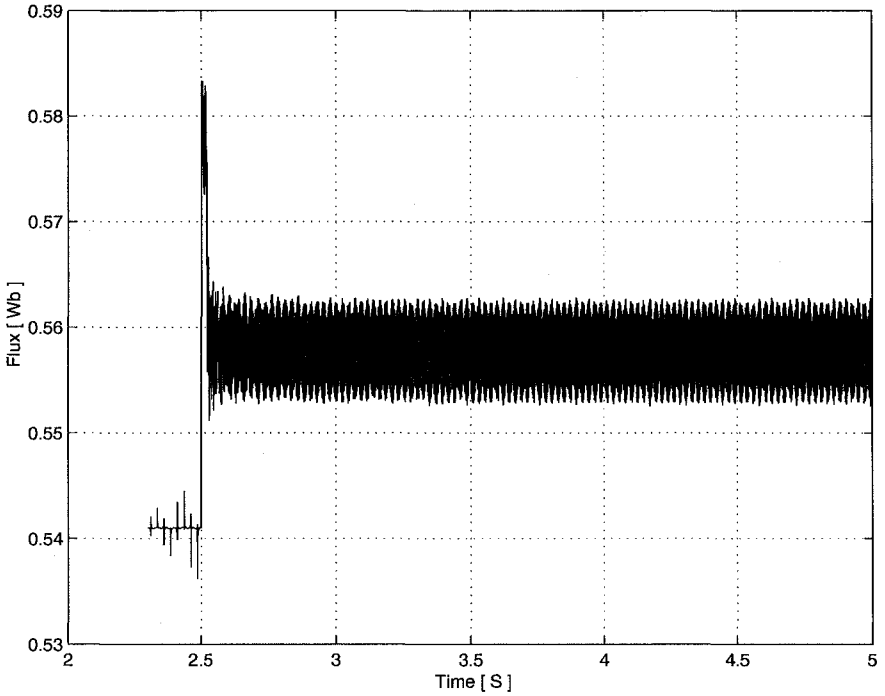

Figure 5. 5 Estimated flux with constant parameters

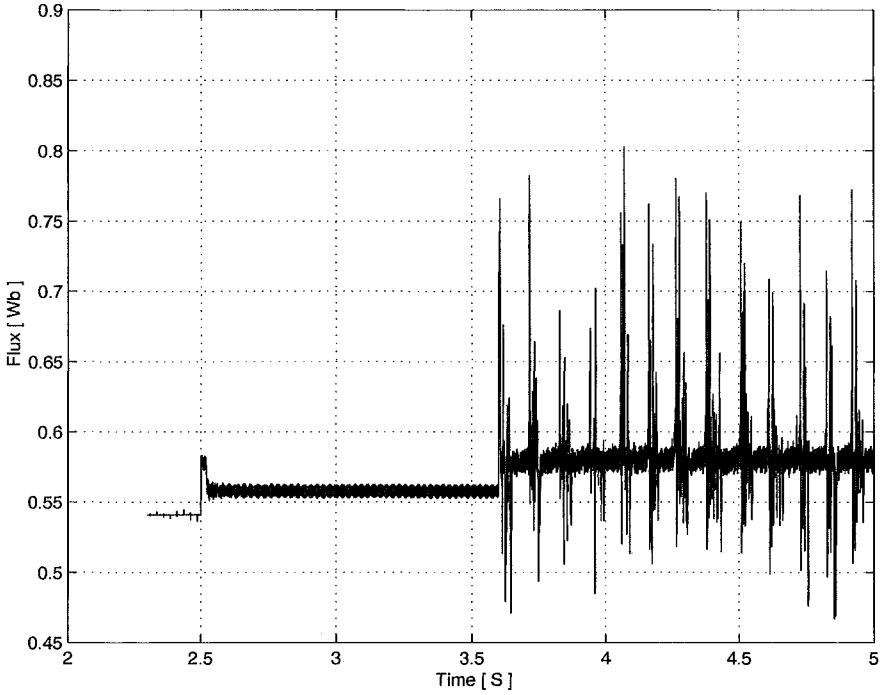

Figure 5. 6 The estimated flux with changed parameters

5.4 Conclusions

The main contribution of the work presented in this chapter is the development of a viable sensorless DTC scheme for the Brushless Doubly-Fed Reluctance Machine. The high accuracy and good performance of the algorithm, using the maximum torque per ampere control strategy as case study, are confirmed by both simulation and experimental work in the following chapters. The important conclusions and observations related to the performance aspects will therefore be made and discussed there. In this chapter, the influence of primary resistance is carefully examined.

Chapter 6 Switching Strategies Of BDFRM

While the Direct Torque Control (DTC) has been already applied to various AC machines for use in higher speed applications, this is not the case with doubly-fed machines in general. Recently, DTC was used as an alternative method to control Doubly-Fed Induction Generator [91]. Since the main target applications of the BDFRM are large pumps, mills and wind turbines [71] where only a limited variable speed capability is required, the secondary supply frequencies are low and therefore some modifications to the original DTC approach [4] (suffering from voltage integration problems in this frequency range) are necessary to allow stable machine operation around synchronous speed under different loading conditions. Fortunately, and unlike cage induction and other conventional singly-fed motors, it is possible to achieve this objective with the BDFRM owing to its double feeding and the fact that both its sides are externally accessible.

Building upon a correct understanding of the traditional DTC principle for induction machines [2,4,87], several switching strategies, suitable for low secondary frequency operation of the BDFRM, are proposed in this chapter. Three possible DTC methods are considered: the first one is to use the traditional DTC look-up table for induction machines based on three-level torque and two-level flux hysteresis comparators; the

second approach is simplified in the sense that it replaces a 3-level torque relay with a two-level one; finally, the third 'hybrid' method is a combination of the two. A comparative performance analysis of the proposed DTC strategies is carried out foremost in terms of transient response they offer, their structural complexity and ease of digital implementation using the DSP development platforms from dSPACE®. The specific performance indicators considered include the machine speed, the electromagnetic torque and the secondary flux. A particular attention is being paid to the machine synchronous speed operation when the secondary winding is DC fed i.e. when the secondary applied frequency is zero. It is well known that under these conditions it is virtually impossible to achieve viable DTC (or any other back-emf based control) of cage induction motors. It will be shown however that the BDFRM is superior to the induction machines in this respect. In the BDFRM case, it turns out that the second approach above is the most suitable due to its simplicity and the possibility of using readily available functional blocks from the dSPACE® library. This convenience means that any compilation problems (which are normally present if user-made functional subroutines, such as a three-level comparator, are used) while uploading Simulink® programmes to the dSPACE® system for real-time implementation can be avoided (or at least reduced to a minimum) in this way. Furthermore, the simplified torque look-up table will enable the improved machine performance and faster transient response over the entire speed range of interest down to synchronous speed than using the traditional look-up table (i.e. the first method identified previously). Because of these inherent advantages, this simplified switching

strategy has been used to generate the simulation and experimental results presented in this and the following chapter(s).

It will be shown that with modified DTC method the BDFRM can achieve the fast dynamics, the most important advantage being the possibility of stable operation down to zero secondary frequency. In this sense, the work to be presented can serve as a starting point for DTC research not only on the BDFRM but also on the Doubly Excited Wounded Rotor Induction Machine (DEWRIM) due to close modelling similarities of these two conceptually different machines.

6.1 The Traditional DTC

A detailed discussion of the fundamental DTC theory can be found in Chapter 4. It has been concluded in that chapter that an identical optimum look-up table as the one used in for cage induction machine can be applied to the BDFRM according to the established DTC principles and close similarities between the two machines. A simulation model was built based on the block diagram shown in Figure 5. 1 of Chapter 5.

Simulink® programmes have been developed to evaluate the theoretical performance of the switching strategies proposed above.

The computer simulation plots in Figure 6.1-6.3 are for the machine operated in torque mode (with no speed feedback). The machine model is using parameters from [22] and the details can be found in Appendix A. Prior to the inverter being connected with the control enabled, the machine has been started with the shorted secondary terminals in a manner similar to a conventional wound rotor induction machine (the machine starting dynamics can be seen before 1-s in plots),. After reaching steady state and connecting the inverter at 2.5-s, both the load and reference torque are simultaneously set to 5 Nm. It can be seen in the corresponding speed plot presented in Figure 6.3, that due to fast and accurate torque control there is virtually no speed variation. At 3 s the machine is unloaded but the reference torque is kept at 5 Nm. Due to a positive acceleration torque developed, the machine will speed up until loaded again at 5 Nm. At 3.5 s the load torque suddenly changed to 10 Nm with the command torque maintained at 5 Nm, which will result in the speed decrease to a sub-synchronous value. Then at 3.6 s, the torque reference is set to 10 Nm so that a new steady state is reached in sub-synchronous mode as shown in Figure 6.3.

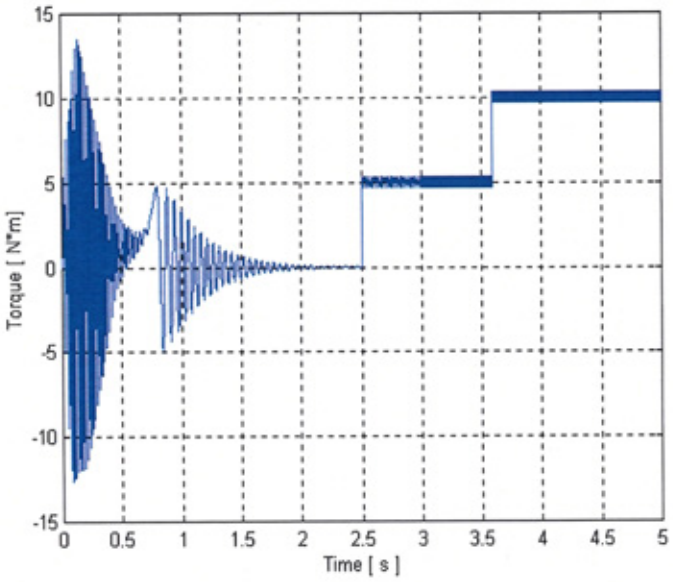

Figure 6.1: Torque plot of BDFRM

It is important to stress the fact that the example machine has responsed to sudden load/reference torque changes. This is visible from Figure 6.1 and confirms the advantage of DTC control. Both the hysteresis bands (for torque and flux) are set to 5% above and below the respective reference values. The step size of the control is 5e-5 s, which means the highest switching frequency of 20 KHz allowing excellent dynamic performance. It will be shown in the following chapter that a similar control rate can be achieved on a real machine as well.

It is clear from the respective flux results in Figure 6.2 that the flux waveform is similar in shape to the torque one in Figure 6.1 as expected. What is also noticeable from the same figure is that there is very little change in flux reference for a given torque reference variation. For example, an increase of 5 Nm in torque will only cause

the flux to rise by 0.2 Wb or so. This confirms that the dominant part of the secondary flux is coming from the primary flux through mutual coupling. The mathematical explanation can be found in Chapter 7.

The secondary flux position in its own rotating frame is also detected (Figure 6.4). The result shows that the change of torque is directly related to the change of flux angle, which proves the observation made in Chapter 4 (for Equ 4.7). A similar conclusion can be made about the secondary current q-axis waveform in Figure 6.5 which is clearly very similar to those in Figures 6.1 and 6.4.

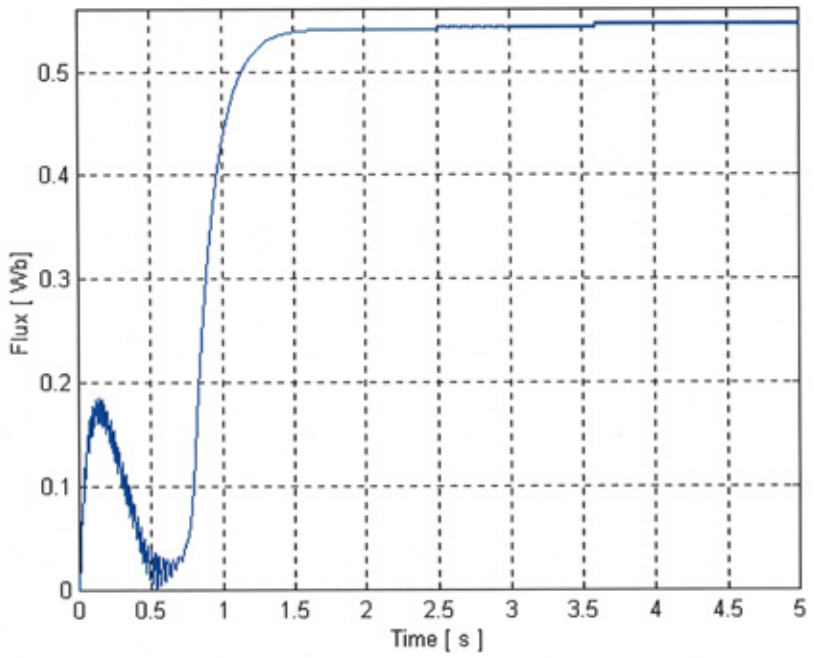

Figure 6.2 Flux plot of BDFRM DTC

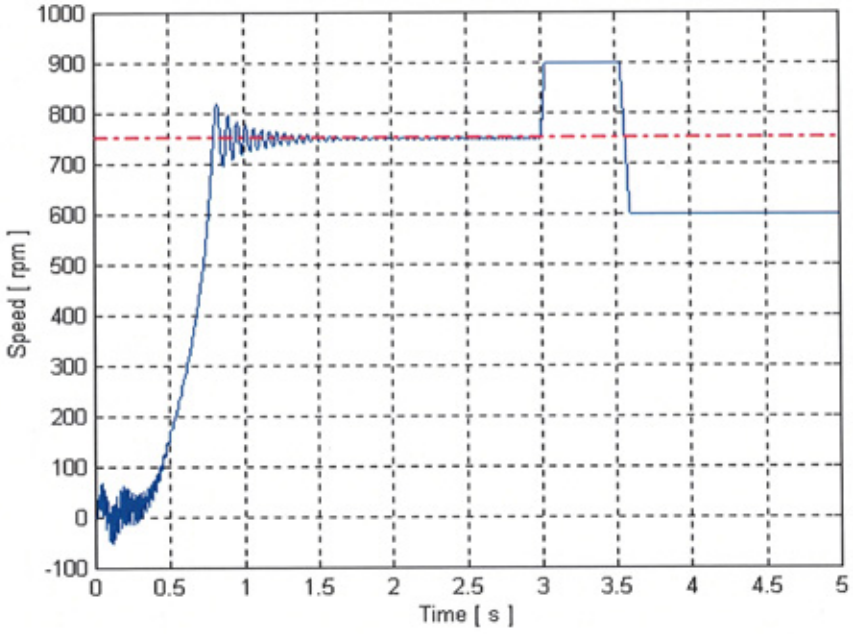

Figure 6.3 Speed plot of BDFRM DTC (dashed line at 750rpm indicates synchronous speed)

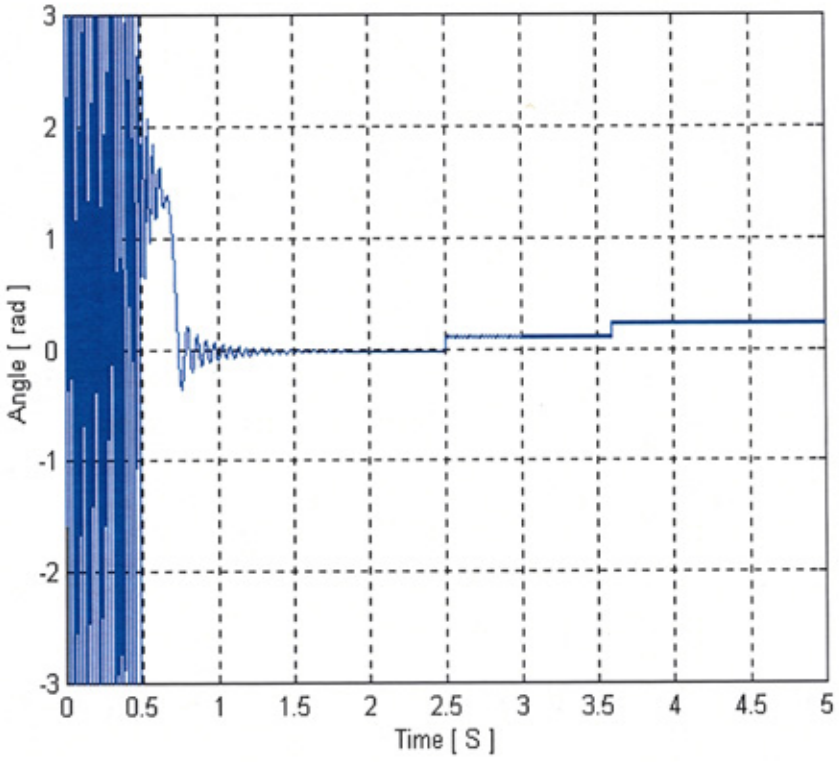

Figure 6.4 Secondary flux angle in its own frame

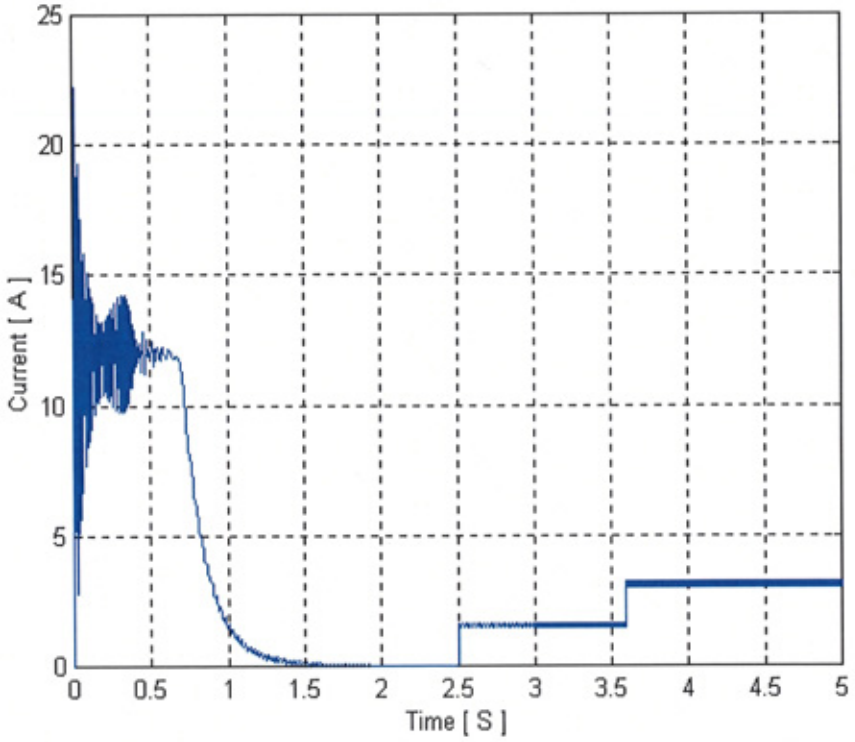

Figure 6.5 Secondary Q-axis current

The simulation results presented previously have undoubtedly demonstrated potentially good performance of the controller at either super-synchronous or sub-synchronous speeds. However, at synchronous speed and in its close vicinity, the transient response deteriorates as illustrated in Figure 6.6. It can be seen that if the machine was suddenly unloaded at 5.5 s with the reference torque changed simultaneously to zero, there is now a speed increment (refer to the zoomed portion in the same figure) of about 24rpm, which is not negligible. The reason for this is the slower torque response that is clearly visible in the zoomed area of Figure 6.7. This dynamic performance degradation can be attributed to the use of zero vectors (the secondary side is then short-circuited with either '111' or '000' binary status of the inverter legs) and nearly zero secondary back-emf in the machine operated at virtually

synchronous speed under these conditions as shown in Figure 6.6. In this case, the machine rate of change torque is dictated by the large time constant of the secondary RL circuit and is therefore generally small due to inherently higher leakage inductances of the BDFRM. It is also true that the inertia of the considered machine is quite small (0.01 kgm^2), which has further contributed to this undesirable effect. With larger machines having higher inertia constants the speed variations would be smaller. This fact indicates that for the machine operation in a narrow range around synchronous speed down to zero secondary supply frequency it would be generally better to use the active vectors only in order to achieve a reasonable high rate of change of torque and faster response.

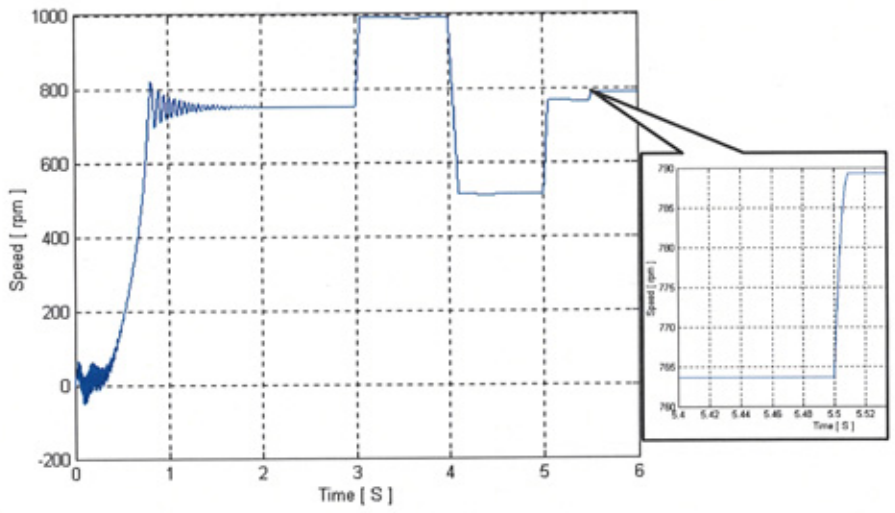

Figure 6.6 The speed plot by using zero voltage vectors

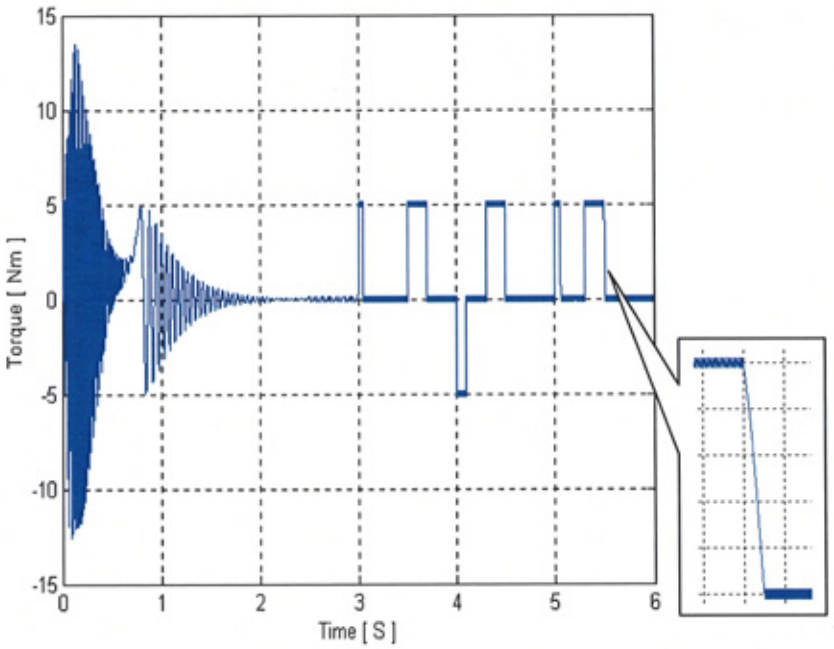

Figure 6.7 Torque response by using zero voltage vectors

6.2 *Modified Look-up Table*

As stated in the Chapter 4, the implementation doesn't need to use the zero voltage vectors, as this method not only results in the sluggish transient response at very small secondary frequencies as previously noted but also requires distinguishing between sub-synchronous and super-synchronous rotational speed, making the control unnecessarily more complicated. By omitting the zero voltage vectors, the look-up table effectively has two columns less (Table 6.1) and becomes much easier to implement using a two-level relay (readily available in the Simulink® library) especially in dSPACE®.

Tab 6.1-Improved Optimum voltage switching look-up table

$d\lambda$	dt_e	α(1) I	α(2) II	α(3) III	α(4) IV	α(5) V	α(6) VI
1	1	u_2	u_3	u_4	u_5	u_6	u_1
	-1	u_6	u_1	u_2	u_3	u_4	u_5
0	1	u_3	u_4	u_5	u_6	u_1	u_2
	-1	u_5	u_6	u_1	u_2	u_3	u_4

The main reason for applying exclusively non-zero vectors '1' or '-1' during transients is to achieve the fastest possible response from the machine. This is especially the case at lower secondary frequencies (the BDFRM is usually operated at) when there is little induced voltage to get a reasonably high rate of change of secondary current and flux (and hence torque) with the shorted windings as mentioned earlier. In this frequency region, and particularly at synchronous speed ($\omega_s = 0$) when there is no secondary back-emf at all, it is preferable to use the active vectors instead of '0' vectors even in the case when the torque is within the band. The benefits of this approach are manifold:

- The synchronous speed performance is considerably improved since with zero applied voltages, the control can be sluggish and inaccurate (or it could be

temporarily lost) as the secondary winding then behaves purely as a shorted RL circuit of a relatively large time constant[2].

- The torque comparator becomes a two level one and it can be easier implemented in both analogue and digital hardware. The software implementation using Simulink® compatible DSP development systems (such as dSPACE® for instance) is particularly facilitated, as two level comparators, unlike three level ones whose operation should be programmed, are readily available in the library. In fact, the dSPACE® Advanced Control Education (ACE) kits (see http://www.dspace.ltd.uk for details), one of which (ACE 1103) is being used in the drive prototype, are not user-friendly in the sense that they do not accept any custom-made Matlab® functions while compiling real-time codes.
- In keeping with the previous advantage, the control algorithm is much simpler as knowledge of the machine speed or operating conditions (transient or steady-state) is not required as follows from Table 6.2. This is not the case if one uses two 2-level comparators to implement traditional DTC.

The only limitation of using solely active vectors is the higher switching rate (this is almost doubled in steady-state for the same hysteresis band) and therefore increased inverter losses. From this point of view, it would be more desirable to use both zero and active voltage vectors except at very low ω_s. For example, from the first column of Table 6.1, it can be seen that two inverter legs have to change their state to allow transition from vector $\mathbf{u}_2$ (110) to $\mathbf{u}_6$ (101). If the zero row is used instead then $\mathbf{u}_2$ will

[2] The BDFRM leakage inductances are higher than with an induction machine due to the unusual operating principle in which the fundamental flux is not torque producing but appears as a leakage component.

only need to change to $\mathbf{u}_7$ (111) which requires only a single leg to be switched. Since the machine is mostly operated in steady state, it is reasonable to consider replacing ' –1' (in case of $\omega_s > 0$) and ' 1' (for $\omega_s < 0$) with '0' row vectors in Table 6.1. The developed DTC scheme in Figure 6.11 builds upon this optimised switching technique.

Table 6.2 -EFFECT OF VOLTAGE VECTORS ON BDFRM TORQUE.

DT	ω_s	Torque changes
1	>0	$\uparrow$
0	>0	$\downarrow(\omega_{rm}>0)$ $\uparrow(\omega_{rm}<0)$
-1	>0	$\downarrow$
1	<0	$\uparrow$
0	<0	$\uparrow(\omega_{rm}>0)$ $\downarrow(\omega_{rm}<0)$
-1	<0	$\downarrow$

The simulation plots (Figures 6.8-6.10) presented below have demonstrated control by using this look-up table down to synchronous speed when the secondary supply frequency is zero. These simulation studies were done in the speed mode i.e. under the closed loop conditions.

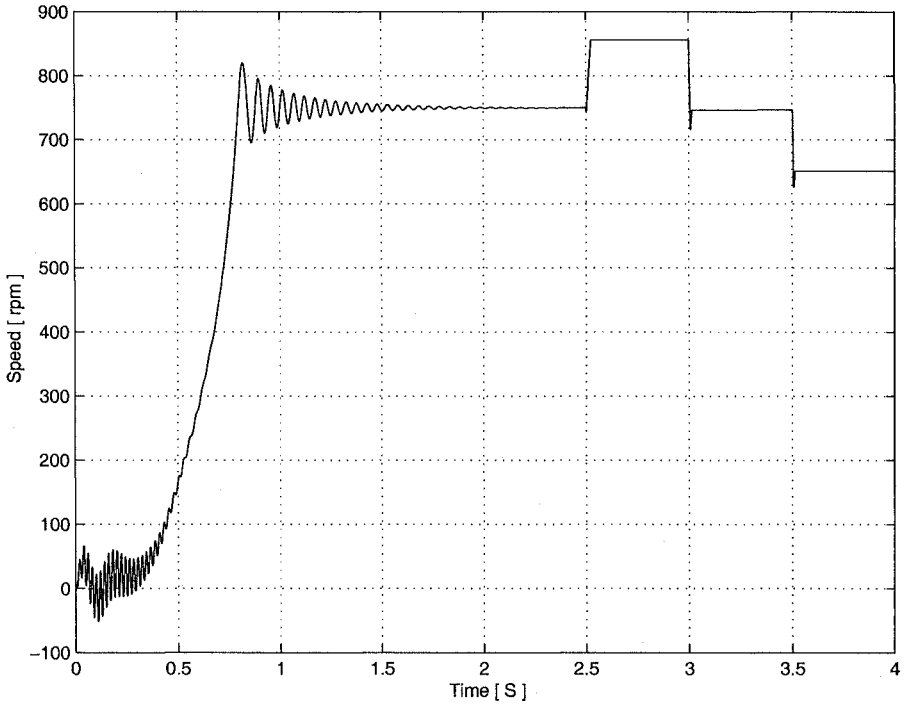

Figure 6.8 The speed plot using 2-relay look-up table

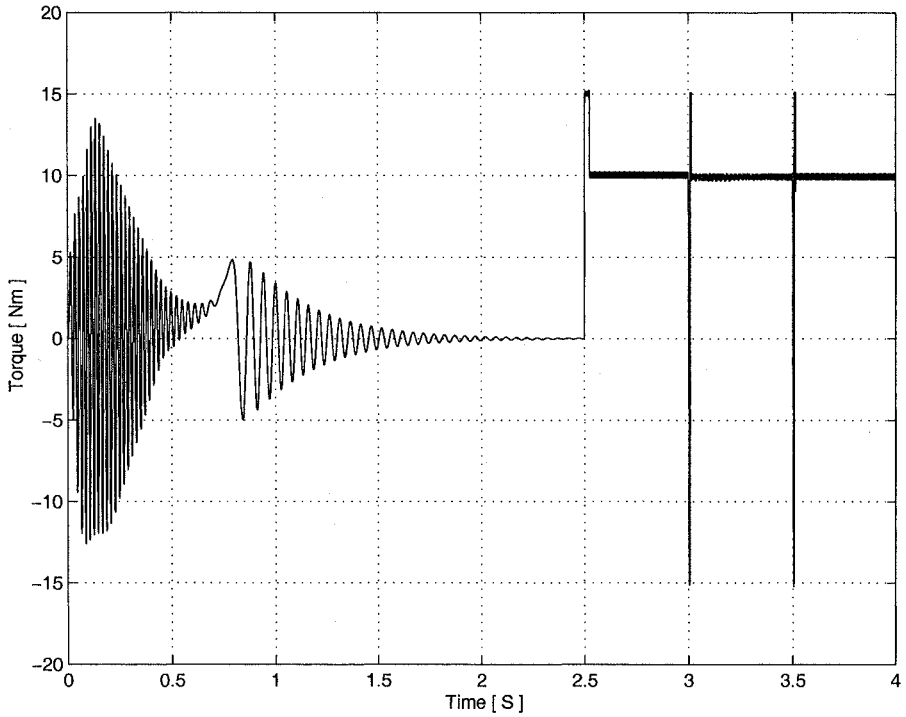

Figure 6.9 The torque plot using 2-relay look-up table

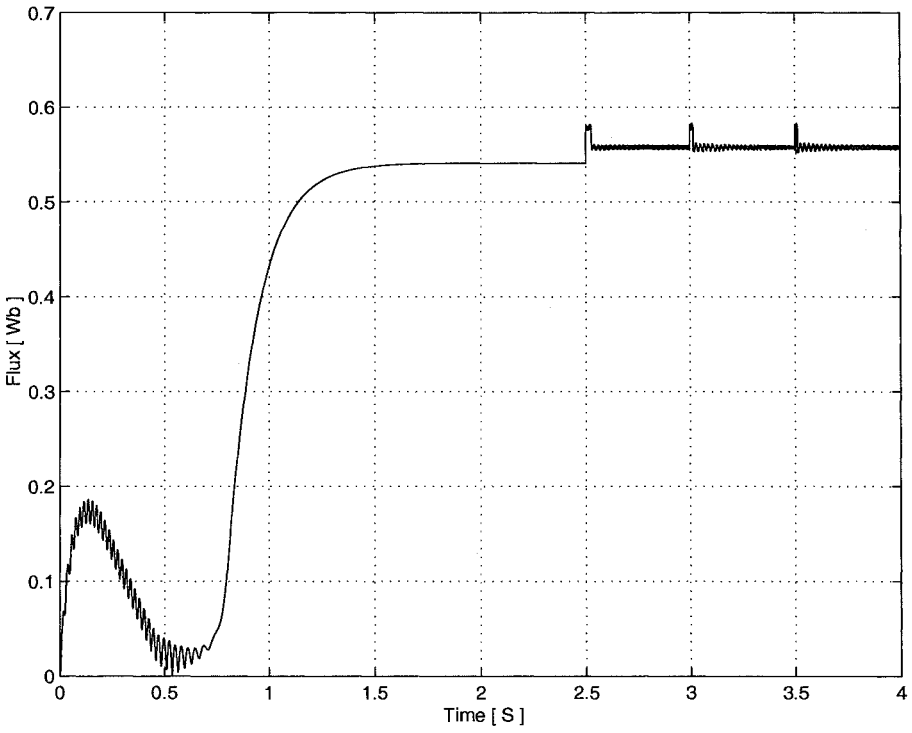

Figure 6.10 Flux plot by using the improved two-level relay

6.3 Combined Control Method

If the active voltage vectors are used only, the switching losses can be significant causing a thermal burden to the heat sink. Also extra attention should be paid to prevent the short-circuit of two switching phases. Since most of the time, the machine would be in steady state operation, it is reasonable to consider a compromised technique. In this alternative switching method, the controller will use zero row instead of '–1' one for the condition of anticlockwise rotating frame($\omega_s > 0$) and substituting the '1' row in clockwise rotating frame (for $\omega_s < 0$) by the zero row. This approach will half the switching frequency in steady state and will also help reduce the acoustic noise as well as the torque, flux, and current pulsations.

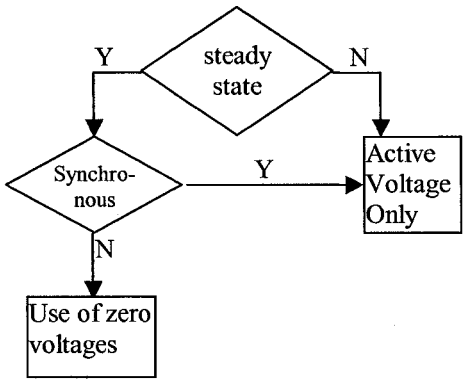

Figure 6.11 The control flow chart

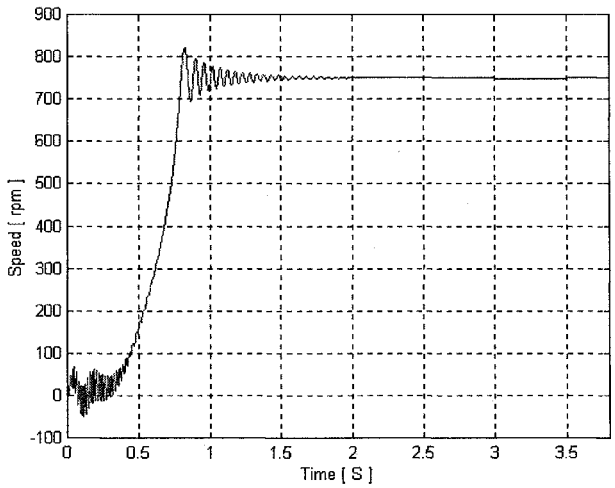

Figure 6.12 The synchronous speed plot of modified DTC

In order to reduce the switching frequency while maintaining the good control dynamics, a speed judgement (a programmed function) has been implemented to decide whether to use an active or zero voltage vector depending on the operating conditions of the machine (steady state or transient) as indicated in Figure 6.11. The improved dynamic performance achieved in this way can be seen in Figure 6.12 where after reaching the synchronous speed, the unloaded machine is first instantly loaded at 5 Nm (at 3 s) and then suddenly unloaded at 3.5 s. It is immediately obvious

from the same figure that, due to the quicker transient response, the speed variation is considerably reduced (it is virtually negligible) compared to that in Figure 6.6. It should be mentioned that the results in Figs.6. 9-6.12 have been generated by executing the DTC algorithm in torque mode (i.e. without speed feedback).

The previous discussions have clearly shown that there are close similarities in the DTC principles between the BDFRM and the induction machine. For example, the same switching table (Table 4.1) and associated conditional relationships (4.11) and (6.12) are also applicable to the cage induction machines. It is interesting that this link can be established despite the fundamentally different torque producing mechanism. However, one of the principal distinctions between the two machines is that the BDFRM can regenerate power through the secondary winding at sub-synchronous speeds while still operating as a motor[3], as follows from (4.7) for ω_s<0. Note that unlike the induction machine, the BDFRM speed and torque in this case are of the same sign (both positive or negative) but the $d_s q_s$ frame rotates in the opposite direction to the primary $d_p q_p$ frame due to the reversed phase sequence of the secondary winding to the primary one in this speed region as mentioned earlier.

[3] This mode is analogous to dynamic breaking in induction machines but, unlike the latter, the BDFRM operation can be sustained.

6.4 Conclusions

It has been shown in the chapter that some modifications to the traditional switching strategy [2,4] for the IM's are necessary before it can be applied to the BDFRM, especially at lower secondary frequencies which is the potential working condition for the BDFRM target applications (such as wind turbines, large pumps or similar drives). Different alternative methods based on an analytical technique (and not the secondary voltage integration) for estimating the secondary flux (more details can be found in Section 7.2.3, Chapter 7.) are suggested and mutually compared. A modified switching look-up table is developed to improve the machine performance in the low frequency range. It allows stable machine operation at either speed and under all loading conditions of interest down to zero frequency this being impossible to achieve with cage induction machines. The proposed switching technique is also applicable to DEWRIM's due to modelling similarities of the two machines.

The algorithm accuracy has been tested using the maximum torque per inverter ampere strategy as an example. The preliminary simulation studies have demonstrated its effectiveness over the whole operating speed range and under all loading conditions this certainly being an encouraging and necessary initial step for its practical implementation.

The following main conclusions/observations can be made from the generated results:

- The developed DTC system is potentially applicable down to zero supply frequency unlike a cage induction or any other machine with DTC.
- The BDFRM is virtually fully fluxed even when unloaded and can achieve fast transient response to load torque changes in this respect.
- With a torque dependent flux reference (detailed in Chapter 7), it is possible to optimise steady-state operation of the machine by executing the control in a stationary frame in contrast to conventional field-oriented controllers.
- There is no apparent trade-off between the optimum dynamic and steady state performance of the BDFRM with the proposed DTC. This is an important advantage over a cage induction machine.
- The use of active voltage vectors only allows generally better performance, the simpler structure and easier digital implementation of the DTC scheme as opposed to using zero vectors as well. This is particularly the case if the machine is operated near or at the synchronous speed.

Chapter 7 Simulation Studies of DTC on BDFRM

A comprehensive simulation analysis is a useful testing tool of the theoretical performance and potential applicability of the developed DTC algorithm. This is foremost the case in DSP implementations using dSPACE® systems which are fully compatible with Matlab®/Simulink® environment and in fact use the respective simulation programmes as a starting point while compiling the real time codes.

It is mainly the increased portability and ease of practical realisation that have contributed to selecting the conventional Matlab®/Simulink® software for the controller development. The control programme has been mainly based on the functional blocks readily available from the Simulink® library. The principal reason for adopting this approach is its user-friendliness when it comes to the dSPACE® implementation.

In this chapter, the ideal machine model that ignores the effects of magnetic saturation and core losses is used for the controller design. The justification for using this approximation has been found in the fact that the machine is virtually fully fluxed under all operating conditions (due to the primary winding grid connection) and therefore the inductance variations caused by magnetic saturation are reduced to a

minimum. On the other hand, accounting for iron losses in the machine model is extremely difficult for this particular machine owing to its highly unusual and complicated operating principle. The experimental results presented in the later chapters (Chapter 8) will however show that core losses can be significant (especially if the machine is not optimally designed this being the case with the BDFRM test prototype used for this research) and therefore deserve a particular attention. In the following sections, each functional block the developed controller is built upon will be described in detail.

The simulation can run in both 'sensor' and 'sensor-less' modes. For the sensor operation, the control programme uses the shaft position feedback available from the machine model to generate the speed estimates (in reality, this information would be obtained by a shaft position sensor). In the sensor-less mode, an estimator is designed to get the rotor speed values from the voltage and/or current measurements. A number of plots for different machine parameters have been presented to illustrate that the DTC can be successfully applied to the BDFRM over the entire speed range and under all loading conditions of interest.

7.1 Program Overview

A functional block diagram of the algorithmic structure of the DTC controlled BDFRM drive is shown as Figure 7.1. It can be noticed that the controller has the

flexibility to achieve either sensor or sensor-less operation depending on the status of the switch selector. The diagram essentially consists of two parts, one for the model of the machine and the other representing the control system. The machine modelling aspects have been thoroughly reviewed in Chapter 3 and won't be repeated here. As mentioned in the introduction, a linear machine model has been employed with the saturation and iron losses being ignored for convenience of analysis and to facilitate the control development.

In terms of the control configuration, the central part of the controller is the look-up table of inverter switching. As can be seen from Chapter 4 and Chapter 6, the look-up table is a two-input system: it is controlled by the outputs of the torque and flux hysteresis comparators. A PI controller will convert the desired speed value selected by the user into a certain torque reference to be fed into the torque controller. The reference flux can be torque independent or can be related to reference torque (as described in the following) so that a particular machine performance parameter is optimised (in this thesis, the maximum torque per inverter ampere control property has served as a case study). In the following sections, a simplified two-level look-up table from Chapter 6 will be used.

To estimate the secondary current vector orientation in a stationary reference frame, measured signals of the secondary currents are fed into the 'current calculation' block. The latter only needs samples of the two line currents, as in most cases the

Y-connected windings (both primary and secondary) are with an isolated neutral point:

$$\begin{aligned} &i_a + i_b + i_c = 0 \Rightarrow \\ &i_c = -i_a - i_b \end{aligned} \tag{7.1}$$

The output of the 'Current Block' will be used in the calculation of the secondary flux magnitude and angle (as described in the previous chapter and also in the following sections). Furthermore, the same output will be fed in the 'Rotor Position Estimator' if the sensor-less control is desired. The information of the 'Flux Estimator' will be compared with the reference value in the flux comparator so that a particular error signal, relevant for determining an appropriate inverter switching pattern, is generated.

Unlike the secondary flux estimation technique discussed above, the feed-in values to calculate the machine electromagnetic torque come from the primary side since the primary winding is directly connected to the supply grid of fixed voltage and frequency. As such, these signals are nearly unaffected by the inverter switching ripples present in the secondary waveforms, and especially in the BDFRM having inherently modest magnetic coupling between the two windings. For the primary flux and torque estimation, the primary voltage and current measurements are required. The current vector calculation method outlined above can be applied to obtain magnitudes and stationary frame angles of the respective primary voltage and current

vectors. The reason for this is quite clear when it comes to the primary current vector as the primary winding, similarly to the secondary, is commonly designed with an isolated neutral point so that (7.1) holds. The primary voltage supply system, on the other hand, is assumed to be balanced (which is normally the case) resulting in (7.1) being applicable in this case as well. By doing this, the number of voltage and current transducers required is minimised.

Note that for the simulation studies the machine rotating frame model differential equations have been used to represent the machine dynamic behaviour. It is well known that this model is much simpler and more convenient for numerical analysis than the stationary frame one [17,34]. However, since the values available from the model are in rotating reference frames, conventional Park's transformations are necessary to convert the rotating frame quantities into their stationary frame counterparts used by the DTC.

Based on the secondary flux and torque comparator outputs, digital signals will be generated from the switching table to control the inverter legs. The appropriate inverter-switching pattern will then determine the voltage vector to be applied to the machine secondary terminals. The functionality of the control blocks in Figure 7.1 will now be described in detail. The order of this explanation will be dictated by the flow of the control signals.

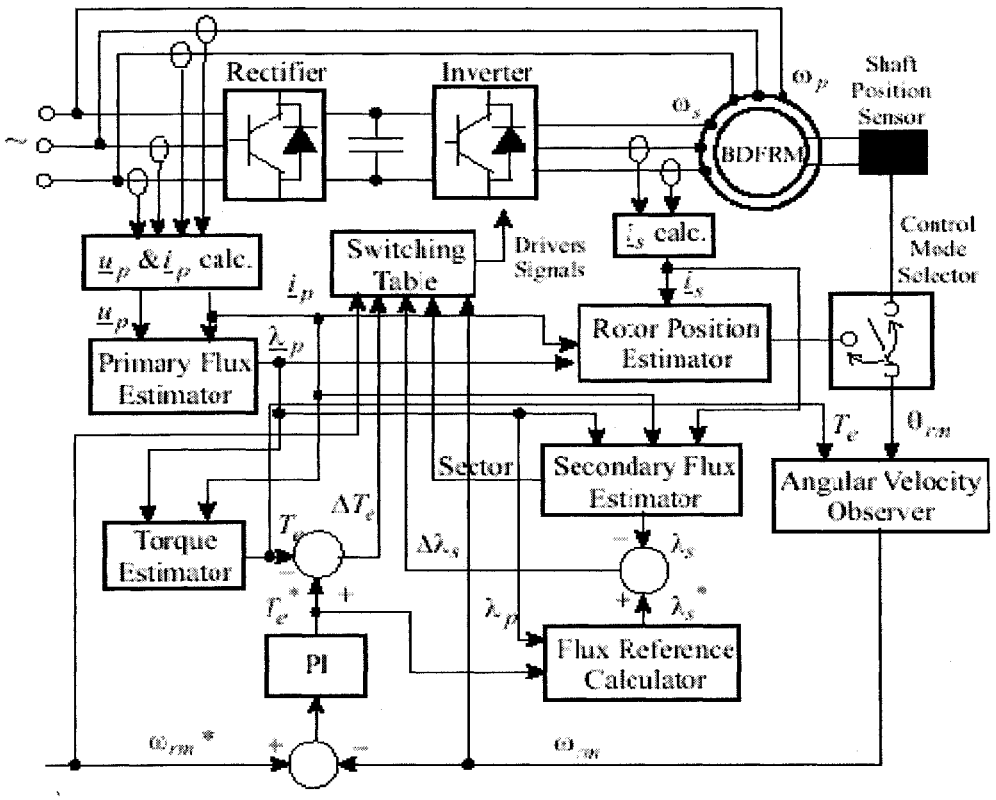

Figure 7.1 DTC algorithm for the BDFRM

7.2 *Functional Blocks*

7.2.1 TRANSFORMATION BLOCK

As previously mentioned, the d-q dynamic model of the machine in a synchronously rotating reference frame is used in the simulation studies. In order to make the controller design practically applicable and therefore usable by the dSPACE® real-time compilers with no or little modifications, the Park's transformation is required to obtain the stationary frame equivalents of the rotating frame quantities available by numerically solving the model equations. For a machine without neutral

connection (i.e. with no zero sequence currents) the relevant parameters are related as follows:

$$\begin{bmatrix} f_d \\ f_q \end{bmatrix} = \frac{2}{3}\begin{bmatrix} \cos\theta_{ave} & \cos(\theta_{ave}-2\pi/3) & \cos(\theta_{ave}+2\pi/3) \\ -\sin\theta_{ave} & -\sin(\theta_{ave}-2\pi/3) & -\sin(\theta_{ave}+2\pi/3) \end{bmatrix}\begin{bmatrix} f_a \\ f_b \\ f_c \end{bmatrix} \tag{7.2}$$

where 'f ' indicates a particular variable such as voltage or current.

Substituting (7.1), (7.2) can be rearranged as:

$$\begin{bmatrix} f_d \\ f_q \end{bmatrix} = \begin{bmatrix} \cos\theta_{ave} & \sin\theta_{ave} \\ -\sin\theta_{ave} & \cos\theta_{ave} \end{bmatrix}\begin{bmatrix} f_a \\ (f_a+2f_b)/\sqrt{3} \end{bmatrix} \tag{7.3}$$

where θ_{ave} is the mean value of the rotating frame angles at the beginning and the end of a particular control interval which are passed into the calculator from the model simulator. If the machine is sensor-less controlled, this angle will be predicted by an angular-velocity observer[4,97]. It should be noted here that the averaging is becoming less important for the DTC considering its extremely high control update rates (the sampling rate of the controller is of the order of 10 kHz and higher). In other words, in this case there is virtually no difference between the discrete form and instantaneous time domain equations.

As mentioned in Chapter 4, the stator fluxes are travelling at primary and secondary winding angular velocities respectively. Therefore there are two reference frames in

the air gap rotating at different speeds. If anti-clockwise direction is set as the positive (reference) direction, the transformation of stationary to rotating frame will be:

$$Q_r = Q_s * e^{-j\omega t} = (Q_{sd} + jQ_{sq})(\cos(\omega t) + j\sin(-\omega t)) \quad (7.4)$$

where 'Q' indicates a particular quantity in question (such as voltage, current, flux etc.), and the subscripts 'r' and 's' signify the rotating and secondary frame components respectively whereas 'ω' represents the speed of the rotating frame of interest (i.e. primary or secondary in this case) as illustrated in Fig. 7.2.

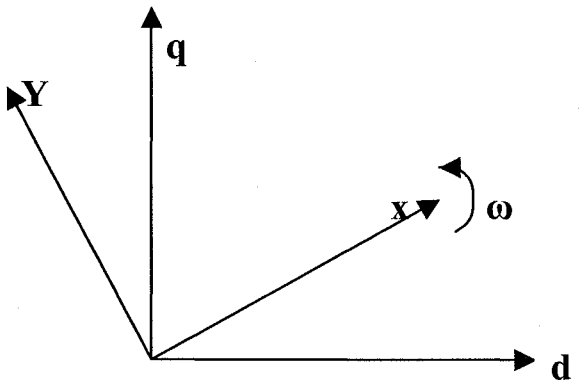

Figure 7.2: The frame tranformation.

If the inverse conversion is needed (i.e. from a stationary to rotating frame) then the relevant expression will be:

$$f_s = f_r * e^{j\omega t} = (f_{sd} + jf_{sq})(\cos(\omega t) + j\sin(\omega t)) \quad (7.5)$$

Of course the same expression can be used if the quantity is changing from one rotating frame to the other. In that case, the 'ω' will be the relative speed between the two frames.

7.2.2 SPEED PI CONTROLLER

The reference value of torque is passed from a conventional speed PI controller so that the closed loop control algorithm will be formed. A block diagram in continuous time domain is shown in Figure 7.3.

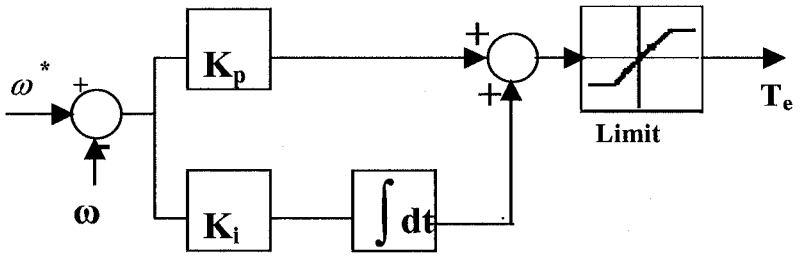

Figure 7.3: Block diagram of speed PI controller

There is a torque limiter before the reference torque is fed to the torque controller so that the machine is protected in case that torque values outside the allowable range are asked for by the speed regulator. In addition to the torque limiting, the 'anti-windup' function is also implemented in the speed controller to disable the integrator action when saturation occurs.

7.2.3 FLUX REFERENCE

The reference value of flux can be set independently. In simulation, the flux reference was linked with reference torque value, as (7.6), to optimise the machine performance for a given torque. For example, if the maximum torque per inverter ampere strategy (MTPIA) is of concern, then one needs to minimise the inverter current loading for a given torque output. It can be shown that this control objective is achieved if the torque dependence of the secondary flux magnitude is of the form [8,60,72]:

$$\lambda^*_s = \sqrt{(\frac{L_{ps}}{L_p}\lambda_p)^2 + [L_{ps}(1/K^2_{ps} - 1)\frac{2T_{eref}}{3p_r\lambda_p}]^2} \tag{7.6}$$

where:

$$K_{ps} = \sqrt{L^2_{ps}/(L_p * L_S)} \tag{7.7}$$

One can see from (7.6) that there is a load independent offset in λ_s^* (as $\lambda_{ps} \approx$ const.) due to the primary winding grid connection. The variable torque term is only a small portion of the entire λ_s^* magnitude meaning that the majority of the secondary flux comes from the primary side through mutual coupling. In other words, the machine is virtually fully fluxed even if unloaded which means that in this sense it can respond quickly to the load torque changes. Another important implication of the $\lambda_{sd} = \lambda_{ps} \approx$ const. (in the secondary $d_s q_s$ frame of Figure 7.2) condition is that the DTC can be optimised since in this case vector control essentially becomes scalar control where a λ_{sq} component is controlled indirectly via λ_s in the stationary frame. The previous two properties represent the significant advantages of the BDFRM over a cage induction machine.

7.2.4 FLUX ESTIMATION

The secondary flux vector magnitude and angle in a stator frame aligned with the phase-a axis of the winding[4] (i.e. $U_1 = 100$ vector position in Figure 4.3) can be estimated in a traditional manner by integrating the secondary voltage as described in Chapter 4. As for any other machine, this approach allows satisfactory estimates when the secondary frequency (and therefore $\omega_s \lambda_s$) is high enough so that $u_s >> R_s i_s$. However, in a narrow range around the synchronous speed ($\omega_{syn} = \omega_p / p_r$), which is a typical operating region of the BDFRM, the ω_s values are small and the DTC algorithm may experience the same low speed voltage integration problems and flux estimation inaccuracies of conventional machines. Fortunately, by virtue of the BDFRM double feeding, both machine sides are externally approachable and it is possible to eliminate this well-known DTC deficiency by estimating λ_s from measurements of the grid voltages and winding currents at line frequency.

The secondary and primary flux expressions in a stationary frame [30] were discussed in Chapter 5, which are reproduced here for convenience:

$$\begin{aligned} \lambda_{ps} &= L_p i_{ps} + L_{ps} i_{ss}^* e^{j\theta r} \\ \lambda_{ss} &= L_s i_{ss} + L_{ps} i_{ps}^* e^{j\theta r} \end{aligned} \tag{7.8}$$

where λ_{ps} is primary flux in stationary frame; λ_{ss} is secondary flux in stationary frame; L_p is primary inductance and L_s is secondary inductance; L_{ps} is mutual inductance; i_{ps} is the primary current in stationary frame; i_{ss} is secondary current in stationary frame; θ_r is mechanical rotor

[4] The primary and secondary windings are normally accommodated in the same slots and there is no space displacement between them.

position with regarding to stationary d axis.

By eliminating the rotor position dependent exponential terms $e^{j\theta r}$ the secondary flux vector can be written in terms of the primary flux and windings currents as follows:

$$\lambda_{ss} = L_s i_{ss} + L_{ps} i^*_{ps} \frac{\lambda_{ps} - L_p i_{ps}}{L_{ps} i^*_{ss}} \tag{7.9}$$

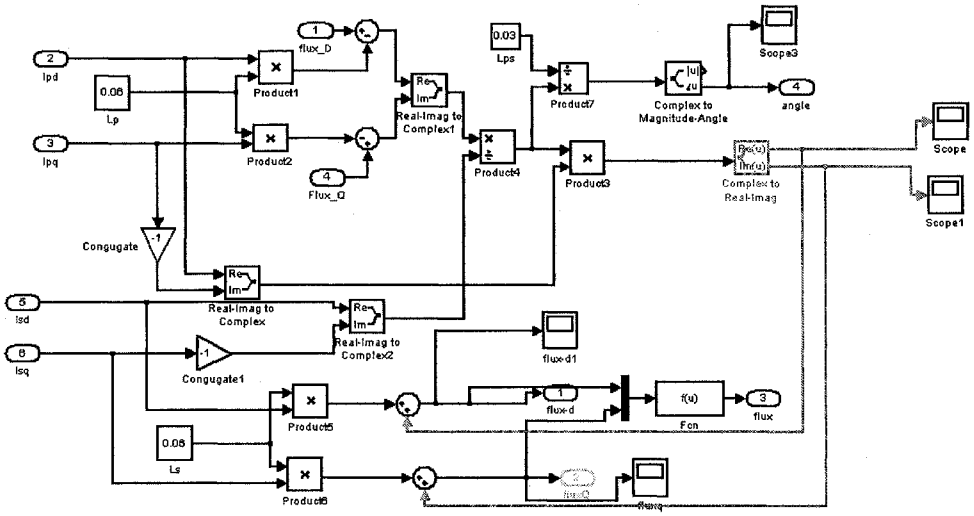

Figure 7.4: The calculation of the secondary flux

The real (d-axis component) and imaginary (q-axis component) parts of the previous equation will be:

$$\lambda_{sd} = L_s i_{sd} + \mathrm{Re}\,l(L_{ps} i^*_{ps} \frac{\lambda_{ps} - L_p i_{ps}}{L_{ps} i^*_{ss}}) \tag{7.10}$$

$$\lambda_{sq} = L_s i_{sq} + \mathrm{Im}\,g(L_{ps} i^*_{ps} \frac{\lambda_{ps} - L_p i_{ps}}{L_{ps} i^*_{ss}}) \tag{7.11}$$

The simulation block to achieve the above calculation is presented in Figure 7.4. This expression is clearly more parameter dependent than (4.8) in Chapter 4 but allows more accurate estimates, better control and stable machine operation over the entire speed range (when the secondary supply frequencies are limited) and under all loading conditions of the machine. Surely, in applications where the secondary frequencies are reasonable one can switch to the traditional voltage integration approach which is fewer parameter dependent.

7.2.5 TORQUE ESTIMATOR

As mentioned previously, there is a number of equivalent torque expressions for the BDFRM but not all of them are suitable for DTC implementation. In practice, the secondary machine side will be more susceptible to various disturbances (such as switching ripples and measurement noise) associated with the power electronic converter. For higher estimation accuracy, it is therefore an imperative to use the primary quantities having much smoother and cleaner waveforms. In this sense, (4.7) in Chapter 4 can be rearranged into a form:

$$T = \frac{3}{2} p_r \left| \underline{\lambda}_p \times \underline{i}_p \right| = \frac{3}{2} p_r \lambda_p i_p \sin \angle \left(\underline{\lambda}_p, \underline{i}_p \right) = \frac{3}{2} p_r \lambda_p i_{pq} \tag{7.12}$$

where i_{pq} is the q-axis primary current in the primary flux frame.

High estimation accuracy can be expected in practice as (7.12) is machine parameter independent and it is exclusively based on the primary quantities having virtually

ripple-free waveforms. Switching ripples are present on the secondary waveforms but are generally of very low magnitude if a partly rated inverter is used. They are basically non-existent on the primary side and because of the relatively weak magnetic coupling between the windings that is inherent with this machine. The primary flux magnitude and angle and then i_{pq} can be easily calculated from the primary voltage and current measurements. In the latter case the relevant expression is (Figure. 7.5):

$$i_{pq} = i_p \sin(\alpha - \beta) \tag{7.13}$$

In most cases, $R_p i_p$ is negligible (especially with an increasing rating of the machine) which further simplifies the primary flux estimation. Issues related to this will be addressed in the following section.

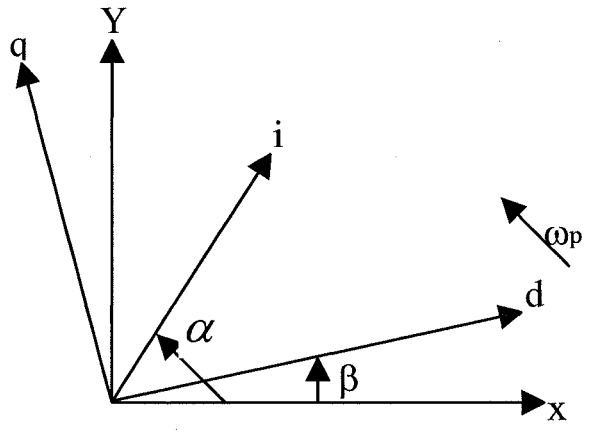

Figure 7.5 The vector diagram of primary current

7.2.6 PRIMARY FLUX CALCULATION

The general voltage equation of a machine using conventional phasor notation is:

$$\mathbf{u} = R\mathbf{i} + \mathbf{e} = R\mathbf{i} + \frac{d\boldsymbol{\lambda}}{dt} \tag{7.14}$$

where e is the induced voltage. The same expression is used for the primary flux estimation of the BDFRM.

The value of stator resistance R is often measured by a simple dc test bearing in mind that at 50 Hz the influence of skin effect is negligible so that the DC and AC values of the resistance are nearly identical. Although in most cases an accurate knowledge of primary winding resistance is not required due to the dominant back-emf of line frequency as mentioned above, this is not quite true if one wants to implement the MTPIA control strategy. The sensitivity of the secondary flux expression has been discussed in Chapter 5.

Assuming no neutral connection, the $d_p q_p$ currents of the machine can be determined from the measured instantaneous values of either two of the three-phase currents (e.g. $\mathbf{i}_a$ *and* $\mathbf{i}_b$) using (7.3):

$$\mathbf{i}_p = \mathbf{i}_{pd} + \mathbf{i}_{pq} = i_a + j\frac{i_a + 2i_b}{\sqrt{3}} \tag{7.15}$$

Once u and i are identified, then the d-q components of the induced voltage phasor e is immediately known. Consequently, the primary flux is the integrated value of this induced voltage.

7.2.7 LOOK-UP TABLE FOR EACH PHASE

The control of the 3-phase voltage source inverter bridge is achieved by a look-up table. Since there are three inverter legs, each with two power devices of opposite switching status, there will be 3 look-up tables i.e. one per leg. The commands for the two IGBTs in the same leg have the logic relationship as 'NOT'. For example, when the device 1 is open the device 2 will be closed, and vice-versa. When it comes to the simulation, the actual input value will be for each phase. The three look-up tables which control the inverter bridge will be developed from the voltage vector look-up table (Tab.4.1 of Chapter 4). To achieve simplified two-level comparator verified in Chapter 6, two columns corresponding to dT=0 will be eliminated.

The look-up table is divided into 3 individual look-up tables, one for each of the inverter legs. In the simulation file, the respective blocks are named as "Table for switch A", "Table for switch B", "Table for switch C", with the Look-Up Table (2-D) block from the Simulink® library being used to represent either of them. A block "Index", which is the 'Fcn' block in the Simulink® 3.0 library, is created to co-ordinate the outputs. The inputs to this block are the outputs of flux comparator (FL) and torque comparator (Te) i.e. the Relay blocks. The "Index" block performs the function: "Index = 5 - 3*FL - Te", so that the following combinations are possible:

FL = 1 and Te = 1, Index = 1

FL = 1 and Te = 0, Index = 2

FL = 1 and Te = -1, Index = 3

FL = 0 and Te = 1, Index = 4

FL = 0 and Te = 0, Index = 5

FL = 0 and Te = -1, Index = 6

In a similar manner, one can associate another set of index values (1 to 6) to a particular sector in a stationary plane containing the secondary flux vector at a certain time instant. The six sectors and associated indices are as follows:

(0<=u(1) && u(1)<pi/6)|| (11*pi/6<u(1) &&u(1)<2*pi), Index=1

(pi/6<=u(1)) && (u(1)<pi/2), Index=2

(pi/2<=u(1)) && (u(1)<pi*5/6), Index=3

(pi*5/6<=u(1)) && (u(1)<=7*pi/6), Index=4

(pi*7/6<=u(1)) && (u(1)<3*pi/2), Index=5

(3*pi/2<=u(1)) && (u(1)<11*pi/6), Index=6

The 'x' direction of a 2-dimension look-up table for each leg is determined by the output of function "Index = 5 - 3*FL - Te", while the y direction is corresponding to a sector the stator flux vector is located in. Hence the look-up table for each particular leg corresponding to the 3-phases will be:

1. **for leg (phase) A**

y

	1	2	3	4	5	6
1	1	0	0	0	1	1
2	1	0	1	0	1	0
3	1	1	1	0	0	0
4	0	0	0	1	1	1
5	0	1	0	1	0	1
6	0	1	1	1	0	0

x

2. **for leg (phase) B**

y

	1	2	3	4	5	6
1	1	1	1	0	0	0
2	1	0	1	0	1	0
3	0	0	1	1	1	0
4	1	1	0	0	0	1
5	0	1	0	1	0	1
6	0	0	0	1	1	1

x

3. **for leg (phase) C**

y

	1	2	3	4	5	6
1	0	0	1	1	1	0
2	1	0	1	0	1	0
3	1	0	0	0	1	1
4	0	1	1	1	0	0
5	0	1	0	1	0	1
6	1	1	0	0	0	1

x

For example: if $d\lambda = 1$, $dt = 1$ then the comparator function will have the output = 5 - 3*FL – Te = 1, which means that the first column of a particular switching table defined above would be of interest. If the stator flux is in sector one (-pi/6<=u(1) && u(1)<pi/6), then the y input will also be 1 resulting in the voltage vector of 110 being applied to the secondary terminals, that is : 1 for leg A, 1 for leg B and 0 for leg C.

The above model is obviously very similar to the optimal look-up table for an induction drive.

7.2.8 THE SECONDARY CURRENT ALIGNMENT

The MTPSA control strategy is very important as it allows the inverter loading to be minimised for a given torque output. This control objective is achieved if the secondary current vector is perpendicular to the mutual flux vector (coupling the

secondary winding) when all of the secondary current is torque producing i.e. when the d-axis secondary current is zero in the respective (secondary) rotating reference frame.

In order to evaluate whether the MTPIA conditions are indeed accomplished by the DTC being executed in a stationary reference frame, one needs to estimate the secondary d-axis current in the rotating secondary frame and make sure it is zero as stated above. The purpose of the following paragraphs and the simulation results (Figure 7.6-7.8) presented is to illustrate this principle. The plots have been generated under the following conditions: the BDFRM is started as a conventional wound rotor induction machine with the shorted secondary terminals until 2.5-s when the inverter is connected and the control is enabled; the machine is subsequently loaded at 10 Nm constant torque with the speed reference of 90 rad/s at 2.5-s , 25π at 3-s and 68 rad/s at 3.5-s.

The d-axis secondary current in the respective reference frame rotating at the secondary applied angular frequency is calculated as: $\mathbf{i}_{sd} = \mathbf{i}_s \cos(\alpha_s - \theta)$. A sequence of steps to follow is:

1. determine the secondary current angle in the stationary reference frame;
2. get the position of the mutual flux vector in the stationary reference frame;
3. calculate the relative position between the two vectors;
4. find the d-axis current.

To achieve step 2, there are kinds of ways as well. In the test, two different approaches are used simultaneously to make sure the result is right. One is to get the flux angle in the primary reference frame and then refer this angle into secondary frame; the other method is to get the flux angle in the stationary frame and then use this to derive the corresponding secondary frame angle.

In both cases, the formula for integrating the primary voltage in the stationary reference frame (in **Section 3.3.1**) is used to calculate the d and q component of flux. The equation is quoted as following:

$$\begin{aligned} \mathbf{u}_{pd} &= R_p \mathbf{i}_{pd} + \frac{d\boldsymbol{\lambda}_{pd}}{dt} - \omega \boldsymbol{\lambda}_{pq} \\ \mathbf{u}_{pq} &= R_p \mathbf{i}_{pq} + \frac{d\boldsymbol{\lambda}_{pq}}{dt} + \omega \boldsymbol{\lambda}_{pd} \end{aligned} \tag{7.16}$$

The error between these two calculation methods is zero as expected. The flux angle is constant during the whole process and is very small: only 0.02 rad (Figure 7.6). This result is understandable since the machine model is built on the assumption that the primary voltage is aligned with the primary flux. By setting the primary supply voltage to be entirely along the q-axis (i.e. its d-axis component is zero), the d-axis will nearly align with the primary flux linkage vector. However, this is not exactly the case due to the primary resistance voltage drop resulting in a small angular displacement identified previously. Similarly, Figure 7.6 demonstrates that the secondary current angle in its own rotating frame has a constant value as well.

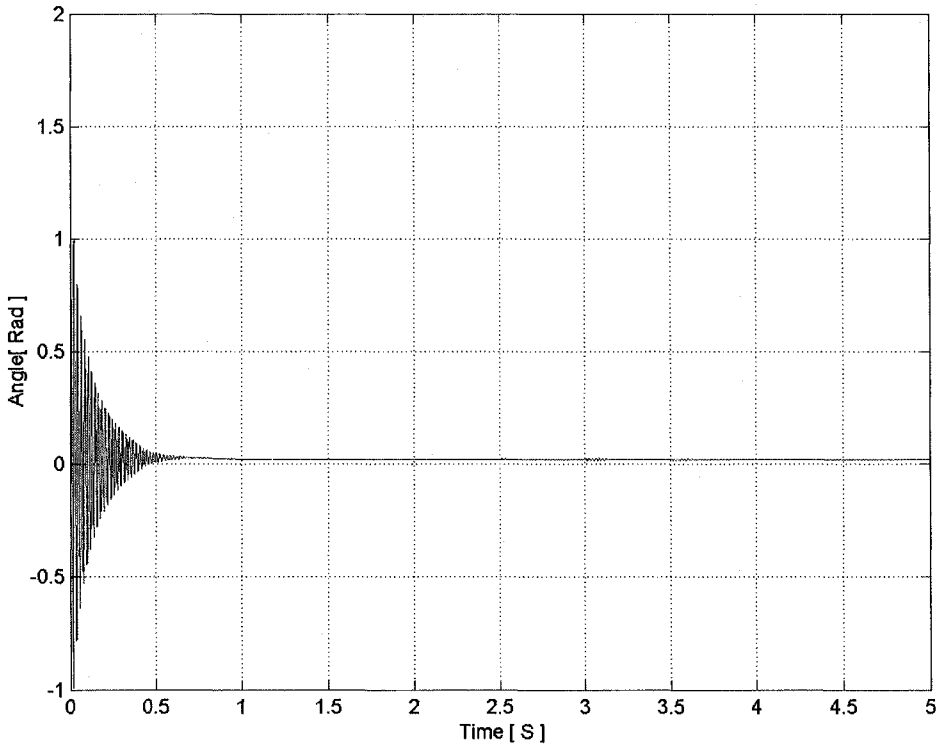

Figure 7.6 The angle of primary flux in its own rotating frame

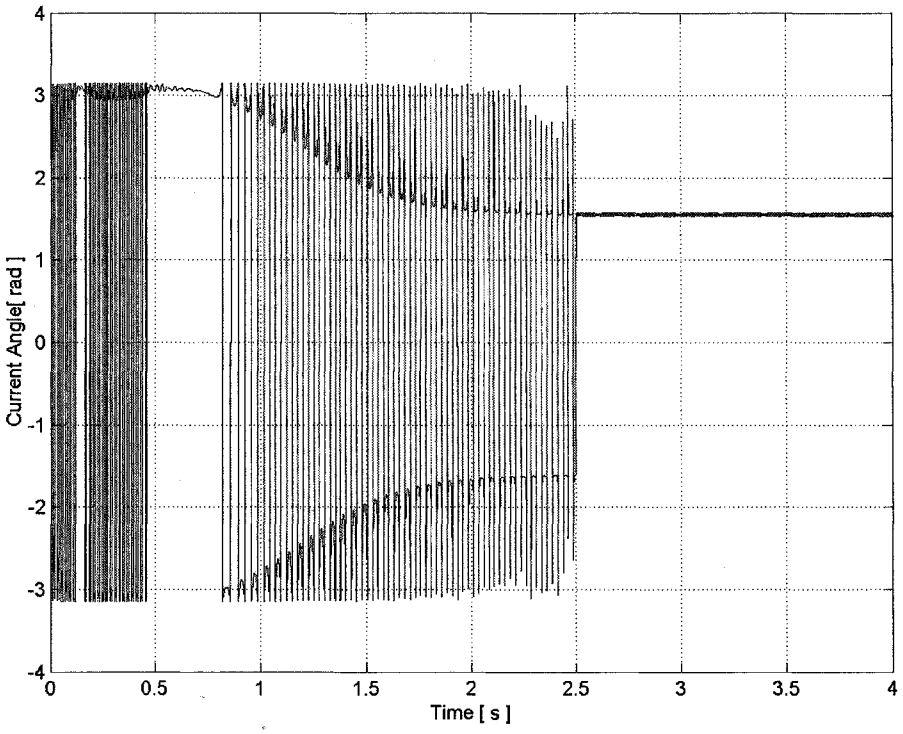

Figure 7.7 The angle of secondary current in its own rotating frame

The plot of the secondary d-axis current will be Figure 7.8:

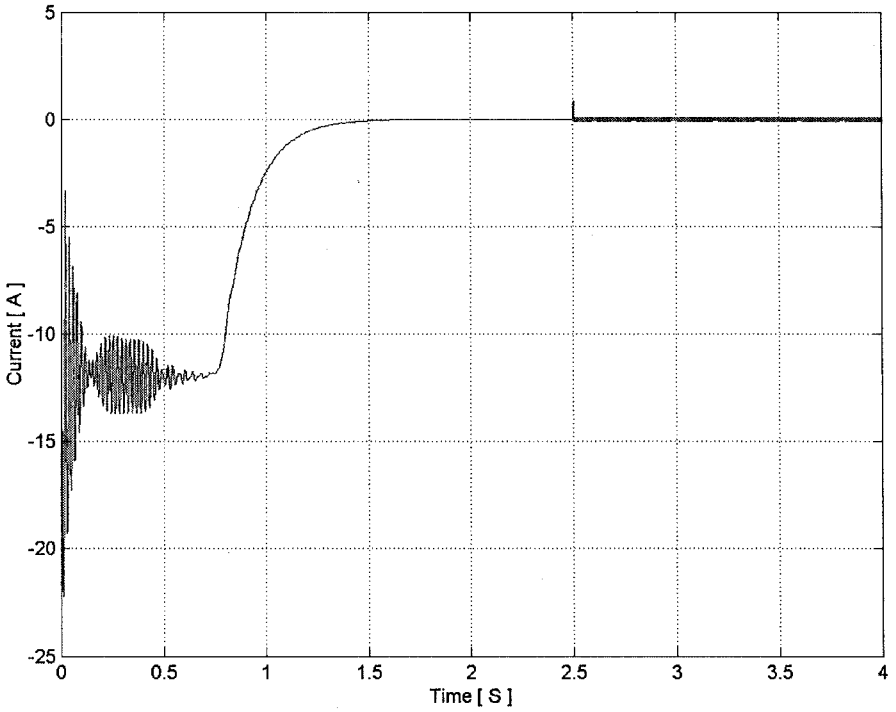

Figure 7.8 The secondary d-axis current

7.3 Fourier Analysis of The Switching Frequency

It can be found that the switching frequency is spread all over the range although there is a rated maximum frequency. This is one of the characteristics of the DTC switching strategy. Unlike the PWM strategy that has a fixed switching frequency, the DTC switching is determined by the machine operating conditions, the selected torque and flux control band-width as well as the voltage vectors applied to the machine (i.e. zero or active) and is therefore variable. The highest switching frequency is dictated by the system sampling time. The plots below correspond to the steady state conditions. Figure 7.9 is the plot for the secondary phase current. Figure 7.10 is the Fourier analysis of the signals. The maximum switching frequency is 6 kHz, which is

defined by the sampling time. The amplitude of the fundamental frequency is $\frac{1}{0.14s} Hz = 7.14$ Hz.

7.3.1 SIMULATION RESULTS

The simulated DTC performances for the maximum torque per secondary ampere strategy are presented in the section. The machine parameters used for the simulation studies can be found in the Appendix A.

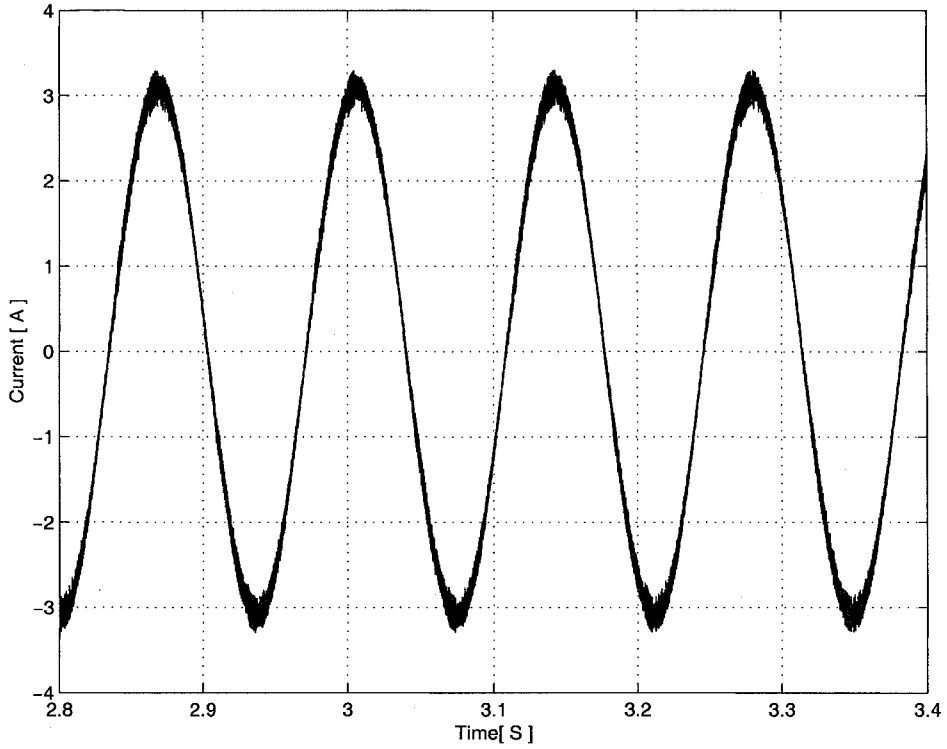

Figure 7.9 The current in phase-a secondary side, steady state

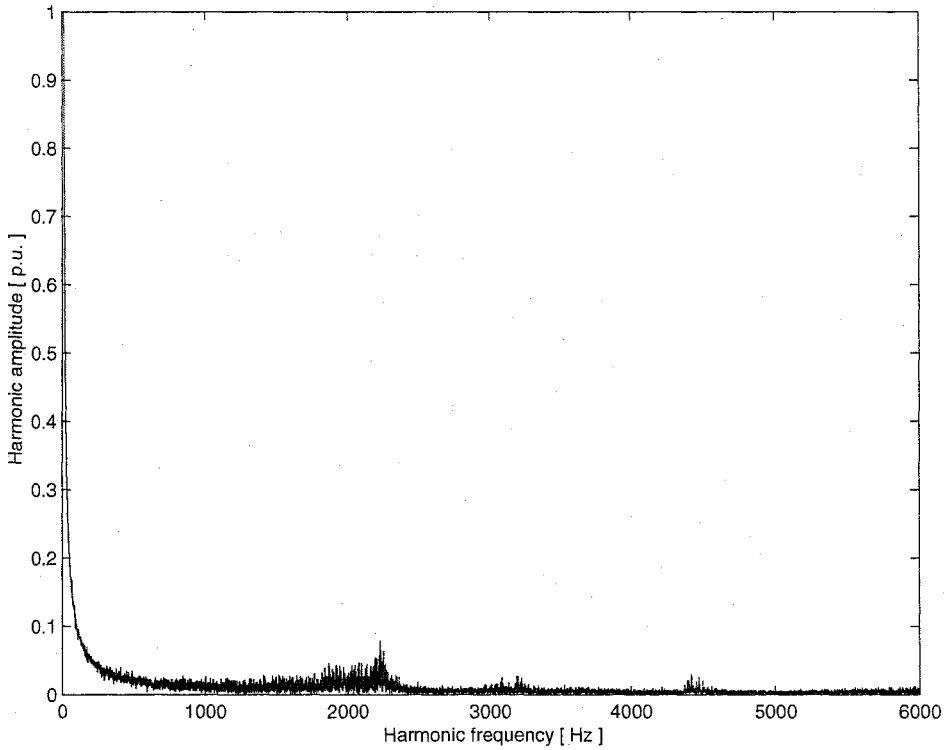

Figure 7.10 Spectrum of the switching frequency

Both the sensor based and sensor-less speed control algorithms were simulated. Therefore, this section is organised in two parts. The first part presents the simulation studies for the machine controlled in the sensor mode, and the second subsection shows the results obtained by executing the sensorless DTC algorithm.

7.4 Sensor Control

This is the most common form of the speed control because of the performance advantages it offers. As the name implies, the rotor position is assumed known (in reality, measurable by a shaft position sensor). In the simulation, the rotor angle is obtained from the Dormand- Prince solution (detailed in Matlab 6.1 Manual) of the

machine model equations. The control rate for the results presented in the remainder of this subsection is 20 kHz(5e-5 s fixed step).

Some simulation results are shown as Figure 7.11, Figure 7.12(a) and (b) the control objective being to track the speed reference under the maximum torque per ampere control strategy. The machine is assumed to be unloaded during start-up. The gains of the speed PI regulators and an angular velocity observer are maintained constant throughout the entire speed range.

The plots are for the case when the machine is fully loaded at 10-Nm after reaching the synchronous speed of 750-rpm. At the same time instant (2.5-s), the control is activated as mentioned earlier in this chapter. As expected, the starting characteristics of the BDFRM (before 2.5-s) closely resemble those of an induction machine since the BDFRM is started with the shorted secondary windings. One can see from Figure7.11 that the machine speed is accurately controlled at the desired values either in super-synchronous (2.5 to 4.5-s), sub-synchronous (4.5 to 6.5-s) or synchronous (6.5 to 8.5-s) modes. It is also notable that the machine transient response to step changes in the speed command is very fast and with no overshoot. This is a consequence of the precise control of both torque and secondary flux as follows from Figures 7.12 and 7.13 (a) and (b). The switching ripples in the waveforms, typical for DTC, are visible from the same figures.

Figure 7.11 (the top plot is the expanded version of bottom one) displays the speed of the machine during speed control. The top figure plots the BDFRM response to a changing speed reference of 110 rpm above and below synchronous speed (750 rpm) respectively. It can be seen that the machine moves from synchronous speed to 860 rpm nearly instantly and with little overshoot.

The top plot in Figure 7.12 is the electromagnetic torque output. The machine torque accurately follows the reference value (bottom plot in the same figure) being produced by the speed PI regulator. The slight overshoot in the torque response can be reduced by optimally tuning the PI gains. Note the switching ripples, typical for DTC, in the actual torque waveform. The hysteresis band was set to 0.05 Nm below and above the reference value. Therefore the torque tolerance is 1% (corresponding to 5 Nm) in this case. The load torque of 10 Nm is used in the simulation as well to test the PI regulator response. It can be seen that the torque overshoot is reasonably good although a higher overshoot (than 5 Nm torque is applied) can be observed. There are some points outside the hysteresis band. As mentioned previously that the control will require huge calculation task, during that very short period, there are some points missed. One solution is to reduce the step size, which will of course increase the accuracy but at the price of slower execution simulation time.

The corresponding control currents in the *dq* axes are shown in Figure 7.13 the close similarity between the torque and *q*-axis current characteristics is evident from Figure

7.12 and Figure 7.13 as expected. This current has a very fast response and as such is essentially responsible for the torque production. In contrast to that, the function of the current component in the high permeance *d*-axis is primarily to establish flux in the machine. It is therefore always kept zero regardless of the torque sign.

As stated in the previous sections, secondary flux value is dominated by primary flux component. The waveform in Figure 7.14 shows the shape of secondary flux is consistent with torque but 5 Nm torque made small change around 0.54 Wb which was determined by primary flux.

7.4.1 SENSORLESS CONTROL

This section presents simulation results that demonstrate the high accuracy of the new observer-based sensorless algorithm implemented in conjunction with the speed vector controller. Apart from diagrams of the same machine performance indicators as presented in the previous section, additional parameters to be plotted including the absolute errors speed estimation. Most of the observations concerning the plots presented in the preceding section can be extended here as well. The control strategy being applied is still maximum torque per secondary ampere.

The results are generated assuming a control frequency of 20 kHz. This sampling rate corresponds to the situation in previous section. Similarly to the sensor control mode,

the gains of the PI speed regulators and position observer in the controller are kept constant over the considered speed range. The observer gains might be decreased as the noisy position estimates from the estimator are used as an input.

Figure 7.15 shows the observed speed of the machine and the corresponding estimation errors. The latter represents the absolute variations from the correct values obtained by solving the model equations. It can be seen that the speed characteristic is very smooth and it follows the desired trajectory. The fast speed change is nearly linear. The very good observer performance and high accuracy of speed estimates are clearly demonstrated in the bottom plot. The maximum error in transient is only about 2 rad/s.

The electromagnetic torque developed by the machine while changing the speed above and below synchronous speed is plotted in Figure 7.16. The torque curve is obviously quite similar to that in Figure 7.12 (sensor mode). Therefore the observations related to Figure 7.12 essentially apply here as well. The actual torque accurately tracks the reference value. Nevertheless, the performance is slightly deteriorated compared to that in Figure 7.12, this is expected since the control is sensorless and as such more susceptible to errors. one can notice that there is a bit more overshoot at the speed change instants than before.

Figure 7.17 plots the *dq* currents required for the machine to produce the torque presented in the previous figure. The most important point to note is the very good agreement between the q-axis component and the torque since the torque is proportional to the $\mathbf{i}_{sq}$. It is good to observe the mean value of $\mathbf{i}_{sd}$ that is zero.

The effectiveness and high accuracy of the sensorless control simulator demonstrated previously is confirmed by the results in Figure 7.15 (b). This figure illustrates the position estimator performance and observer filtering abilities. The figure is a plot of absolute error.

The final point of the note in this subsection is how the observer gains should be tuned for the convergence and high accuracy of the sensorless algorithm. The tuning is undoubtedly a key factor in the high performance of the controller. The approach used was essentially heuristic. The performance of the observer is sensitive to the gain values and these have to be carefully adjusted depending on the desired application.

As already mentioned, the best performance is achieved with gain scheduling. The gains are changed depending on the machine operating condition (the load torque) and also the speed reached. The philosophy for determining the gains was to increase the gains in more accurate and decrease them when the input estimates are of poor quality. The reason is obviously to track the good estimates and reject the erroneous one.

7.5 Conclusions

Based on the theory stated in the previous chapter, a comprehensive set of computer simulation studies have been carried out to evaluate the performance of a Direct Torque Control controller for the BDFRM. The simulation program and its main functions were explained in detail. Maximum torque per ampere control for the BDFRM prototype, whose properties were determined in Chapter 4, has been implemented by the controller. The control was based on using a machine matrix d-q model.

A nice feature of the control simulator is its ability to run in both the sensor and sensorless control modes. Switching from one mode to another requires little modification of the software, this resulting from the use of an observer algorithm for predicting the rotor position and angular velocity from the current position measurements or estimates.

Plots of the performance during speed reversal of a BDFRM machine controlled in either of the two control modes were shown and discussed. In order to emulate the real system, the control frequency and current sampling rate were set to be exactly the same as in the real-time controller. The significant conclusion/observation that can be drawn from the results are as follows:

- the controller has achieved fast speed control in either mode. The observer estimates when executing the sensorless algorithm are accurate to approximately 2 rad/s.

- the machine electromagnetic torque and flux accurately track the desired trajectories. Small variations under transient conditions were found to be due to rotational voltage induced inaccuracies in predicting the next control.

- The observer tuning is crucial for good performance of the sensorless controller. The accuracy of the algorithm is very sensitive to the gains values and these have to be carefully adjusted. The highest accuracy was obtained with gain scheduling. The basic principle used was to lower the gains when the machine speeds up and increase them at steady speed. The tuning at low speed is different in real time due to practical effects.

From the plots, it can be concluded that the optimum look-up table has been successfully applied and the DTC controller is very effective and has high accuracy in either sensor or sensorless control mode. This argues well for a real-time implementation of the controller.

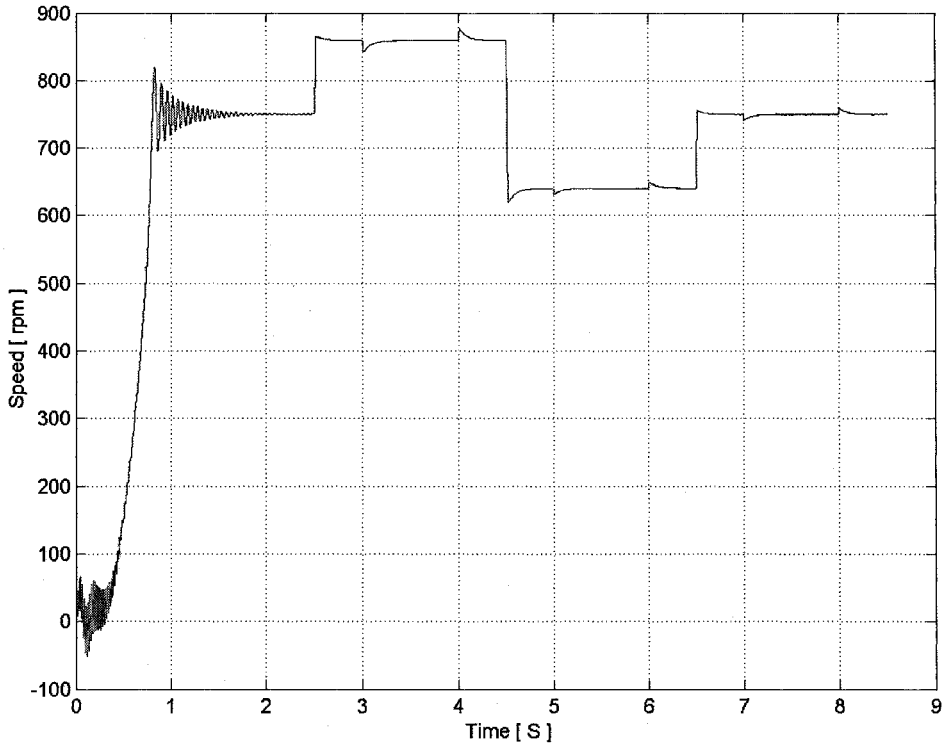

(a) Complete speed response plot

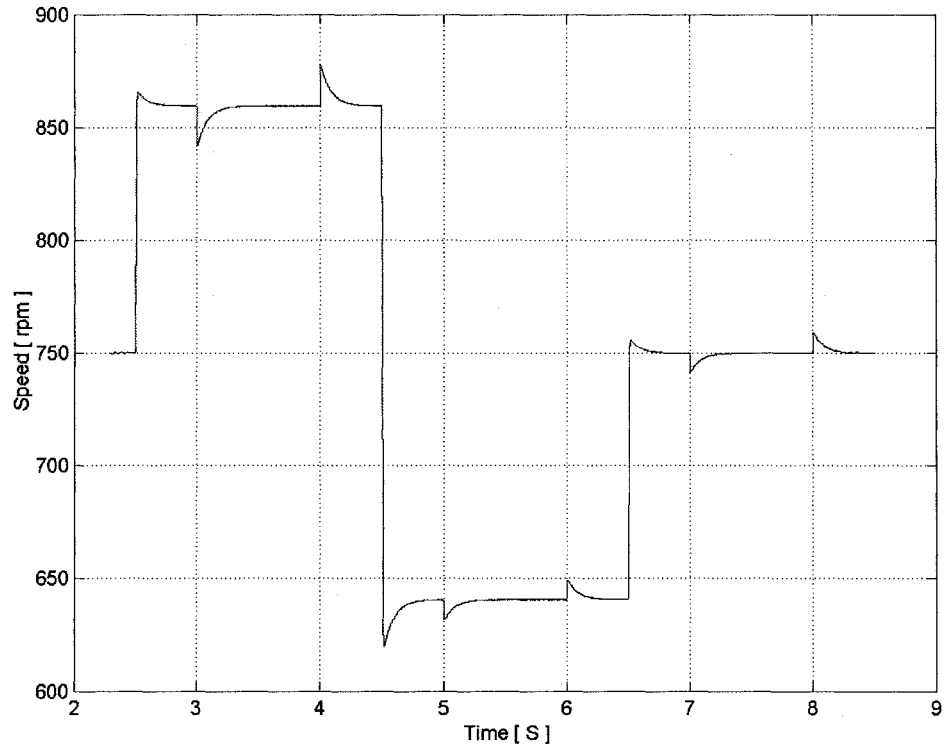

(b) Zoom-in plot of the speed control

Figure 7.11 Speed response in sensor control mode

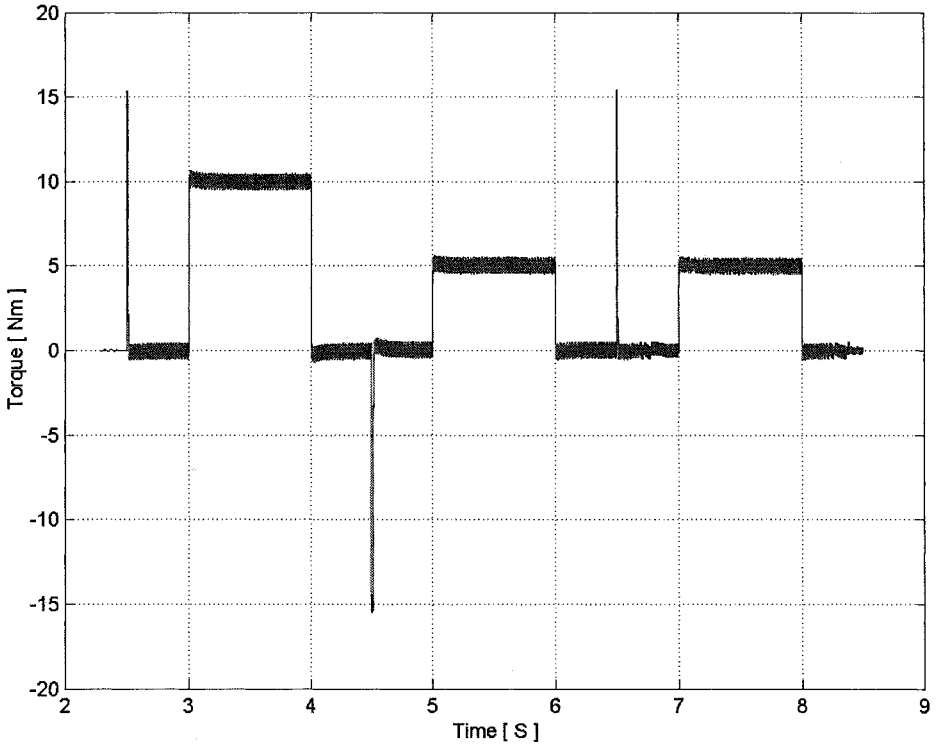

Figure 7.12(a) Electromagnetic torque in sensor control mode

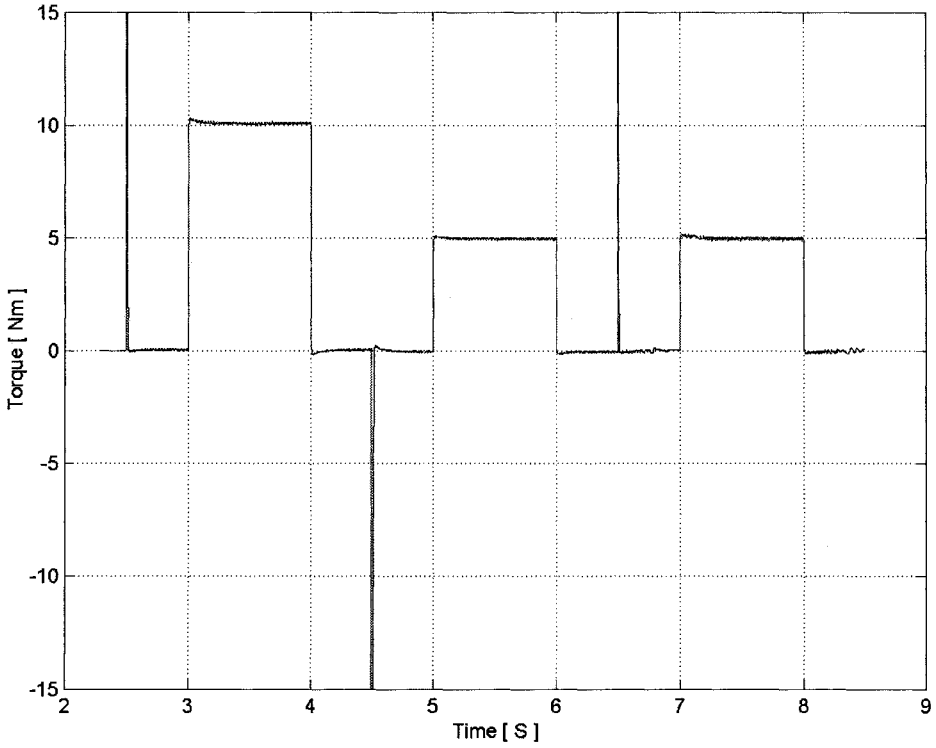

Figure 7.12(b) Torque reference generated in sensor control mode

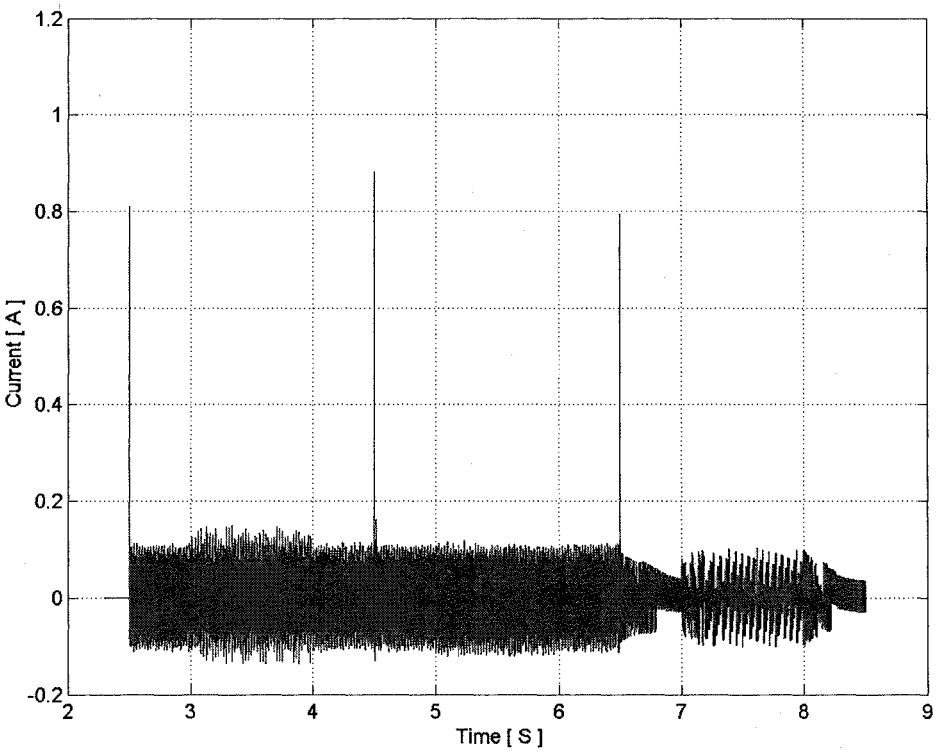

Figure 7.13(a) d-axis Secondary current component in sensor control mode

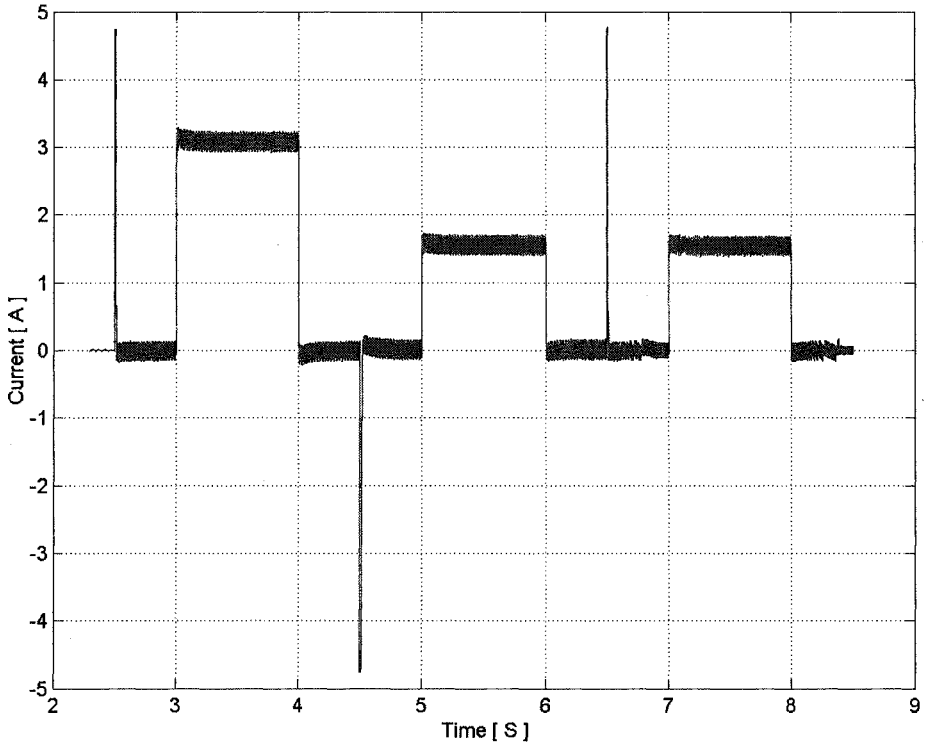

Figure 7.13(b) q-axis Secondary current component in sensor control mode

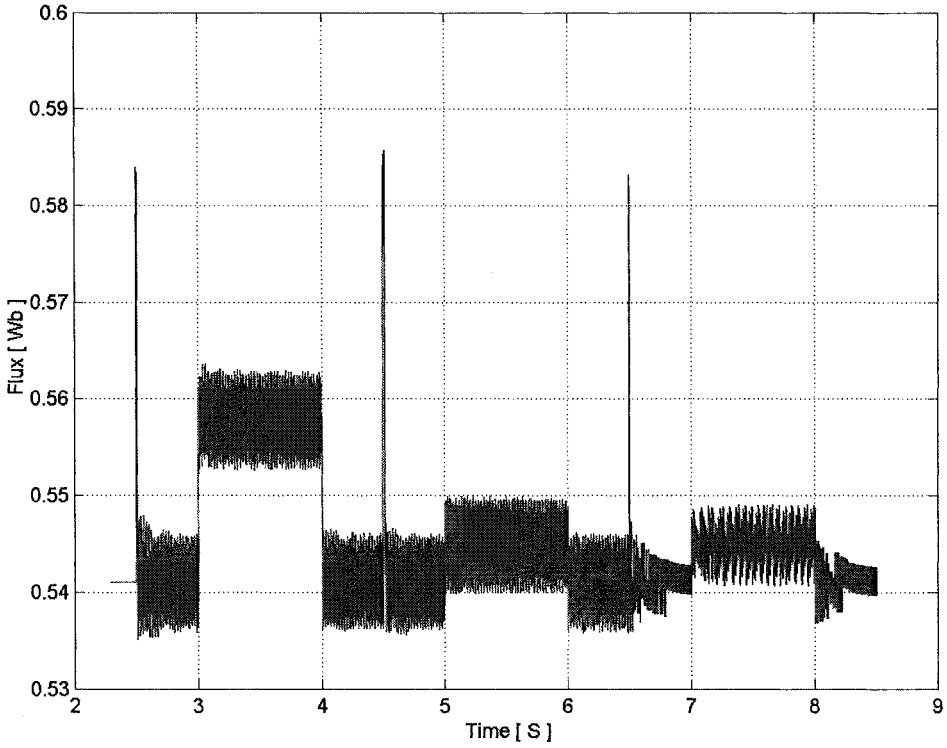

Figure 7.14(a) Secondary flux in sensor control mode

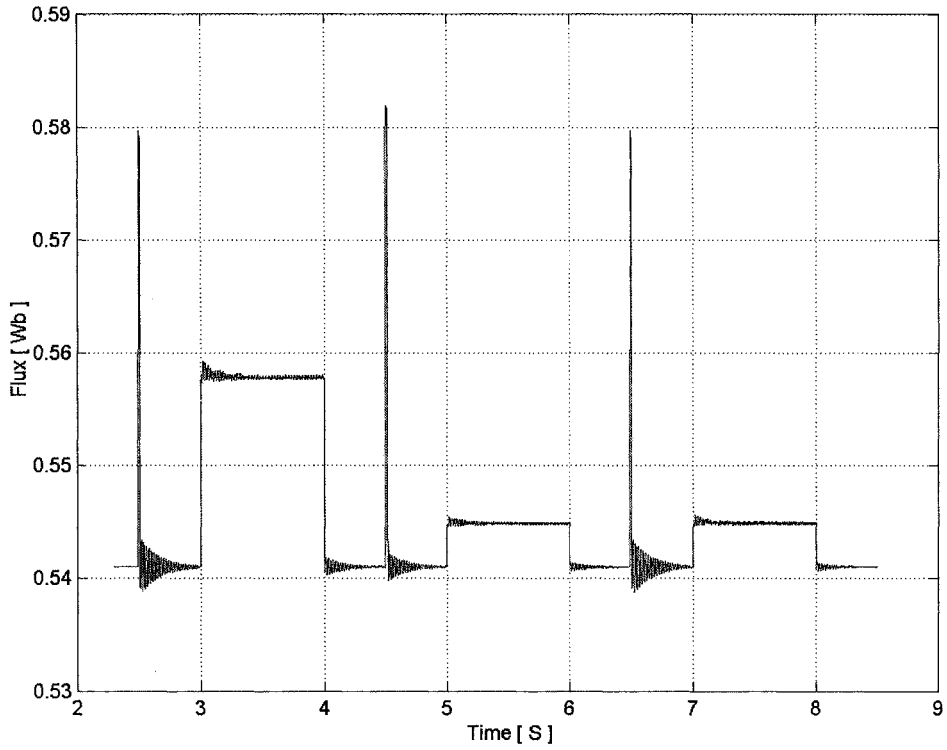

Figure 7.14(b): Flux reference in sensor control mode

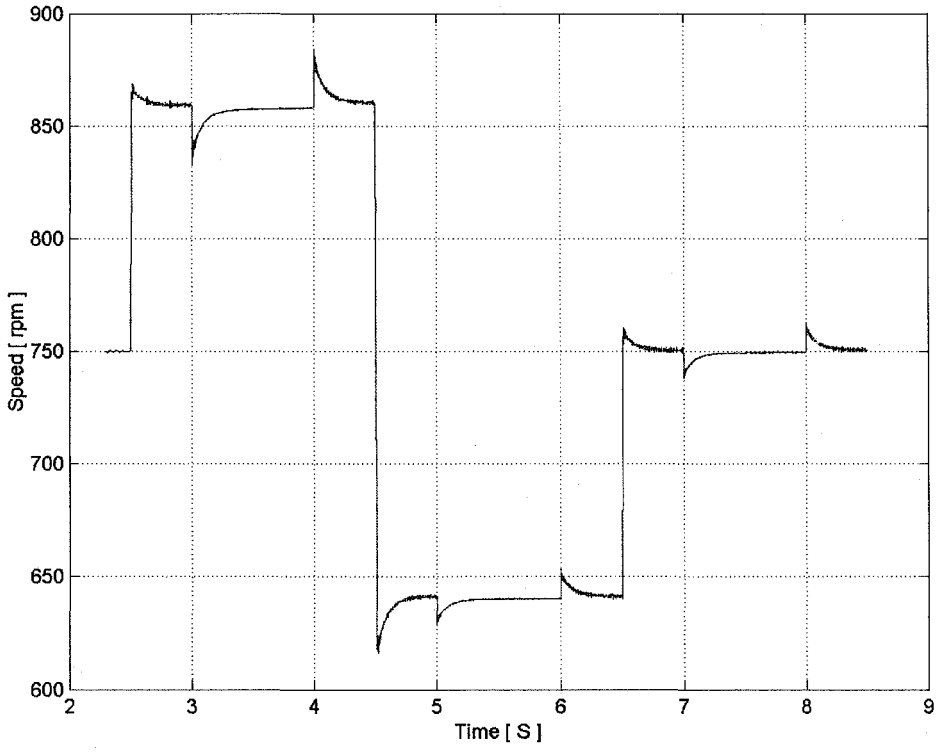

Figure 7.15(a) Speed response in sensorless control mode

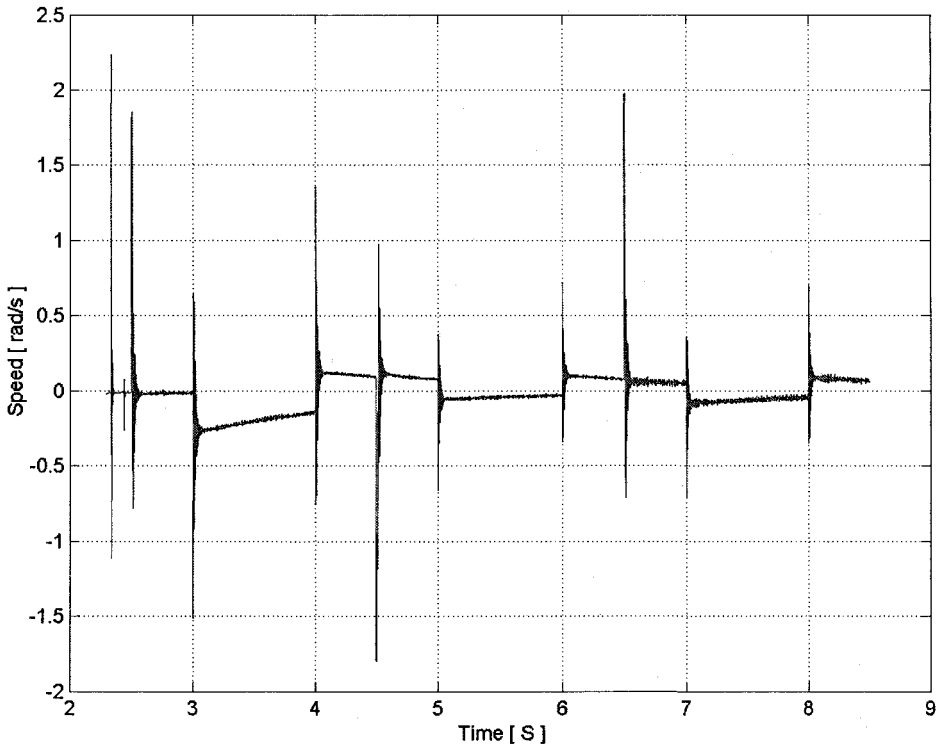

Figure 7.15(b) Absolute error of the estimated speed and the measured value

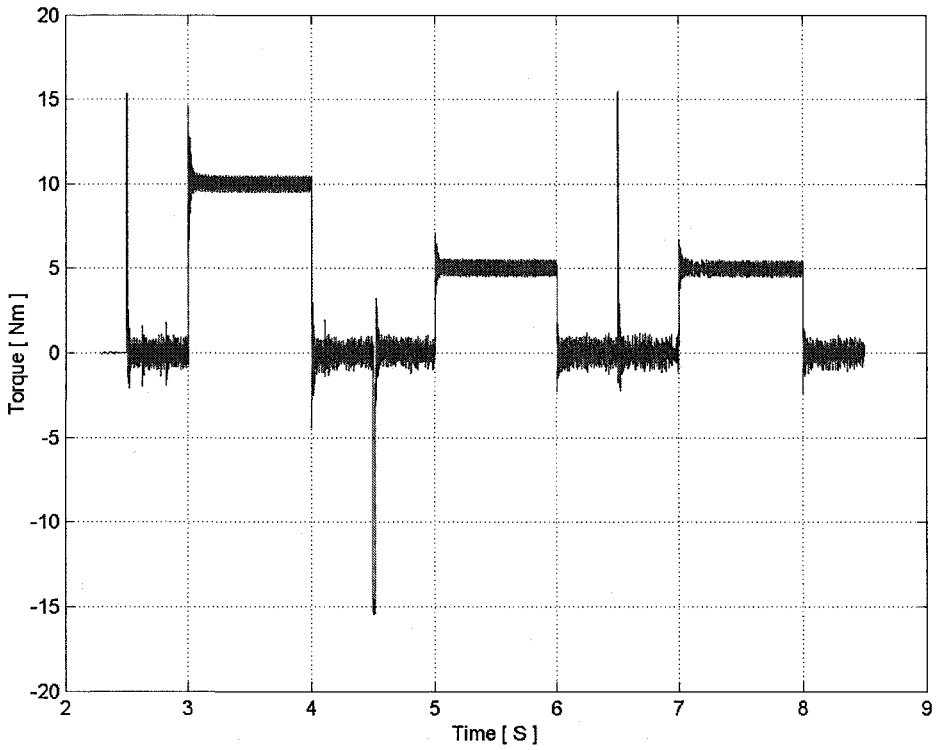

Figure 7.16(a) Electromagnetic torque in sensorless control mode

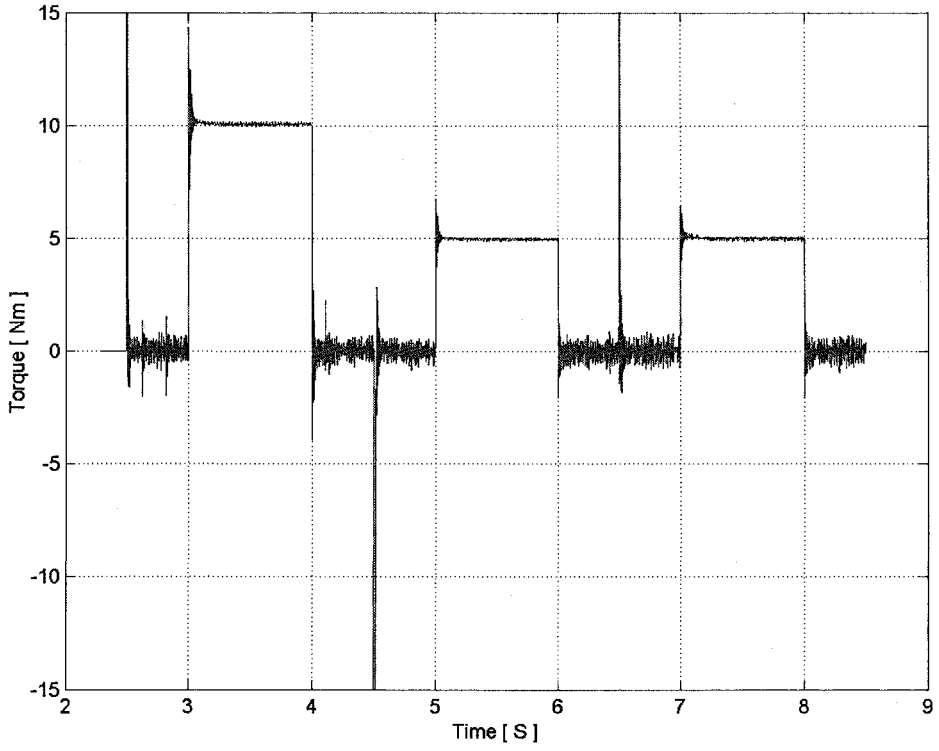

Figure 7.16(b) Torque reference generated in sensorless control mode

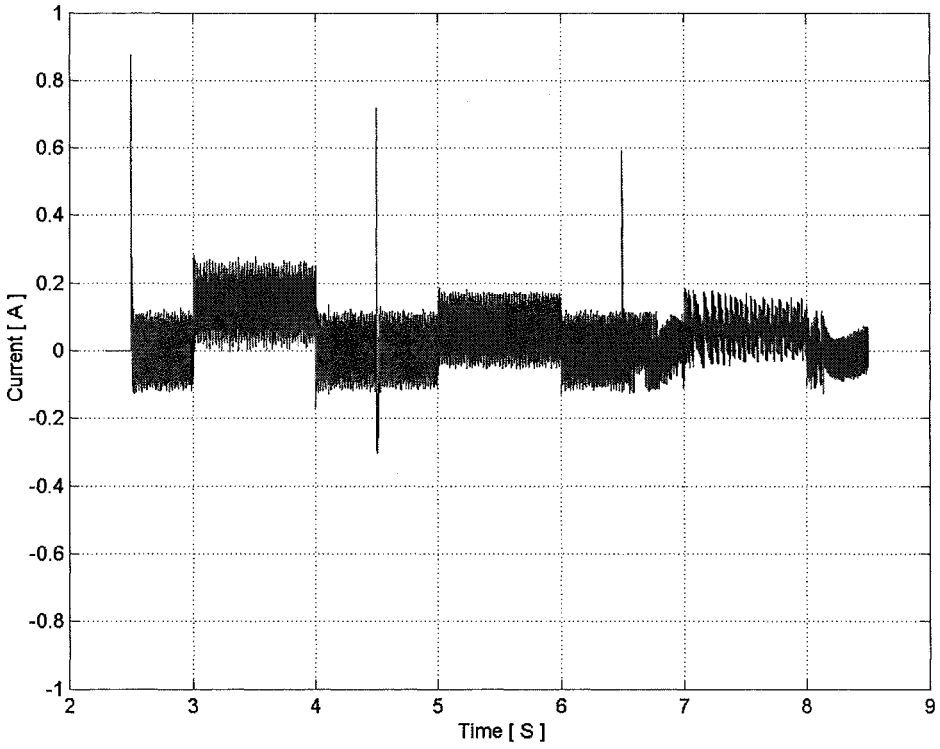

Figure 7.17(a) d-axis Secondary current component in sensorless control mode

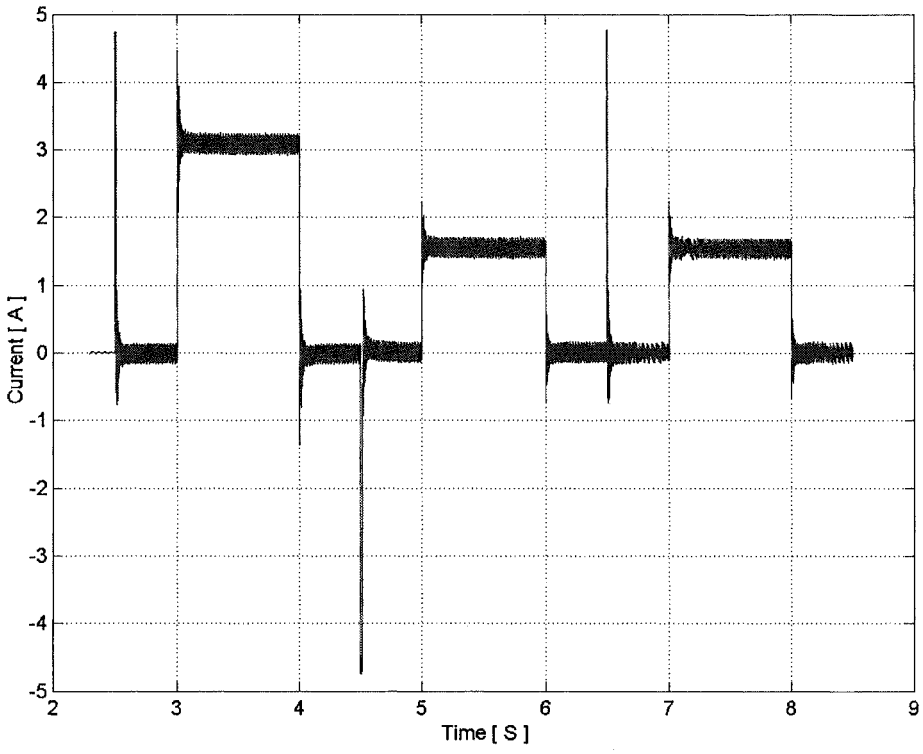

Figure 7.17(b) q-axis Secondary current component in sensorless control mode

Chapter 8 Experimental Results

The simulation results of the previous chapter have clearly demonstrated the good theoretical performance and prospective potential of the developed DTC scheme for the BDFRM in both the sensor and sensorless modes. Considering the fact that the state-of-the-art DSP kit from dSPACE® has been used in the BDFRM experimental test system and given its compatibility with Matlab®/Simulink® software platform, the Simulink® programme will serve as a basis for the control practical implementation. However despite the undoubtedly high portability, some significant, mostly digital hardware interface related modifications have to be made in order to adapt the simulation program for real-time use. The objective of the following sections is to outline these changes. Both the Simulink® programme and interface techniques have been appropriately changed to enable the control algorithm to be successfully implemented. The software modifications required have been elaborated in Section 8.1. The Sections 8.2 to 8.4 have explained the peripherals of the experimental controller. More detailed information on hardware components and respective tests can be seen in Appendices A and B.

In order to verify the simulation studies in Chapter 6 and Chapter 7, experimental results have been generated for a small 1.5 kW axially laminated 6/2 pole BDFRM prototype. The primary side of the machine stator is directly connected to a conventional 3-phase power supply of fixed voltage and frequency, while the

secondary side is connected to the mains via a power electronic converter. Both stator windings are rated at 415 V and 2.5 A. The remaining specifications and relevant design details of the machine can be found in Appendix A.1.

The promising performance of the controller simulator has been experimentally validated by the results presented in Section 8.5. The last section of the chapter is a summary of the relevant conclusions/observations that can be made from the test results.

8.1 Experimental Controller Design

The configuration of the experimental test rig is shown diagrammatically in Figure 8.1. and Pictures 5, 10 in Appendix C. As mentioned in the introductory paragraphs, the major software components and the control functions (Fig. 8.2) they perform are exactly the same in both the simulated and experimental controller. These are described in detail in Chapter 7 and won't be commented on again in this chapter. The main structural difference is naturally the absence of the machine simulator and the reference frame transformation corresponding to the rotating frame oriented machine model used for the simulation analyses. Instead, the machine voltages and currents are directly measured and so is the inverter DC link voltage (only for monitoring and protection purposes). In addition, an incremental encoder is employed in the experimental system to accurately detect the rotor position and to subsequently derive the machine speed. This is of course only relevant for the sensor control mode.

One of the main advantages of the dSPACE® system is its powerful 400MHz CPU. Therefore the main sampling and calculation duties are carried out by the DS1103 board itself. The function of the host PC will be mainly to monitor the system parameters and to act as an integrated screen display. In this sense the high PC processing power is not required. For this reason, in this experiment, an off-the-shelf 450 MHz PC is used. The details of the host PC for the DS1103 board can be found in Appendix B. The inverter hardware and encoder are interfaced with the I/O board by means of A/D data conversion ports. Picture 3 in Appendix C shows the interface board.

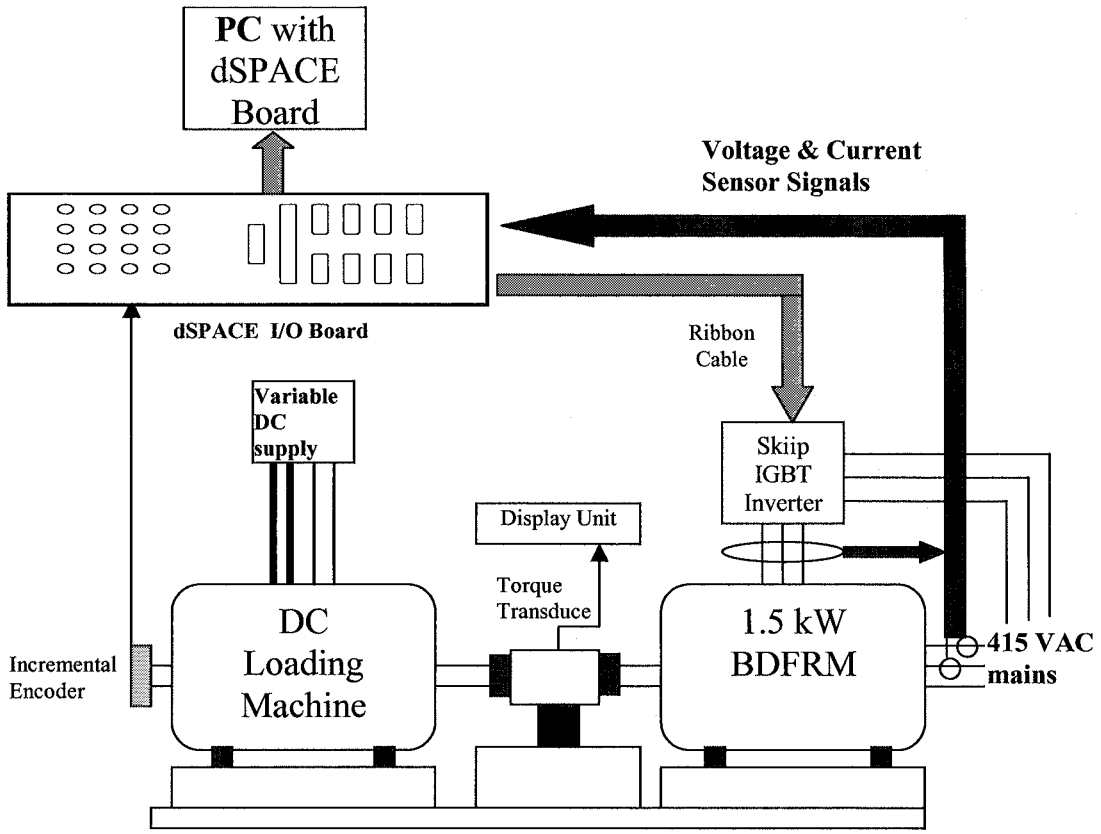

Figure 8.1 Experimental test system

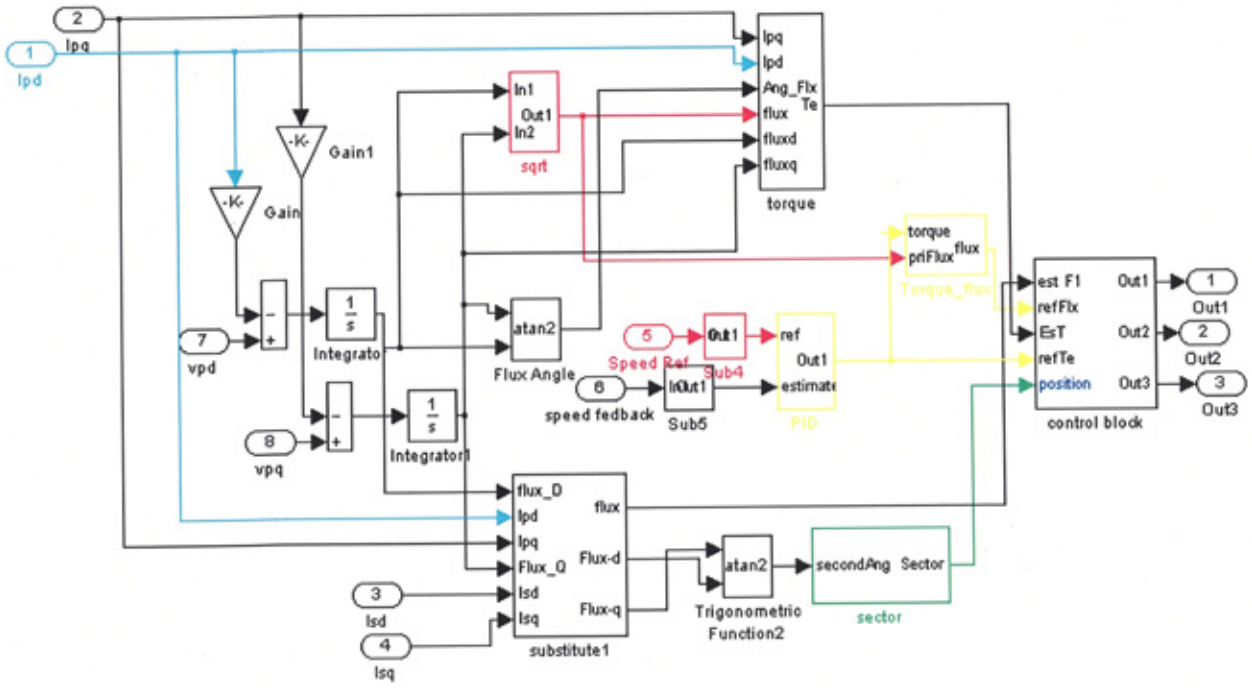

Figure 8.2 Main controller blocks

8.1.1 MAIN PROGRAMME

The controller in Figure 8.2 executes the duty of torque and flux estimation (formula were explained in Chapter 7), speed detection from the encoder measurements (for sensor control) or speed observation from the rotor position estimates (in case of sensorless control). Unlike the simulation programme mentioned in the previous chapters, the input signals to the real-time controller come from the dSPACE® I/O interface and the output of the controller are the TTL signals to the IGBT inverter drivers. As mentioned earlier the input variables are the primary voltages, primary currents, secondary currents and rotor mechanical velocity. Transducers are used to measure the electrical parameters. In the case of sensor control, an incremental

encoder is employed to get the rotor speed from the measured shaft position. This type of shaft position sensor is ideally suited to the stator frame based DTC as absolute rotor position information is not required but only the speed feedback for closed-loop speed control. It can be seen from Figure 8.2 that only the d and q stationary frame components of the measured voltages and currents are needed to enable the control calculations. Therefore, the typical Park's 3-phase to DQ transformation has been applied. Two transducers are generally sufficient per each electrical quantity being measured to capture all the necessary information for this conversion as the third phase variable immediately follows from the knowledge of the other two using $f_c = -f_a - f_b$ in which f can correspond to voltage or current. The reason for this is the balanced voltage supply and the fact that the machine Y-connected windings have been designed with an isolated neutral point. The requirement for two phase measurement also means that the overall cost and complexity of the instrumentation system has been reduced. Tests on each of the system components have been carried out to ensure their proper working conditions prior to their integration into the system. Issues related to this have been addressed in Appendix A.

8.1.2 SOFTWARE AND HARDWARE INITIALISATION

In real time implementation, initialisation procedures are necessary to set up both the software and hardware before control becomes active. Some of the software variables such as initial integrator value and the systems timers need to be reset each time the

system is switched on. Also initialisation of the I/O ports and A/D converter is essential. The machine itself is to be started and this is achieved in a manner similar to the wound rotor induction machine i.e. by short-circuiting the secondary windings. In the experimental system developed at Northumbria University, the power electronics is however considerably over-rated and is robust enough to withstand any inrush currents caused by dead on-line start of the small BDFRM prototype. This means that strictly speaking in this particular case the machine can be started with the inverter connected and the control enabled even from zero speed. In order to emulate the most common real-time situations where a small inverter is used, the machine is still started in its induction machine operating mode as previously mentioned. This has been accomplished by sending zero applied voltage signals to the IGBTs (i.e. either '000' or '111') which has effectively shorted the secondary windings. Doing so, the inverter has actually indirectly helped the machine to speed up and reach steady-state (by providing a short circuit of the windings) without being controlled. As with the induction machine, the rotor speed is near (but somewhat below) the synchronous value (750 rpm) and will be determined by the no-load slip. During starting, the controller ignores all of the sampled inputs by a zero set signal.

The encoder interface also needs to be properly initialised, especially if the absolute position information is required this fortunately not being the case here. After power-up the position counters contain arbitrary data, and therefore they should be synchronized by manually moving respective sensor until an index pulse is

encountered. To monitor the index lines, the index pulses are fed to the interrupt controller. When the position counter detects an index line (by polling the interrupt controller or by receiving an interrupt from it), it will either reset the respective position counters by setting the RSTINC1···5 flags in the INC (Index Counter) Reset Register, or set the counter by writing data to the position counter register to the absolute position of the connected plant.

8.1.3 INTEGRATOR SETTINGS

Both continuous and discrete integrators can be used in the hardware system. The discrete integrator makes use of the Forward Euler method requiring only information after one sampling point (e.g. two successive samples). The sampling time of the discrete integrator can be set to any value higher than the basic system step size, which is 5e-5s in this particular case. The continuous integrator is in fact a special case of the discrete integrator obtained by setting the sample time equal to the system step size. Testing has shown that by using either of these two integrators the same results are obtained due to extremely high sampling rates achievable with the DTC (note that the system step-size above, required by the CPU to perform all calculations, corresponds to 20 kHz control rate which is quite impressive even for DTC). Sending a step signal when the controller is on resets the integrator.

8.1.4 THE INTERFACE OF THE CONTROLLER

A user interface (Fig. 8.3) was designed to enable the user to specify the values of rotor pole number, inductances and resistance. These parameters are obtained from off-line tests the details of which can be found in Appendix A.1. The disadvantage of using the interface is that it slows down the controller operation. In the design of the controller it is crucial to make it computationally the least intensive so that the control execution time is reduced to a minimum. In the experiment where the system step size is set to 5e-5s (20 kHz) , it is decide to use blank settings instead of the user interface.

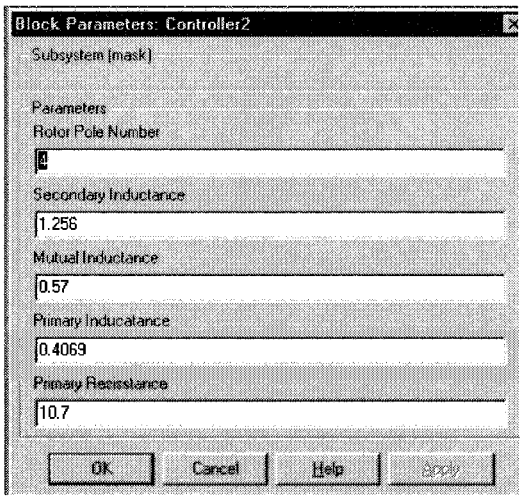

Figure 8.3 User interface of controller

8.1.5 AN ALTERNATIVE METHOD FOR ANGULAR VELOCITY ESTIMATION

As emphasized in the velocity observer section of Chapter 6, an alternative estimation approach of the rotor angular velocity from encoder measurements would be to apply the Euler's linear approximation of the position differential. This relatively simple method only requires knowledge of the incremental position over a certain time

interval which should be big enough to reduce the quantization errors to an acceptable level, and small enough to preserve the system dynamics. Its clear advantages over the observer algorithms are the load and machine parameter independence and simplicity. However, while the method may give accurate estimates at constant speeds, its transient performance is inferior to that of the observer algorithm, and it is more susceptible to quantisation noise, especially at lower speeds. For this reason, it is very suitable for dynamically less responsive systems where the steady-state operation is of major concern.

An expression similar to that in Chapter 6 is applied for estimating the rotor angular velocity:

$$\omega = \frac{\theta(n) - \theta(n-k)}{k\Delta} \tag{8.}$$

where $\theta(n)$ and $\theta(n-k)$ are the rotor positions that correspond to the encoder measurements at the n^{th} (current) and $(n-k)^{th}$ control sampling instants. It is evident that the estimate update at the control rate would result in significant estimation errors due to position measurement quantisation.

Obviously, to minimize the quantisation errors, the number of control intervals before the ω evaluation should be as large as possible. However, in order to have a satisfactory accuracy under transient conditions, the discretisation interval must be short, particularly when the machine is lightly loaded or unloaded. Therefore, the overall performance is a compromise between these two contradictory requirements; it is usually the transient that is sacrificed.

8.2 A/D Converters of The dSPACE System

There are two different types of A/D converters (ADC's) provided by the DS1103 PPC:

- Four 16-bit ADCs with Multiplexed Inputs, having a 250 KHz sampling rate;
- Four 12-bit ADCs with Non-Multiplexed Inputs, at 1.25 MHz sampling rate.

These converters will be used to read signals from both voltage and current transducers. Four Non-Multiplexed Inputs and two Multiplexed Inputs are used to sample the primary voltages, primary currents and secondary currents. In comparison with the 50 Hz power supply and the controller step size running at up to 20 KHz, the sampling rates of both of these ADC's are more than sufficient. The single ended bipolar inputs span for these converters is 20V [-10V, 10V peak value].

The current/voltage transducers are based on current transformer principles. Therefore, high-precision resistors are needed to achieve accurate voltage inputs. The *LEM*® current transducer and voltage transducer are chosen because of their reliability, galvanic isolation and fast responses. The accuracy of these devices is limited to within 2% (details can be found in Appendix A). To make full use of the specified accuracy, appropriately rated resistors are chosen to allow the transducer operation as close as possible to the maximum rated current. The calibration constants and conversion factors between the measured quantities and transducers outputs as well as the off-line tests being conducted to examine their performance are outlined in Appendix A.

8.3 Encoder Interface

Although an absolute optical encoder offers the actual rotor position directly, the use of an incremental optical encoder should be a favourable option when it comes to the dSPACE® implementation of DTC. Incremental encoders generally feature better 'value for money' as they are cheaper and yet much more accurate compared to absolute counterparts. They also have an additional advantage of being directly supported by the DS1103 system used hence significantly reducing the hardware development time. Furthermore, DTC is essentially sensorless in torque mode and the rotor position information is not required at all as the control is executed in a stationary frame. It is only the closed loop speed mode that requires the speed feedback but not the absolute position knowledge. From this point of view, and given the above preferable characteristics, the incremental encoder, used as a shaft speed sensor, is an ideal solution for this application.

Indeed the DS1103 provides an interface able to connect up to 6 incremental encoders. Incremental encoders typically use six signals: A rectangular signal, a 90° phase-shifted signal, an index pulse and their inverted counterparts. The encoder interface on the board generates an internal pulse for each encoder pulse, it determines the direction from the phase-shifted signal and it detects the index pulse. This information is processed by software on the DS1103, which calculates the position value that can be used in the Simulink® model. At each simulation step the underlying software directly reads the current position values.

Incremental encoders provide two 90° phase shifted signals, PHI0 and PHI90, and the index signal, IDX (Figure 8.4). In addition, most encoders also provide the inverted signals /PHI0, /PHI90 and /IDX. This means that the index signal is HIGH if A and B are also HIGH. This is exactly what the DS1103 interface expects.

The encoder position is read by DS1103 from an RTI block. However if the exact angular position is required, the RTI block would have to reset with the first encoder index signal; this is achieved using an interrupt (as mentioned in previous section). After the reset the absolute position of the encoder is known. If the RTI block is not reset, then the encoder will not have a reference point. In the case of the sensor DTC control, the incremental encoder can satisfy the requirements since the position difference is relevant for the angular velocity estimation.

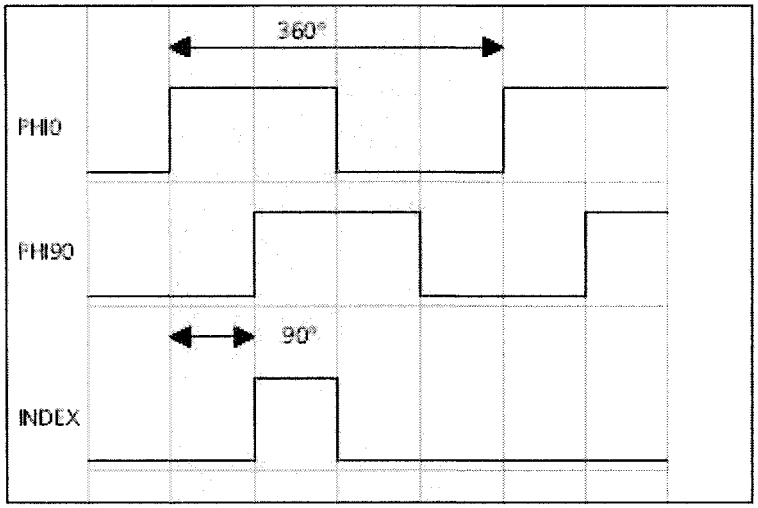

Figure 8.4 Signals from Figure 8. 1 encoder

In summary, an incremental encoder should be used in this experimental system because it is best supported by the DS1103.

The resolution of the encoder can be calculated by 360° / (4 * line count) since each cycle is divided into 4 sections to maintain 90° phase shift. It may be advantageous to use an encoder with a line count that equals a power of two (1024, 2048, 4096).

8.4 IGBT Inverter

An IGBT inverter used in the experimental system is the Skiip 132GDL120-412CTVU, a standard commercially available product from Semikron®. This unit is an intelligent integrated semiconductor system, rated at 100A, 900V. A conventional 3-phase full-bridge (6 pack) IGBT inverter is combined with a DC brake chopper with embedded 3-phase current sensors and a DC-link voltage sensor for protection. The unit has an integrated 15/24 V power supply as well as a temperature sensor. Normalized analogue voltage signals of the actual AC-current value, the actual ceramic substrate temperature value and the actual DC-link voltage are available at the DIN41651 gate driver connector of the **Skiip** system, for use in the control system if required. These voltage signals are smaller than 10V, which conforms to the dSPACE 1103 requirements. Therefore, these two compatible systems can be integrated easily. Other relevant details related to the IGBT inverter and its testing procedures can be found in Appendix **B**.

8.5 Experimental Results

The purpose of this section is to present the experimental results generated by executing the developed DTC algorithm on the custom designed and built BDFRM prototype.

Successful speed control of the machine can be observed from the plots in Figure 8.5 for a simple incremental speed test. The rotor speed reached the required speed (85 rad/s) in less 0.2s from the original value (near to its synchronous speed of 78.5 rad/s, but a little smaller due to its induction machine start process). The waveform is clear and smooth. Electromagnetic torque (Fig 8.6) obviously made full use of the PID capability since it reached its top constraint of 15Nm. A reference secondary flux (Fig. 8.7) was generated by using optimal formula stated in Section 7.2.3, Chapter 7. With a frequency relationship formula developed in Chapter 2, the positive frequency of the secondary side can be read from the current waveform in Figure 8.8. It might be noticed that the control was not applied to the machine until 1.8 s in the plot. It was due to the soft-start strategy mentioned in Chapters 6, 7.

Figs. 8.9-8.11 shows the machine's performance following a set of different speed commands.

- Machine was started by shorting the secondary circuit and running in steady state before 6.5 s;

- A speed reference of 85 rad/s (above synchronous speed) was placed at 6.5 s ;
- the speed reference changed to 72.5 rad/s (below synchronous speed) at 12.5 s;
- at 18.5 s, the speed reference changed to synchronous speed of 78.5 rad/s.

The change of speed in Figure 8.11 followed the control command described above. The optimal tuning of PI speed controller will of course influence the control result. The most significant part of this test is that the machine was running well at synchronous speed. The DC secondary current of Figure 8.12 further confirms the relationship between rotor speed and primary frequency. It is not usual for an induction machine to be controllable at standstill (which is equivalent to synchronous speed for BDFRM) or low speed range due to the flux estimation techniques using. The experiment result exhibits the advantages of BDFRM, e.g. can be controlled by DTC over speed range covering synchronous speed, and the potential for the torque and flux estimation techniques used to achieve optimal control. When rotor speed is below synchronous speed, the secondary current shows 'negative' frequency in that the d-axis component is lagging the q-axis current.

8.6 Conclusions

Direct Torque Control was applied to a proto-type Bruless Doubly-Fed Reluctance Machine. The experiment results in this Chapter, together with theoretical simulation plots in Chapter 7, demonstrate successful speed and torque control over sensitive

speed range including synchronous speed and promising potential for the estimation techniques used in the project.

While both speed and torque are controlled in a feasible way as shown, the flux was not optimal controlled. Control inaccuracies under transient condition are likely due to some problems such as numerical sensitivity of the secondary flux estimator. It is known [43,45,87] that flux reference could be set independently in line with machine's optimal operation condition. This will be further addressed in Chapter 9.

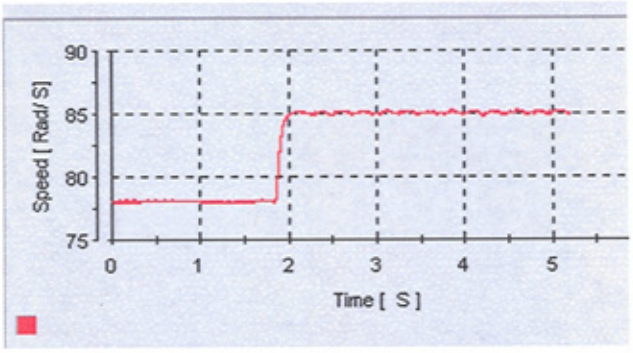

Figure 8.5 Speed plot following a reference to 85 rad/s (super-synchronous speed)

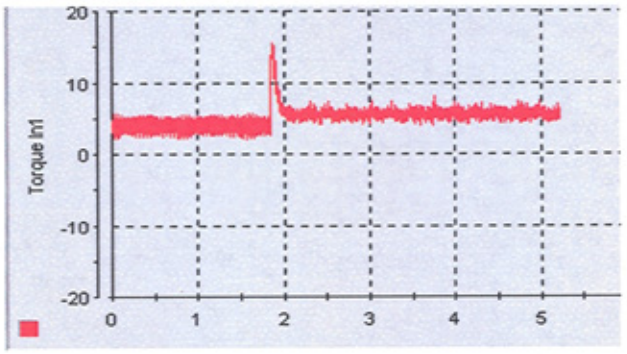

Figure 8.6 Torque response at a speed increment procedure

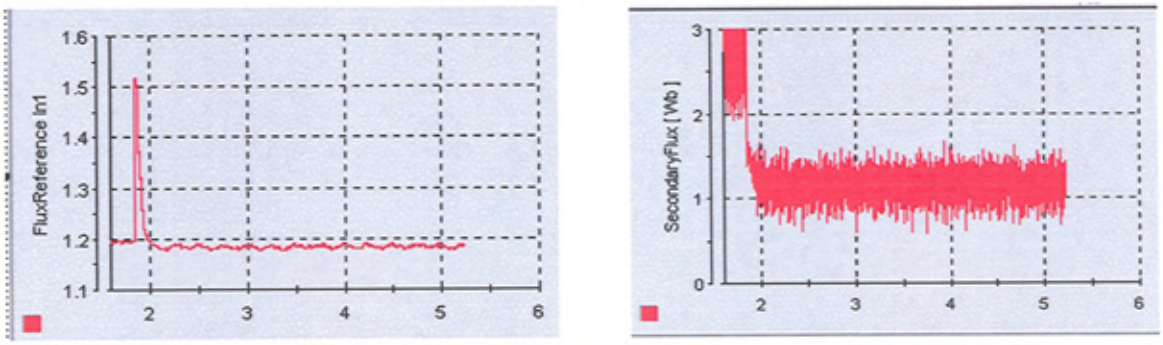

Figure 8.7 The flux control by DTC on BDFRM (start from 1.8 s) left: secondary flux reference; bottom left: secondary flux response

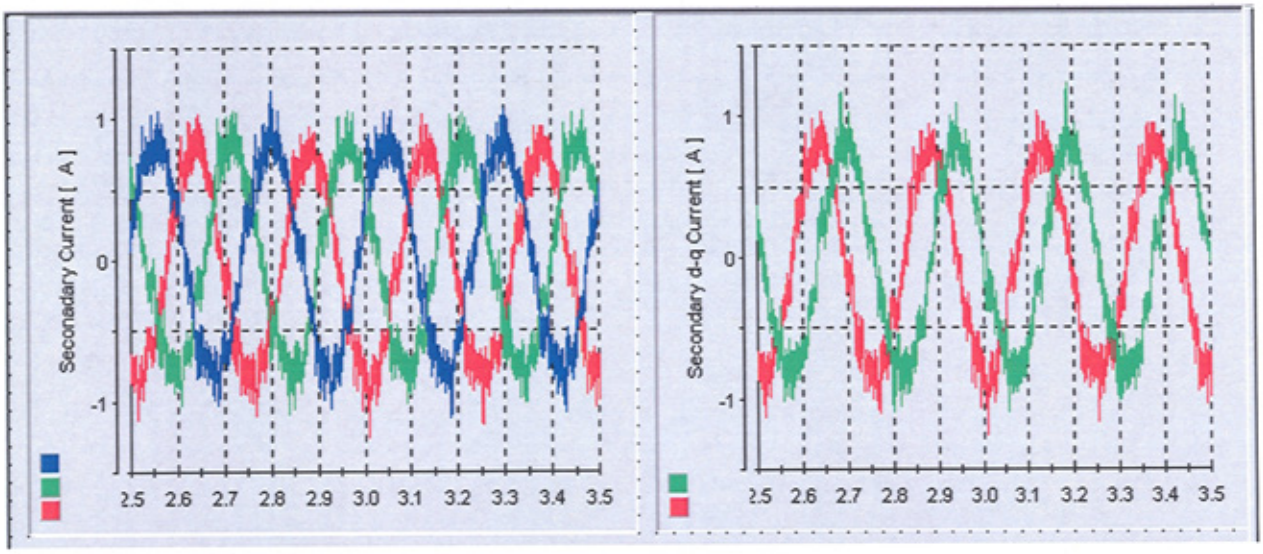

Figure 8.8 The secondary current under control. Left: three-phase currents; right: d-q components of secondary current, d-axis current is in red.

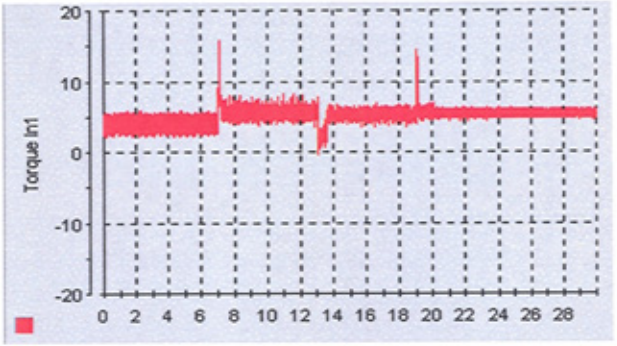

Figure 8.9 Torque response on speed control

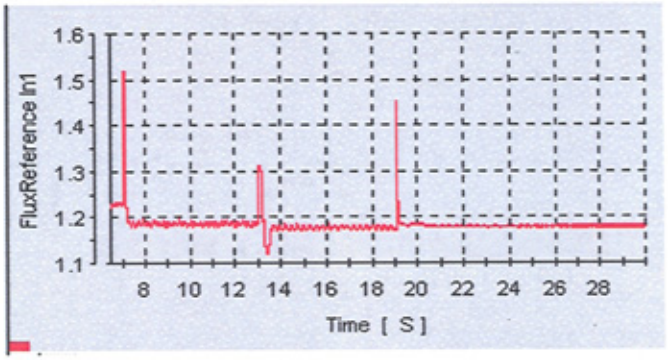

Figure 8.10 reference value for secondary flux

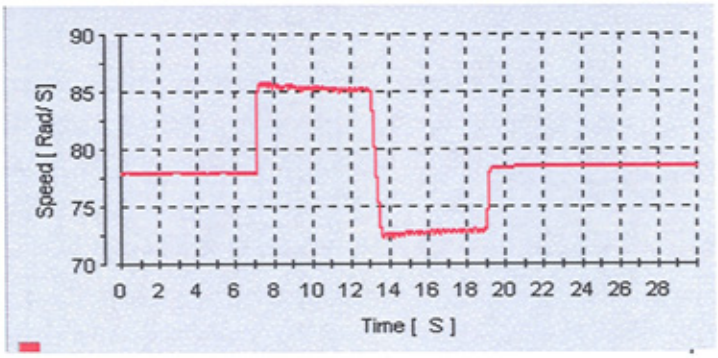

Figure 8.11 the corresponding speed running above, below and at synchronous speed

Figure 8.12 The current in different states

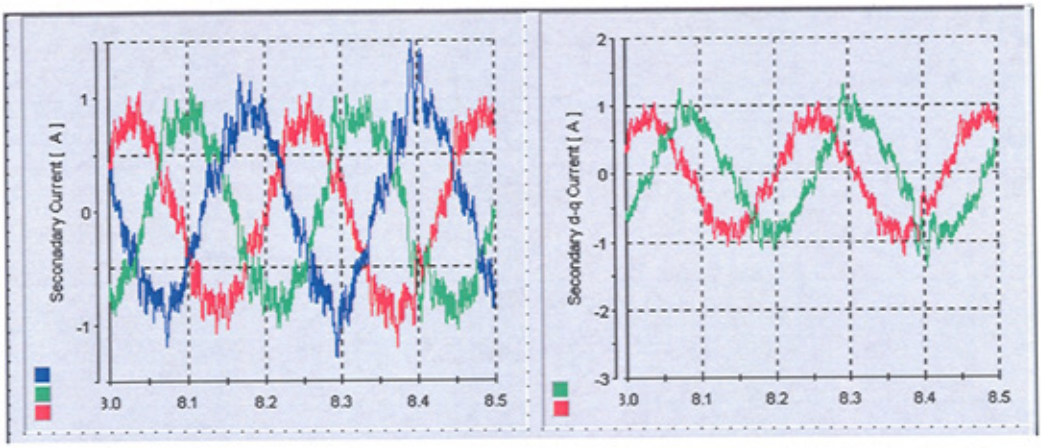

status I: positive secondary current d-axis component is in advance of q-axis component

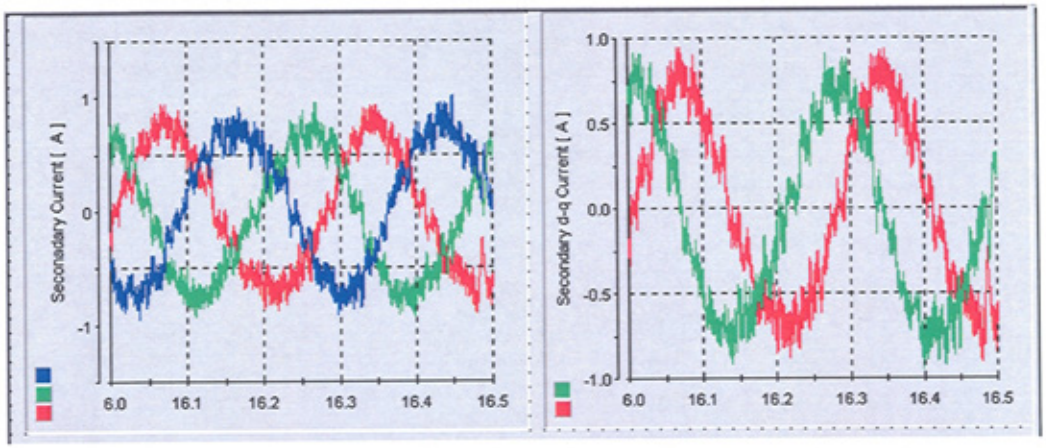

status II: negative secondary frequency when rotor speed is below synchronous speed

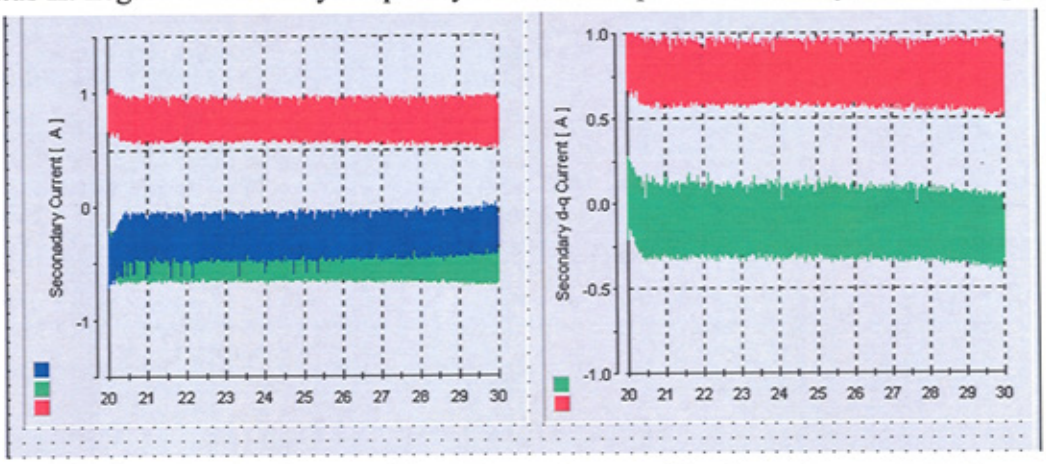

Status III: direct current in secondary when rotor speed is at synchronous speed

Chapter 9 Conclusions and Further Work

Verified by hardware experiment, the principle of Directly Torque Control on Brushless Doubly Fed Reluctance Machine was established in the thesis. The primary concern of the project was to verify the concept in both computer simulation and real time experiment, which has been achieved. There are, however, some aspects requiring further study. This chapter is trying to conclude the project and make some recommendations for the possible future extension.

The chapter is composed of two sections. The first part of the chapter concludes the thesis. The second part of the chapter suggests that a more completed BDFRM model can be developed when saturation and iron loss are considered. This completed model should provide a good approach to the real time experiment. The improvement of estimation techniques recommended is to use on line parameter estimation. For emerging industry, wind power generation shows its promising potential for this project.

9.1 Conclusions

The thesis developed an ideally linear mathematic model of BDFRM. The BDFRM model was tested under different loading conditions at different speed. The maximum

torque per secondary ampere strategy was tested and has been justified by the final plots.

Based on the relationship between secondary stator current angle and electro-magnetic torque, a modified look-up table, based on DTC philosophy, was used for BDFRM. Both computer simulation and real time experiment test results were presented in the thesis. Comprehensive computer simulation studies were curried out for either sensor or sensorless DTC control. The corresponding torque and secondary flux estimation techniques enabled final control.

The control algorithm developed for BDFRM in the thesis has a high accuracy and could work the whole working range, above and below synchronous speed. The impact of parameter changes during working condition was considered and analysed. Due to the similarity of machine models, the same DTC control scheme can be used for conventional Doubly-Fed Induction Machines.

In conclusion, this thesis has presented a real time digital Direct Torque Control controller for a 1.5 kW axially laminated BDFRM. The DTC controller was implemented in Simulink®, Matlab®. dSPACE® control board was used as the compiler and interface between PC and other hardware components in real time tests. DTC controlled BDFRM was experimentally shown to be capable of fast speed control over a sensitive range around synchronous speed.

9.2 *Extensions*

9.2.1 MACHINE MODEL

In Chapter 6, Chapter 7, the control of BDRM was the application of an idea model (no saturation or losses) for the theoretical analysis and practical implementation. However, in a real machine the effects of saturation and iron losses result in variations of the optimal current angles from those predicted by the idea model. Therefore, in order to have a better insight into the machine behaviour these practical effects shall be taken into account and deserve particular attention.

As shown in Fig. 1.1 in Chapter 1, reluctance machine rotor is defined in such a way that flux path along q-axis is dominated by air resulting in a minimal saturation. Consequently, the L_q inductance is very small and almost constant under all operating conditions and can be considered to be the unsaturated value. The high permeance d-axis, on the other side, usually shows significant saturation, particularly when the machine is being operated at small current angles.

The d-axis saturation is the combined effect of saturation in the stator yoke, stator teeth, and rotor laminations and be substantially reduce the L_d inductance.

9.2.2 ON-LINE PARAMETER ESTIMATION

The speed observer based controller for the test presented in this thesis has been implemented using measurements of machine and load parameters. Therefore, the

application of the controller to a particular machine requires that these parameters have been previously determined by off-line testing as stated in Appendix A. In addition, the stator resistance variations due to temperature changes and skin effects can not be taken into account and it is usually assumed constant. This may deteriorate control performance if the machine is loaded at low speed.

These limitations can be overcome by identifying the machine parameters on-line. This approach has several significant advantages.

- the inverter-controller system would become decoupled from the machine to some degree. Hence, for a given power rating, an inverter can support a variety of different machines without having to modify any look-up tables.
- the controller itself would be more versatile, and if implemented on a DSP it would be commercialised.
- the heavy parameter dependence of the sensorless control algorithm can be eliminated or at least reduced. This would further improve its effectiveness and accuracy;

There are a number of on-line parameter estimation methods [69]. Such techniques are applicable to the estimation of the *d-q* inductances, stator resistance and inertia constant of the BDFRM using a conventional d-q model in discrete form. One PI compensation for stator resistance has been proposed in [69].

It has been noticed that flux control in real time experiment was not optimal. This might attribute to numerical problems since secondary flux is dominated by primary flux as stated in Section 7.2.3, Chapter 7 and real time signals, if not good in quality, will have impact on estimated value. Flux control is independent with torque control in DTC philosophy. Flux estimation can therefore be substituted by a constant value which is in line with machine's optimal operation condition. Alternatively, flux estimation can also make use of traditional PI controller to compensate the estimated value.

9.2.3 BDFRM IN WIND POWER GENERATION

Since wind power generation is one of the most important potential application areas of Brush-less Doubly Fed Reluctance Machine, it is beneficial to extend the work in this field. The most obvious advantage of BDFRM is the brushless structure with the partial rated power electronics. As mentioned in Chapter 2, Doubly Fed Induction Machine got the same advantage to save the capital of power electronics. An outstanding example in wind power generation is the over-synchronous cascade arranged turbine: AWEC-60 (1200 KW) at Cabo Villano, Spain. In that case, part of the electrical power is taken from the generator rotor at over-synchronous speeds, through slip-rings[89]. In this case, the absence of the brush offers the better position of BDFRM. It will be the direction of this research to be extended to wind power generation.

Reference:

1. Ian Boldea, "Reluctance Synchronous Machines and Drives", Oxford University Press,1996, ISBN 019 8593910
2. R.E.Betz and M.Jovanovic, "The Brushless Doubly Fed and the Synchronous Reluctance Machine – a comparison", *IEEE Transactions on Industry Applications*, Vol. 36, No. 4, pp.1103-1110, July/Aug 2000.
3. L.Xu, Y.Tang, L.Ye, "Comparison study of rotor structures of doubly excited brushless reluctance machine by finite element analysis", *IEEE Transactions on Energy Conversion*, vol. 9, no. 1, 1994, pp. 165-172.
4. R.Betz and M.G.Jovanovic, "Comparison of the brushless doubly fed reluctance machine and the synchronous reluctance machine", Tech. Rep., Department of Electrical Energy Conversionm Institute of Energy Technology, Aalborg University, Denmark, October, 1998
5. M.S.Boger, A.K.Wallace, R.Spee, R.Li, "General pole number model of the brushless doubly-fed machine", *IEEE Transactions on Industry Applications*, vol. 31, no. 5, 1995, pp. 1022-1028.
6. P.Tiitnen, P. Pohjalainen and J. Lalu, "The next generation motor control method: direct torque control", *EPE Journal, vol.*5, No.1, 1995, pp. 14- 18
7. Y.Liao, "Design of a brushless doubly-red induction motor for adjustable speed drive applications", *IEEE-IAS Annual Meeting*, San Diego, California, 1996, pp. 850-855.
8. I.Takahashi, T.Noguchi, "A new quick-response and high-efficiency control strategy of an induction motor", *IEEE Transactions on Industry Applications*, vol. IA-22, no. 5, 1986, pp. 820-827.
9. P.Vas, "Sensorless Vector And Direct Torque Control", Oxford University Press, 1998. ISBN 0198564651
10. A.R.W.Broadway, L.Burbridge, "Self-cascaded machine: a low-speed motor or high frequency brushless alternator", *Proc. IEE*, vol. 117, no. 7, 1970, pp. 1277-1290.
11. C.P.Steinmetz, "Operating alternating motors", US Patent 587340, 1897.
12. B.Hopfensperger, D.J.Atkinson, R.A.Lakin, "Stator flux oriented control of a cascaded doubly-fed induction machine", *IEE Proc.-Electr. Power Appl.*, vol. 146, no. 6, 1999, pp. 597-605.
13. H.Hopfesperger, D.J.Atkinson, Doubly-fed a.c machines: classification and comparison, EPE 2001, Graz
14. F.Creedy, "Some developments in multi-speed cascade induction motors", *Journal IEE*, vol. 59, 1921, pp. 511-532.
15. A.R.W.Broadway, "Cageless induction machine", *Proc. IEE*, vol. 118, no. 11, 1971, pp. 1593-1600.
16. L.J.Hunt, "A new type of induction motor", *Journal IEE*, vol. 38, 1907, pp. 648-667
17. F.Liang, L.Xu, T.A.Lipo, "D-q analysis of a variable speed doubly AC excited reluctance motor", *Electric Machines and Power Systems*, vol. 19, 1991, pp. 125-138.
18. D.Zhou, R.Spee, G.C.Alexander, "Experimental evaluation of a rotor flux oriented control

algorithm for brushless doubly-fed machines", *IEEE Transactions on Power Electronics*, vol. 12, no. 1, 1997, pp. 72-78.

19. W.R.Brassfield, R.Spee, T.G.Habetler, "Direct torque control for brushless doubly-fed machines", *IEEE Transactions on Industry Applications*, vol. 32, no. 5, 1996, pp. 1098-1104.
20. Y.Liao, C.Sun, "A novel position sensorless control scheme for doubly fed reluctance motor drives", *IEEE Transaction on Industry Applications*, vol. 30, no. 5, 1994, pp. 1210-1218.
21. O.Ojo, Z.Wu, "Performance characteristics of dual-winding reluctance generators", *IEE Proc. – Electr. Power Appl.*, vol. 144, no. 6, 1997, pp. 461-468.
22. L.Xu, L.Zhen, E.H.Kim, "Field-orientation control of a doubly-excited brushless reluctance machine", *IEEE Transactions on Industry Applications*, vol. 34, no. 1, 1998, pp. 148-155.
23. R.Li, R.Spee, A.K.Wallace, G.C.Alexander, "Synchronous drive performance of brushless doubly-fed motors", *IEEE Transactions on Industry Applications*, vol. 30, no. 4, 1994, pp. 963-970.
24. Y.Liao, L.Zhen, L.Xu, "Design of a doubly fed reluctance motor for adjustable-speed drives", *IEEE Transactions on Industry Applications*, vol. 32, no. 5, 1996, pp. 1195-1203.
25. B.V.Gorti, D.Zhou, R.Spee, G.C.Alexander, A.K.Wallace, "Development of a brushless doubly-fed machine for a limited-speed pump drive in a waste-water treatment plant", *IEEE-IAS Annual Meeting*, Denver, Colorado, 1994, pp. 523-529.
26. L.Xu, Y.Tang, "A novel wind-power generating system using field orientation controlled doubly-excited brushless reluctance machine", *IEEE-IAS Annual Meeting*, Houston, Texas, 1992, pp. 408-413.
27. S.Williamson, A.C.Ferreira, A.K.Wallace, "Generalised theory of the brushless doubly-fed machine. Part 1 : Analysis", *IEE Proc. – Electr. Power Appl.*, vol. 144, no. 2, 1997, pp. 111-122.
28. S.Williamson, A.C.Ferreira, "Generalised theory of the brushless doubly-fed machine. Part 2: Model verification and performance", *IEE Proc. – Electr. Power Appl.*, vol. 144, no. 2, 1997, pp. 123-129.
29. L.Xu, W.Cheng, "Torque and reactive power control of a doubly fed induction machine by position sensorless scheme", *IEEE Transactions on Industry Applications*, vol. 31, no. 3, 1995, pp. 636-642.
30. R.Pena, J.C.Clare, G.M.Asher, "Doubly-fed induction generator using back-to-back PWM converters and its application to variable speed wind-energy generation", *IEE Proc.-Electr. Power Appl.*, vol. 143, no. 3, 1996, pp. 231-241.
31. B.Hopfensperger, D.J.Atkinson, R.A.Lakin, "Stator flux oriented control of a doubly-fed induction machine with and without position encoder", *IEE Pro.-Electr. Power Appli.,July, 2000, pp 241-250.*
32. E.Galvan, J.M.Carrasco, R. Ortega, G.Escobar and A.M. Stankovic, "A family of switching control systems for the reduction of torque ripple on the direct torque and flux control for induction motors", *IECON'01, IEEE*, USA, 2001
33. R.Betz and M.G. Jovanovic, "Theoretical analysis of control properties for the brushless doubly fed reluctance machine", Newcastle University, Australis,1998
34. R.E.Betz and M.Jovanovic, "Introduction to the space vector modelling of the brushless doubly-fed reluctance machine", *Electric Power Components and Systems* journal, Vol.31, No.8, pp. 729-755, August, 2003

35. O.Ojo, Z.Wu, "Modelling of the doubly reluctance machines using harmonic balance technique and manley-rowe power frequency relationships", IEEE, IAS,1996, pp794-800
36. E.Hajdu , R.K.Jardan, "Voltage source inverter drive with direct torque control", Power electronics and U.S drives , pp80-85
37. T.Noguchi, M. Yamamoto, S.Kondo and I.Takahashi, "Enlarging switching frequency in direct torque-controlled inverter by means of Dithering", *IEEE trans. on IA, vol. 35, No.6, Novermber/December*, p.199
38. D.W. Novotny, T.A. Lipo, "Vector control and dynamics of AC drives", Oxford university press, 1996
39. A.M. Trzynadlowski, " Control of induction machine motors", Academic press, 2000
40. O.Ojo, "Field orientation control of a doubly-fed synchronous reluctance machine", vol.2, IEEE annual meeting, Japan, 1998
41. J. N. Nash, "Direct torque control, induction motor vector control without an encoder", *IEEE trans. on IA, vol.* 33, *No.* 2, March/April, 1997
42. D. Casadei, G. Grandi, G Serra, "Rotor flux oriented torque control of induction machines based on stator flux vector control", *IEE*, 13-16 September 1993, vol.5, pp 67-72
43. D. Casadei, G. Grandi, G Serra and A. Tani, "Effects of flux and torque hysteresis band amplitude in direct torque control of induction machines", *IEEE,* IECON' 94, Bologna, Italy
44. N.Mohan, "Power Electronics" , New York, Chishester, 1995
45. M.P. Kazmierkowski and A. B. Kasproics, "Improved direct torque and flux vector control of PWM inverter-fed induction motor drives", *IEEE Trans. Ind Electro., vol.* 42, pp 344-350, Aug. 1995
46. X. Roboam, "A special approach for the direct torque control of an induction motor", in 1st European Technical Scientific Report, Naples, Italy, Feb. 1996, pp 216-225;
47. E. Flash and R. Hoffmann, "Direct mean torque control of induction motor", in *proc.* EPE'97, Torndheim, Norway, Sept, 1997, pp 3.672-3.677.;
48. Y.Li, J. Shao and B. Si , "Direct torque control of induction motors for low speed drives considering discrete effects of control and dead-time of inverters", *IEEE annual meeting*, 1997;
49. J. Kang and S Sul, "New direct torque control of induction motor for minimum torque ripple and constant switching frequency", *IEEE tran. on industry applications, vol.* 35, 1999, pp 1076-1082
50. D.Casader, G.Serra and A. Tani, "Performance analysis of a DTC control scheme for induction motor in the low speed range", EPE, Trondheim, 1997
51. Casadei D., Grandi G, Serra G., Tani A., "Switching strategies in direct torque control of induction machine", ICEM' 94, Paris, France, pp204-209;
52. T.G.Habetler, F. Profumo, L.M. Tolbert, "Direct torque control of induction machines using space vector modulation", *IEEE trans. IA, vol.* 28, No. 5., spet/oct, 1992, pp 1045-1053
53. L.Zhong M.F. Raham, W.Y. Hu and K.W.Lim, "Analysis of Direct Torque Control in Permanent Magnet Synchronous Motor Drives", IEEE, transactions on power electrnoics, vol. 12, No. 3, May 1997
54. I. Takahashi, Y Ohmori, "High-performance direct torque control of an induction motor", *IEEE, trans. IA,* vol.25, No.2. 1989 D.A. Bradly, "Power Electronics", London, chapman and Hall, 1995

55. T.Kanmachi and I Takahashi, "Sensor-less speed control of an induction motor", IEEE industry Applications Magazine, January/February , 1995
56. W. R. Brassfield and R. Spee, T. G. Habetler, "Direct torque control for brushless doubly fed machines", IEEE industry applications society annual meeting, 1992, pp. 615-622
57. George Mcpherson, "An introduction to electrical machines and transformers", John Wiley and Sons, 1989
58. D.W. Novotny and R.D. Lorenz(Eds), "Introduction to field orientation and high performance ac drives", in tutorial course Record of Annual Meeting. IEEE Industry Applications Soc.,1985,1986
59. B. Friendland, control system design, New york, mcgraw hill,1986
60. R.E.Betz and M.Jovanovic, "Theoretical analysis of control properties for the brushless doubly-fed reluctance machine", *IEEE Transactions on Energy Conversion*, Vol.17, No.3, pp. 332-339, September,2003
61. B. Friendland, control system design, New York, Mcgraw Hill,1986
62. G.Armstrong, D.J.Atkinson, "A comparison of model reference adaptive system and extended kalman filter estimators for sensorless vector drive", *EPE*, Trondheim, 1997
63. N.R.N. Idris, A.H. M. Yatim, "a reduced torque ripple controller for direct torque control of induction machines", electrical power components and systems, May,1999, pp. 507-24
64. M.Jovanovic and R.E.Betz, "Control Strategies for Brushless Doubly Fed Reluctance Machines", *Transactions of IEE-J*, Vol.121-D, No. 2, pp. 272-278, February 2001.
65. R.B.Inderk, R.W.DeDoncker, "Direct instantaneous torque control of switched reluctance drives" , 2002 , IEEE, ISA, Annual meeting, U.S.A. pp. 1065-9
66. S.Arnalte, J.C.Burgos,J.L. Rodriguez-Amenedo, Direct torque control of a doubly-fed induction generator for variable speed wind turbines, electric power components and systems, 30: pp199-206, 2002
67. M.Jovanovic and R.E.Betz, "Off-line testing of reluctance machines", *IEEE Transactions on Energy Conversion*, Vol. 14, No. 3, September 1999.
68. M.Jovanovic and R.E.Betz, "Optimal torque controller for synchronous reluctance motors", *IEEE Transactions on Energy Conversion*, Vol. 14, No. 4, December 1999.
69. M.Wang, E.Levi and M.Jovanovic, "Compensation of parameter variation effects in sensorless indirect vector controlled induction machines using model based approach", *Electrical Machines and Power Systems Journal*, Vol. 27, No. 9, 1999.
70. M.Jovanovic, R.E.Betz and D.Platt, "Sensorless Vector Controller for a Synchronous Reluctance Motor", *IEEE Transactions on Industry Applications*, Vol. 34, No. 2, March/April 1998.
71. M.Jovanovic and R.E.Betz, "The use of doubly fed reluctance machines for large pumps and wind turbines", *IEEE IAS'2001 Annual Meeting*, Chicago, USA, September,2001
72. M.Jovanovic, J.Yu and E.Levi, "A review of control methods for brushless doubly-fed reluctance machines", *IEE Power Electronics Machines and Drives (PEMD) Conference*, Bath, April 2002.
73. M.Jovanovic and R.E.Betz, "Slip power recovery systems based on brushless doubly-fed reluctance machines", *IEEE Power Conversion Conference (PCC)* in Osaka, Japan, April 2002.
74. M.Jovanovic, J.Yu and E.Levi, "Control methodologies for brushless doubly-fed reluctance

machines", ICEM, Bruges, Belgium, August 2002.
75. M.Jovanovic, R.E.Betz, J.Yu and E.Levi, "Aspects of Vector and Scalar Control of Brushless Doubly Fed Reluctance Machines", IEEE Power Electronics and Drive Systems (PEDS) Conference, Bali, Indonesia, October 2001.
76. M.Jovanovic and R.E.Betz, "The use of doubly fed reluctance machines for large pumps and wind turbines", *IEEE IAS'2001 Annual Meeting*, Chicago, USA, September/October 2001.
77. M.Jovanovic and R.E.Betz, "A comparative analysis of doubly fed reluctance machine's performance parameters", *European Power Electronics (EPE'01) Conference*, Graz, Austria, August 2001.
78. M.Jovanovic and R.E.Betz, "Power factor control using brushless doubly fed reluctance machines", *IEEE IAS'2000 Annual Meeting*, Rome, Italy, October 2000.
79. M.Jovanovic, "Power factor and inverter rating – a compromise in doubly fed reluctance machine drives", Eight IEE *International Conference on Power Electronics and Variable Speed Drives (PEVD'2000)*, London, UK, 18-20 September 2000.
80. M.Jovanovic and R.E.Betz, "Brushless doubly fed reluctance machines – a cost effective solution for limited speed range applications", *International Conference on Electrical Machines (ICEM'2000)*, Espoo, Finland, 28-30 August 2000.
81. M.Jovanovic and R.E.Betz, "Control Strategies for Brushless Doubly Fed Reluctance Machines", Proceedings of the *International Power Electronics Conference (IPEC)*, Tokyo, Japan, April 3-7, 2000.
82. M.Jovanovic and R.E.Betz, "Optimal Performance of Brushless Doubly-Fed Reluctance Machines", *IEE Electrical Machines and Drives (EMD'99) Conference*, Canterbury, UK, September 1999.
83. R.E.Betz and M.Jovanovic, "Control aspects of brushless doubly fed reluctance machines", *European Power Electronics (EPE'99) Conference*, Lausanne, Switzerland, September 1999.
84. R.E.Betz, M.Jovanovic, R.Lagerquist and T.J.E.Miller, "Aspects of the Control of Synchronous Reluctance Machines Including Saturation and Iron Losses", *IEEE-IAS Annual Meeting*, Houston, Texas, October 1992.
85. M.Jovanovic, J.Milanovic and D.Petrovic, "Frequency Converter Starting a Self Controlled Synchronous Motor", *International Conference on the Evolution and Modern Aspects of Synchronous Machines*, Zurich, Switzerland, August 1991.
86. R.D.Lorenz, K. W. Van Patten, High –Resolution Velocity Estimation for All-Digial , ac Servo Drives, IEEE *trans. on ISA, Vol. 27, NO.4*, July, 1991
87. M.P.Kazmierkowski and H.Tunia, "Automatic control of converter-fed drives", Elsevier, 1994. ISBN 0-444-98660-X
88. Erich Hau, Wind Turbines: Fundamentals, Technologies, Application, Economics, ISBN 3-540-57064-0, Springers,2000
89. Robert Harrison, Erich Hau and Herman Snel, Large Wind Turbines Design and Economics, ISBN 0-471-49456-9, John Wiley & Sons Ltd, 2000
90. P.Krause, Analysis of Electrical Machines, McGill Hill,1986
91. S.Arnalte, J.C.Burgos, J.L. Rodoriguez, Direct Torque Control of a Doubly-Fed Induction Generator for Variable Speed Wind Turbines, Electric Power Components and Systems, 30: 199-216, 2002
92. M.Jovanovic, J.Yu and E.Levi, "Real-time implementation of direct torque control

scheme for Brushless Doubly Fed Reluctance Motors", 2nd int. conf. On Power Electronics, Machines and Drives (PEMD), Edinburgh, 2004

93. J.Yu and M.Jovanovic, "A switching strategy for direct torque control of brushless doubly-fed reluctance motors", the 38th *Universities Power Engineering Conference (UPEC)*, Thessaloniki, Greece, September 2003.
94. M.Jovanovic and J.Yu, "Maximum efficiency control of brushless doubly-fed reluctance motors for large pump applications", 3rd *International Conference on Energy Efficiency in Motor Driven Systems (EEMODS)*, Treviso, Italy, September 2002.
95. M.Jovanovic, J.Yu and E.Levi, "Direct torque and flux control of brushless doubly-fed reluctance motors", the *European Power Electronics (EPE) conference* in Toulouse, France, September 2003.
96. M.Jovanovic, J.Yu and E.Levi, "A doubly-fed reluctance motor drive with sensorless direct torque control", IEEE *International Electric Machines and Drives Conference (IEMDC)* in Madison, Wisconsin, June 2003.

Appendix A

Components Introductions and Tests

Due to the contents limitation, the detailed introductions of experimental components are listed in this part. This appendix tried to be in such a way that some detailed test records were included for the future reference. BDFRM, transducers and IGBT units were tested. The offline test is to get the accurate machine parameters such as resistance and inductance. It can be found that the inductance varies with the rotor position. However this variation is within the small area. It is still valid to treat the inductance a constant. The final parameters were listed in A. 1. Accuracy of transducers and their working performance were listed in A. 2, the test was to simulate transducer performance in the actual working condition. The transducers were proven to be precise and no phase shift. The main features of the IGBT inverter unit can be referred to the user manual. Some general introduction which will help to carry out the tests and understand the results were included in this appendix. The test for IGBT system including a signal amplifier interface can be found in A.3. A.4 was used to introduce the torque transducer that would be used to monitor the speed and torque along shaft.

A.1. MACHINE OFFLINE TESTS

The doubly feed reluctance machine is characterised by its special stator design. When it turns to the rotor, there is no difference between BDFRM than the rotor of its counterparts such as synchronous reluctance machine. The rotor has different inductances along its dq axes(L_d and L_q). In its simplest salient form, it is similar to the classical machines without a rotor winding. The electromagnetic torque is developed due to the tendency of the rotor to take up a minimum reluctance position for the stator flux. This is the position when the high permeance rotor axis (d-axis) is aligned with the stator field axis.

A.1.1 THE STATOR RESISTANCE TEST

It is difficult to get directly the value of phase resistance since the neutral point is inside of the machine and not accessible. However there is a simple way to test. If the terminal of B and C are connected the circuit will be like:

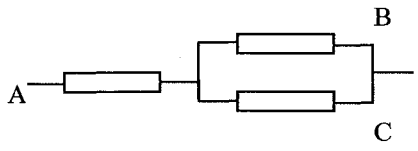

Since three phases are symmetric to each other, the resistance got will be 1.5 times of per phase. The same was done to the other phase and the results were listed as following:

Primary side

A, BC	16Ω
AB,C	15.98Ω
AC,B	16.22Ω

Secondary side

a, bc	19.15Ω
ab,c	18.73Ω
ac,b	19.20Ω

Therefore the resistance of per-phace will be:

$$R_{phase} = \frac{2}{3} R_{reading}$$

$$R_p = R_{ave} = \frac{1}{3}[\frac{2}{3}(16+15.98+16.22)] = 10.71(\ \Omega)$$

$$R_s = R_{ave} = \frac{1}{3}[\frac{2}{3}(19.15+18.73+19.20)] = 12.684(\Omega)$$

A.1.2 INDUCTANCE TEST

The assumption of inductance test:

1. the three phase-inductance are symmetrical
2. the three-phase supply are symmetrical
3. the resistance value will keep constant even the temperature changes according to the condition

When the line voltage is fully supplied as 415V, it is hoped that the inductance tested is under saturation condition. It will be much closer to the actual value when the machine is running. The periphery condition is that the rotor is kept standstill by brakes while the readings are made.

This test was based on the equivalent circuit (Chapter 3). If the 2q-pole winding is open circuited and the 2p pole winding is supplied with symmetrical three phases ac power, it is seen that the self-inductance L_p and mutual inductance L_{ps} can be determined by:

$$L_p = \sqrt{\left(\frac{U_p}{I_p}\right)^2 - (R_p)^2} / \omega_p \qquad \text{(A. 1)}$$

$$L_{ps} = \left(\frac{U_{q0}}{I_p}\right) / \omega_p \qquad \text{(A. 2)}$$

where U_p and I_p are the phase voltage and current applied to the 2p- pole winding, and U_{q0} is the measured open-circuit phase voltage of the 2q-pole winding. In a similar way, the self-inductance L_s can be tested.

It should be noted that the self-inductance and mutual inductance are dependent on the rotor position. Therefore, the above test procedure should be carried out for different rotor positions. In order to obtain accurate test results, not only the voltage and current of the windings, but also the rotor position angle should be carefully recorded.

The readings were recorded at different voltage levels and different positions. At each position, there is an average value of the inductance. It can be calculated that the primary inductance is : 0.4069 H. The same strategy is used to test the secondary inductance and the value is 1.256 H. The mutual flux is measured as 0.57 H. It can be seen that the values of inductance is changing with position, however, the change of inductance is quite small (less than 10%).

A.1.3 PARAMETERS USED IN THE EXPERIMENT

The off-line tested parameters which will be used in the experiment controller are listed as :

Rated Power : 1.5 kW;

Rated Voltage: 415 V;

Primary resistance: 10.7 ohms;

Primary inductance: 0.4069 H;

Secondary resistance: 12.684 ohms;

Secondary inductance: 1.256 H;

Mutual inductance: 0.57 H;

Pole numbers of Rotor: 4

It has been aware that more can be done in machine optimal design. Some of the plots in the thesis were generated on parameters from paper [22] because the prototype machine was not available and tested until the last stage. The parameters in paper [22] were for a 2 horse-power BDFRM:

Rated Power : 2 Hp;

Primary Rated Voltage: 220 V; Primary Rated Current: 4.5 A;

Primary resistance: 0.4 ohms;

Primary inductance: 0.06 H;

Secondary resistance: 0.32 ohms;

Secondary inductance: 0.06 H;

Mutual inductance: 0.03 H;

Pole numbers of Rotor: 4

A. 2. VOLTAGE TRANSDUCER TEST

A.2.1 THE TEST OF VOLTAGE TRANSDUCER

The aim of the test: 1. To check the accuracy of voltage transducer;

2. To check the phase-shift problem of voltage transducer

The devices used in the test included:

- $\pm 15V$ DC power supply; variable AC single phase supply;
- Oscilloscope; resistors: one is labelled 33 $K\Omega$, another is labelled 220 Ω
- Voltage transducer: to be used as the interface between oscilloscope and measurement terminal;

From the data sheet of voltage transducer ***LEM LV 25-P***, it can be seen that the transducer can be powered up either by $\pm 10V$ or a $\pm 15V$ DC supply. Rated input current is 10 mA while the rated output (measurement terminal) current is 25 mA. Since the ADC limitation of the dSPACE board is 10 Volts, the measurement resist

should be not exceeding than 400 Ω.

e rated calculated power on it is just 0.25 w.

Since the voltage transducer work in the rated 240 volts phase voltage, the performance around this voltage rating is more interested. In that test, a $22\,K\Omega$ input current limiting resistor was chosen. Therefore, in theory, the 220 volts input voltage will corresponding the 10 mA current.

A.2.2 TESTS OF CURRENT TRANSDUCER

The current transducer used in the actual experiment is : HY5-P *LEM* current transducer. The nominal primary current 0-5A, the accuracy is less than 1 % from the Data Sheet. Power supply used is 15 V and the maximum output voltage is 4V.

To work out the corresponding conversion formula and confirm the technical values on Data Sheet, the test on transducer was carried out.

The DC power supply has the limitation of 2.0 A and 30 V. digital current metres used in the test was limited 5mA tolerance(have been tested). A variable resistance was chosen to achieve the different current.

The expected relationship between input current and out voltage should be

$$\frac{I}{V} = \pm\frac{5}{4}$$

since the maximum values of the output voltage is 4 v and the maximum input current

is 5 A. the supply of the transducer was using $\pm 15v$ since the transducer would be used for AC current measurement.

The average value of the ratio is 1.244. This value will be used in the software transformation. The difference between the expected value 1.2 and the actual value might attribute to the tolerance of meters, human errors, the resistance of wires and offset. There was an offset. The way to detected the offset was to short-circuited DC voltage source. It was found that there was a reading around 2mA. The accuracy calculated was 0.5%, which was consistent with the data sheet.

A.3. IGBT INVERTER: SKIIP SYSTEM

The IGBT inverter used in the experiment system is : **Skiip 132GDL120-412CTVU**. This is a comprehensive product of ***Semikron,*** Germany. As the names suggests, this AC-AC inverter unit is an intelligent integrated semiconductor subsystem. It is rated at 100A, 412V working condition. Three-phase full-bridge(6 pack) IGBT units is combined with the DC brake chopper. With embedded three phases close loop current sensors, DC-link voltage sensor, the unit has an integrated 15/24 V power supply as well as an temperature sensor. Normalized analogue voltage signals of the actual Ac-current value, the actual ceramic substrate temperature value and the actual DC-link voltage are available at the DIN41651 gate driver connector of the **Skiip**

system for use in the control system. These voltage signals are smaller than 10 V which is the limitation of **dSPACE 1103**. Therefore, these two systems can be integrated easily. The rectifier used in the DC bridge is SKKD 46/14. The reference values are as following: $I_{FRMS} = 90A,$ $V_{RSM} = 1500v$ $V_{RRM} = 1400v$

The EMC capacitor(S1000202) is used for the high frequency filter.Four capacitors ($4400\mu F$) are used for DC bridge. The two-serious and two-parallel connected capacitors have the overall rated voltage at 800 v since each is rated at 400v. The capacitor is the EMC one which is suitable for high switching frequency. There is a discharging resistor parallel connected with each capacitor.

A.3.3 THE TEST OF THE EMBEDDED DC VOLTAGE TRANSDUCER

To protect the device, there is a DC voltage transducer built in to monitor the condition of DC bridge. This sensor, together with over-temperature and over current protection makes sure that the Skiip 2 system is in the working condition. From the data sheet, the corresponding relationship between the actual value and the sensor output signal should be

$9_{output}(V)$ $900_{DC\,link}(V)$

that means the maximum voltage value of DC link is 900 volts which is corresponding to 9 volts output signal. Therefore, there is 100:1 ratio. This is within the safe range of dSPACE board since the rated I/O signal is rated within 10 volts.

A test was done to check this. A variable transformer is used. The transformer has an output 150 volts, the value of 1.5 volts is expected. To minimise the influence of noise, a shielded cable is used which has a grounded wire along with the signal output. Figure A. 2 still had the visible ripples. The maximum err of this signal is 13% (0.2 volts in 1.5 volts output). This ripples were assumed to come from the transformer (source) since the Figure A. 2 demonstrated same ripple in wave form. Channel 1 in Figure A. 2 was for one phase input AC voltage while Channel 4. was to show output DC signal.

If the transformer sets the output as 150 volts (phase- neutral), the DC link voltage is expected as 350.86 volts, by using the formula $V_{DC} = \frac{3\sqrt{6}V_{phase}}{\pi}$. The voltage meter reading of the DC link is 355.12 volts while the reading of the oscilloscope is 3.5 volts .

This test (Figure A. 1) examined both the ability of DC link and voltage transducer. The error of voltage transducer out put is 1.2% that attributes to DC link as well as the tolerance of voltage transducer.

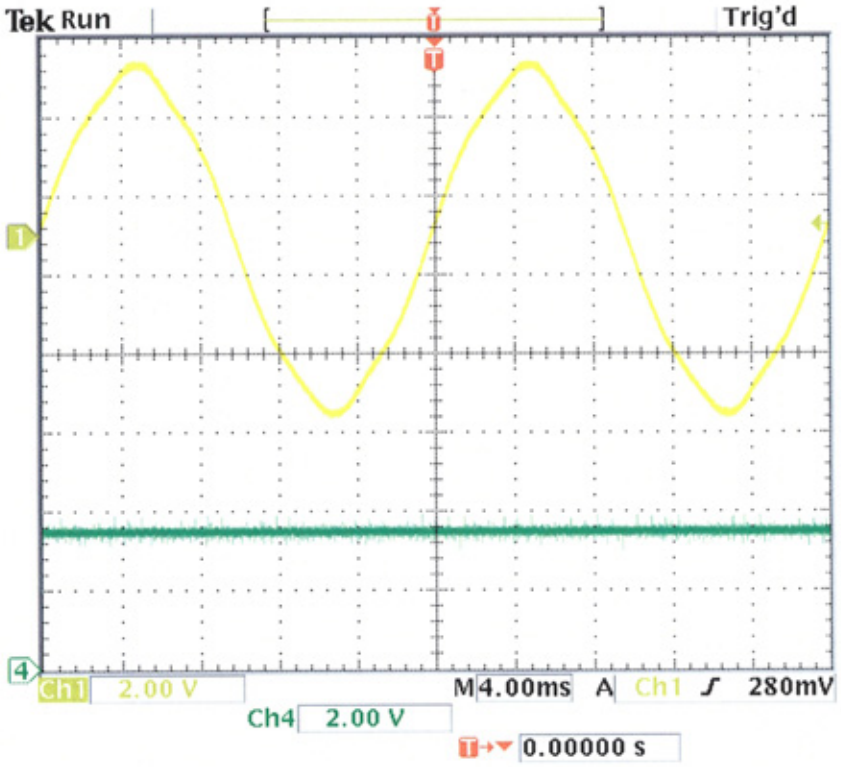

Figure A. 1 the DC sensor shows the correct value corresponding to maximum output of the transformer

Further test is done to examine the influence of noisy signal on dSPACE I/O board. The two plots in Figure A. 2 and Figure A. 3 showed the oscilloscope output which was for the case DC link voltage is 211 volts. To comparison, the output of dSPACE control desk was plotted. The dSPACE plot was yielded in the condition of step size: 0.1ms (which is 10kHz) measure period.

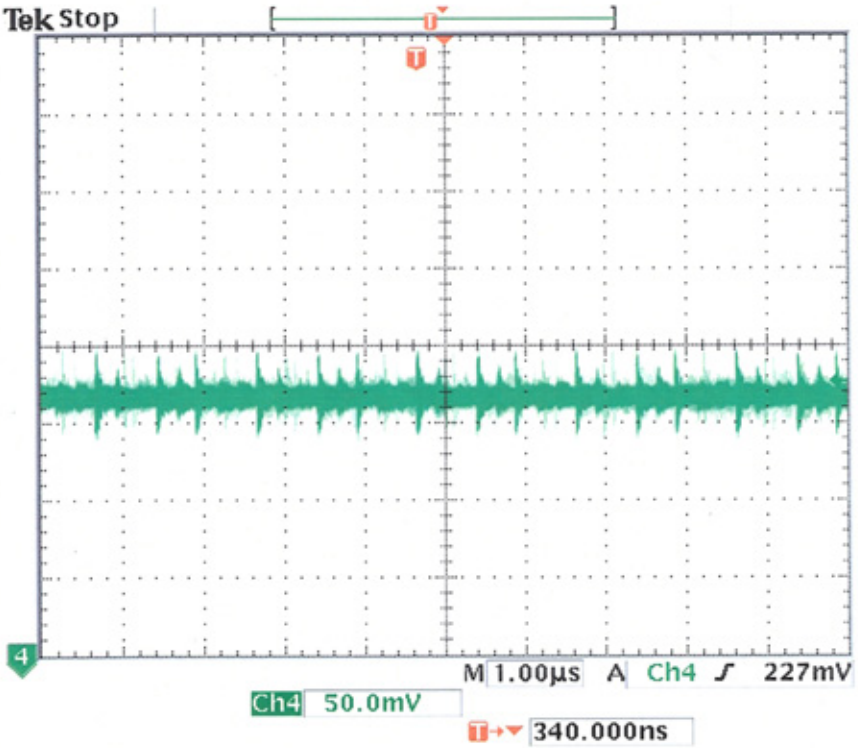

Figure A. 2 the oscilloscope plot of the DC link voltage sensor output (215v)

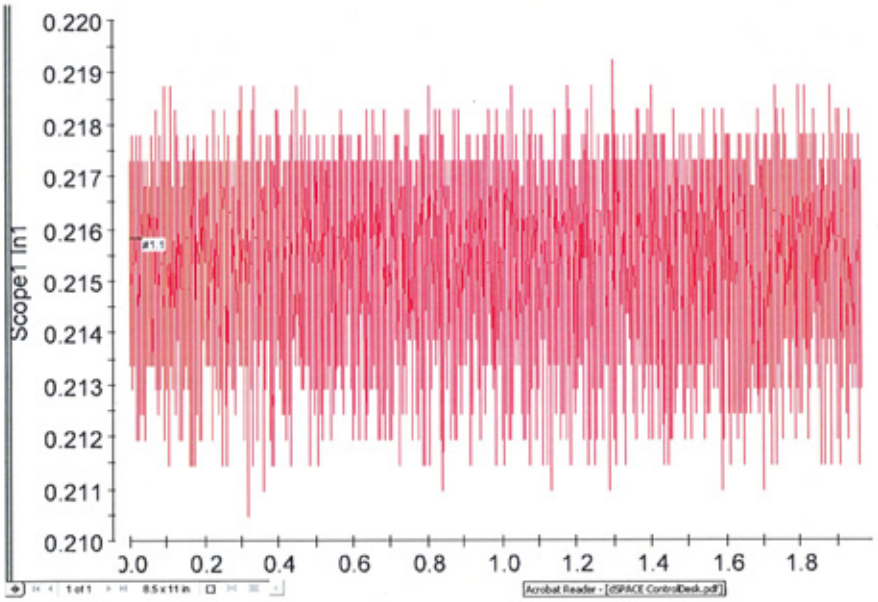

Figure A. 3 the dSAPCE control desk plot (215 v)

A.3.4. TESTS OF INVERTERS

Signals from dSPACE I/O board are designed as Terminal Logic (TTL) signal. The voltage comparator is used as an amplifier to transfer the TTL (5v) signal from dPSACE to a 15 v CMOS signal. Both chip LM 741 and the chip of LM311 are tested. LM 311 will be used in final hardware experiment due to its fast response.

The plot of Figure A. 4 showed the instant amplifier signal corresponding to the TTL input by using LM331. The voltage output is shown as well. In the plot, channel one is the amplified signal whose amplitude is 15 volts, while channel 2 is the TTL signal from the controller. Since this test is only applied to single module, the high voltage (15 volts) status will turn on the IGBT. The characteristics of IGBT (turn of delay time around 2 μs) can be clearly seen from the plot(channel 4).

Figure A. 5 shows the voltage output together with CMOS signals in the case of two-phase connection. One phase is controlled by a 5 KHz signal (Channel one) while the other one is controlled by 2.5 KHz signal(Channel 3). Channel 2 is the output of err detection of phase currents. The function of this protection is to prevent two modules in one leg being switched on at the same time. This function is achieved by setting this error signal high. There is 'dead-time' design embedded in the Skiip system, therefore, it is possible to use inverse function to control one phase leg.

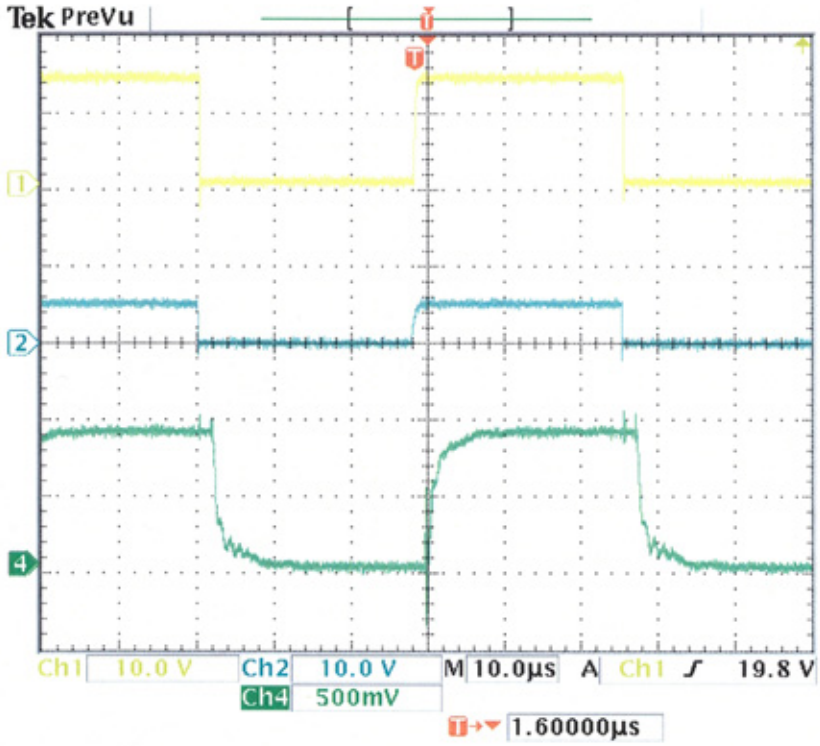

Figure A. 4 test via LM331.From top to bottom: amplified CMOS signal; TTL signal and the voltage ouput

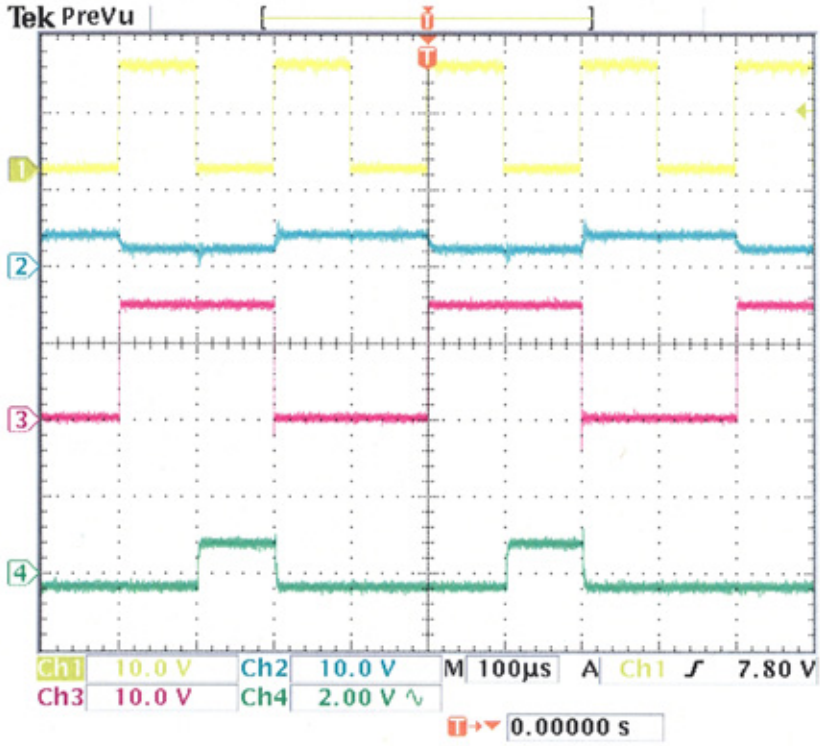

Figure A. 5 the two phase connection

before they were used in assembly system. The details parameters of machine were listed through offline test. The inductance dependence on rotor position was considered. Other tests examined the qualify and accuracy together with interface A/D converters of dSPACE board. These tests proved that the chosen devices were suitable for the real time implementation and paved the way of system control in later stage.

Appendix B

DS1103: Introduction and Tests

More detailed information about DS1103 board, dSAPCE® used in the real time experiment can be referred to DS 1103 board user manual. The general introduction was outlined and important tests were done to identify the appropriate techniques for encoder signal process in the real time control system.

B.1 MASTER PPC

The master processor on the DS1103 is a Power PC PPC604e which is running at 400MHz (CPU clock).

B.2 PERIPHERAL UNIT

The following topics provide information on the features provided by the peripheral unit of the PPC:

- ADC Unit
- Bit I/O Unit
- DAC Unit
- Incremental Encoder Interface
- Serial Interface
- Interrupts
- Timers

B.3. The Choose of Encoder Interface

It has been aware that there are two supplied interfaces at dSPACE system: one is RTI encoder interface, the other is DSP F2D block at Slave Processor Interface. The plot Figure B.1 shows the difference between these two options. The top plot is from the output of RTI encoder interface (ENC) , the bottom one is from the Slave Processor Interface DSP F2D block. The step size is quite big at 1e-3 s(which is 1kHz) . There is not much difference between these two plots, the output from encoder output has smoother wave form.

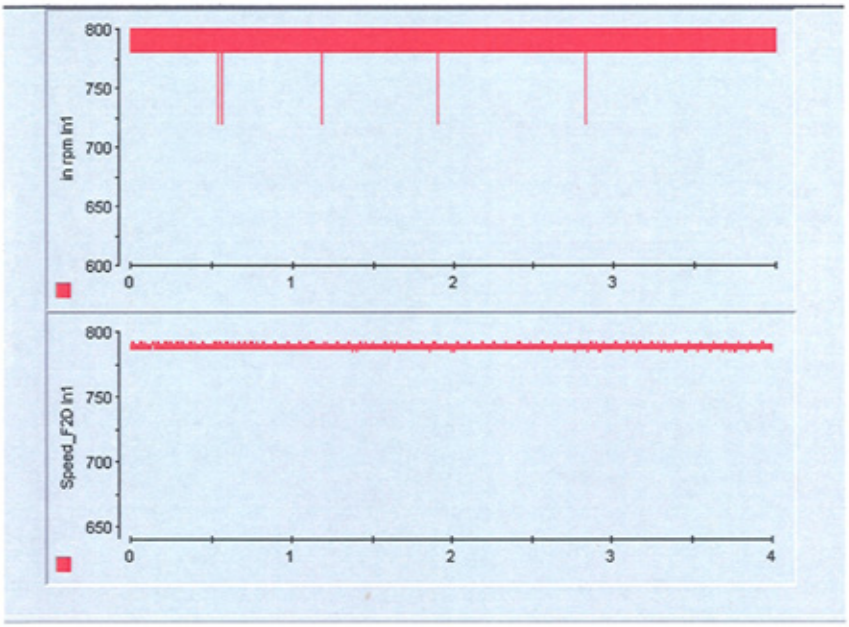

Figure B.1. outputs from two different encoder interfaces

The above plot is yielded in the condition that step size is 5e-5, the transducer reading is 785rpm. It is obvious that the output of F2D has much smaller band and smoother waveform of the speed. It was due to the co-efficiency of covering 'Delta-angle' to speed which is proportional to the sampling frequency.

Because of this low speed of 32.7 lines/msec(corresponding to 785 rpm at 5e-5 s sampling time in the second plot) a small measurement inaccuracy of the used encoder creates an fluctuation between 800 rpm and 770 rpm. Therefore the hysteresis band of 785 rpm +- 15 rpm is caused by the adverse combination of the encoder resolution of 1/4 lines, inaccuracy of the used encoder and a low encoder speed. In comparsion higher encoderspeeds (from about 1000 rpm onwards) would cause an negligible hysteresis band. To solve this problem there are three possibilities:

1. Use an encoder with higher resolution (20000 lines)

2. Enlarge (if possible) the stepsize to 0.01 sec.

3. To calculate the speed use a F2D IO block (DS1103SL_DSP_F2D) instead because of its higher time resolution of 50e-9 sec. For this connect the phi0 or phi90 signal line to connector pin P2 77. Afterwards the F2D output must be transformed as followed: speed in RPM = F2D_output*60/encoder_resolution. To get the direction information of your encoder use DS1103_ENC_POS furthermore.

Therefore, the **conclusion** can be made as followings:

1. The RTI I/O block DS1103_ENC_POS outputs encoder position and delta position in encoder lines.

2. The corresponding encoder resolution is 1/4 lines. To get information like speed in RPM or angle in degree you must transform the ouputs as described in your last mail, for example:

   angle in degree = enc_pos_output/encoder_resolution * 360°

   speed in RPM = enc_delta_pos_output*60/(encoder_resolution * stepsize)

3. in the formula of

$$w(in \quad rpm) = incoder\ output(Delta\ Position) \times \frac{60}{stepsize(s) \times encoder - lines}$$

the value used should be the actual line;

4. the F2D I/O block has better result than the encoder interface but has no information of the direction. The output of F2D block has better waveform compared with output of encoder, especially when sampling frequency is high.

Another techniques to get a smoother speed waveform together with the direction information is to use higher step time in encoder sampling. The Zero-Order Hold block implements a sample-and-hold function operating at the specified sampling rate. By using a Zero-Order Hold block, the band will significantly reduced. The advantage of using a Zero-Order Hold block is to enable 'multi-task' for the simulink model. The following plot was yielded in the condition that ' fix step size ' of control model is still set as 1ms, however, the actual sampling time of the encoder is determined by the Zero-Order Hold block. In this example, the sample time is set as 0.01s which has the very obvious effect on the output.

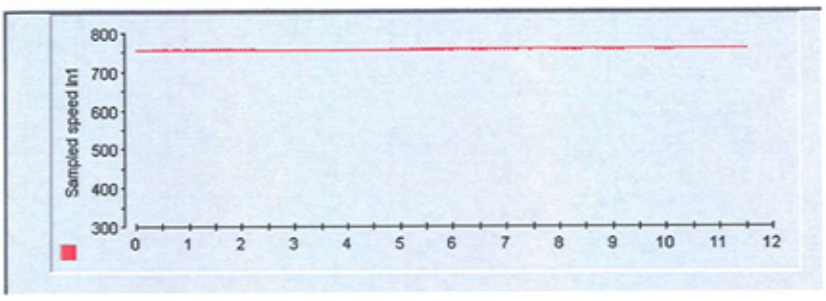

Figure B.2. The encoder signal after Zero-Order Hold block

Appendix C Hardware Pictures

The actual hardware system is presented vividly by pictures in this appendix. It will show in detail what the main components look like, such as the dSAPCE board, Skiip power electronic system, Brushless Doubly Fed Reluctance machine. The picture will show not only each component, but also the whole connected system.

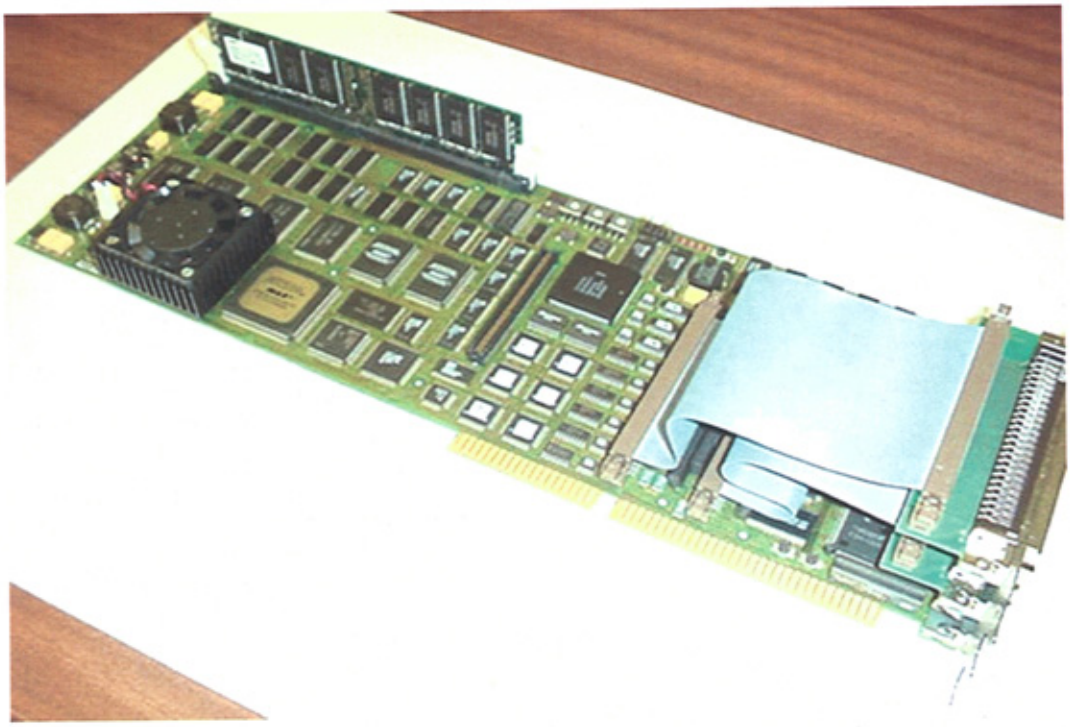

Picture 1:dSPACE board before being installed in PC

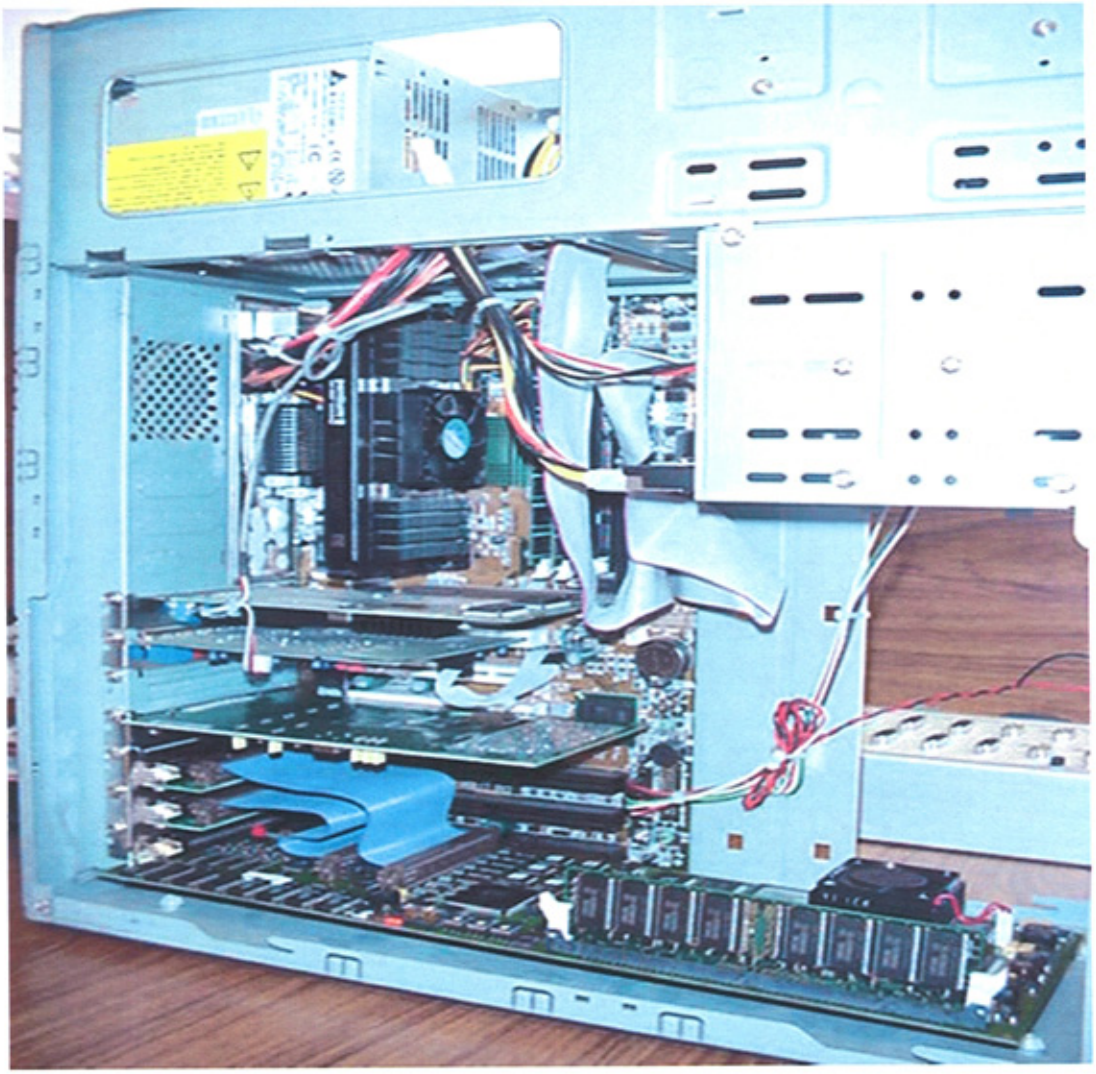

Picture 2: dSAPCE board installed in a PC

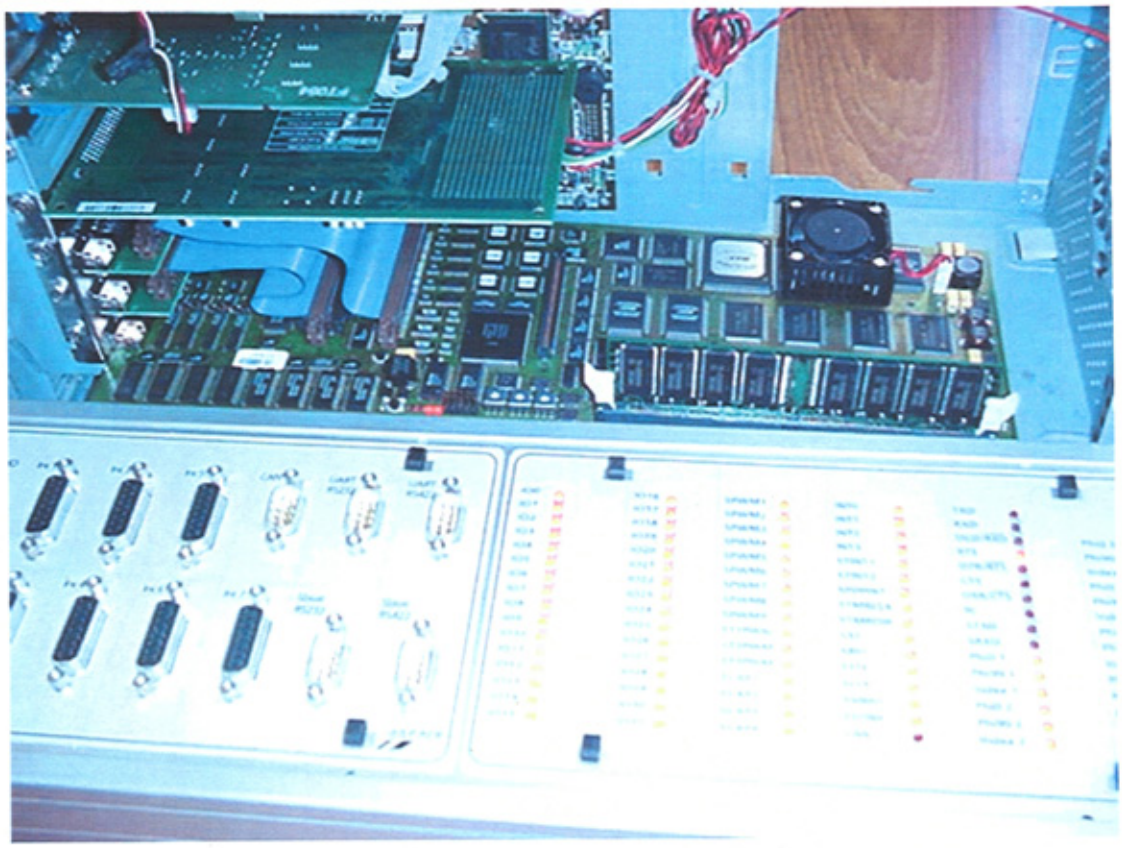

Picture 3: dSPACE® board with connection to a I/O interface board

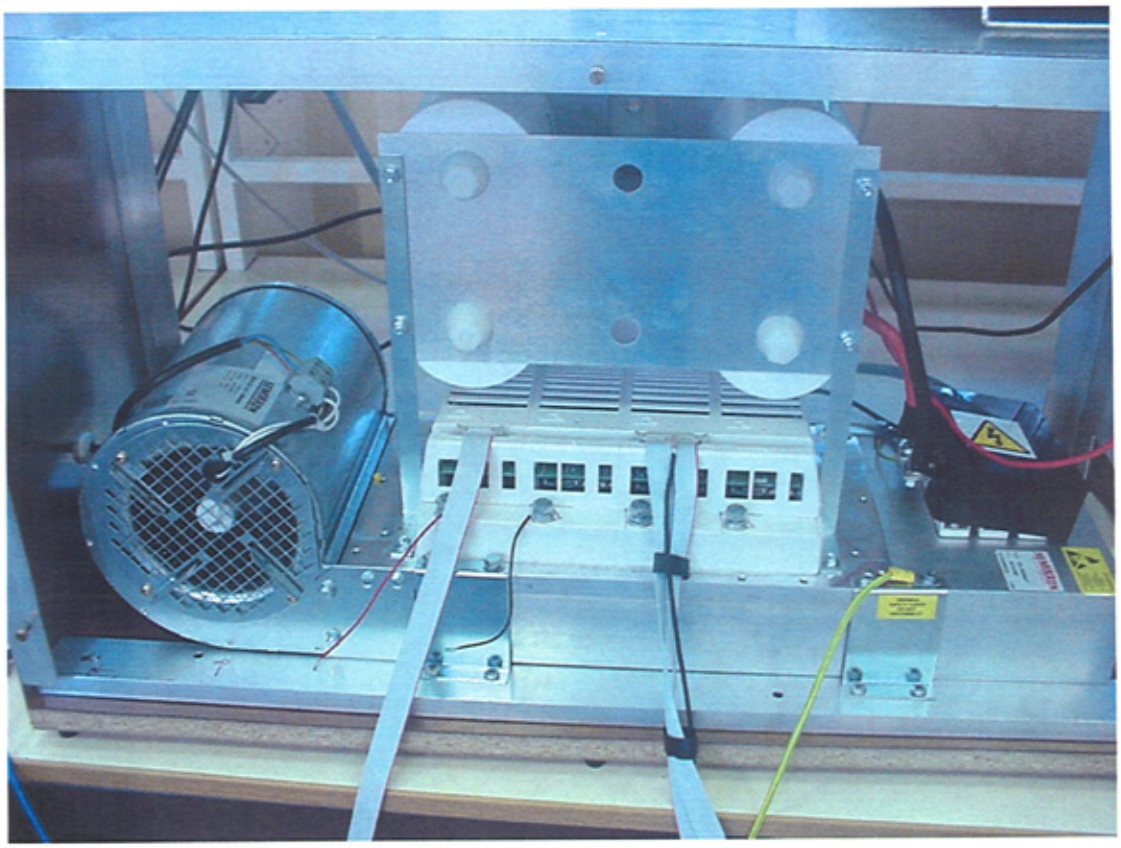

Picture 4: Skiip® power electronic system

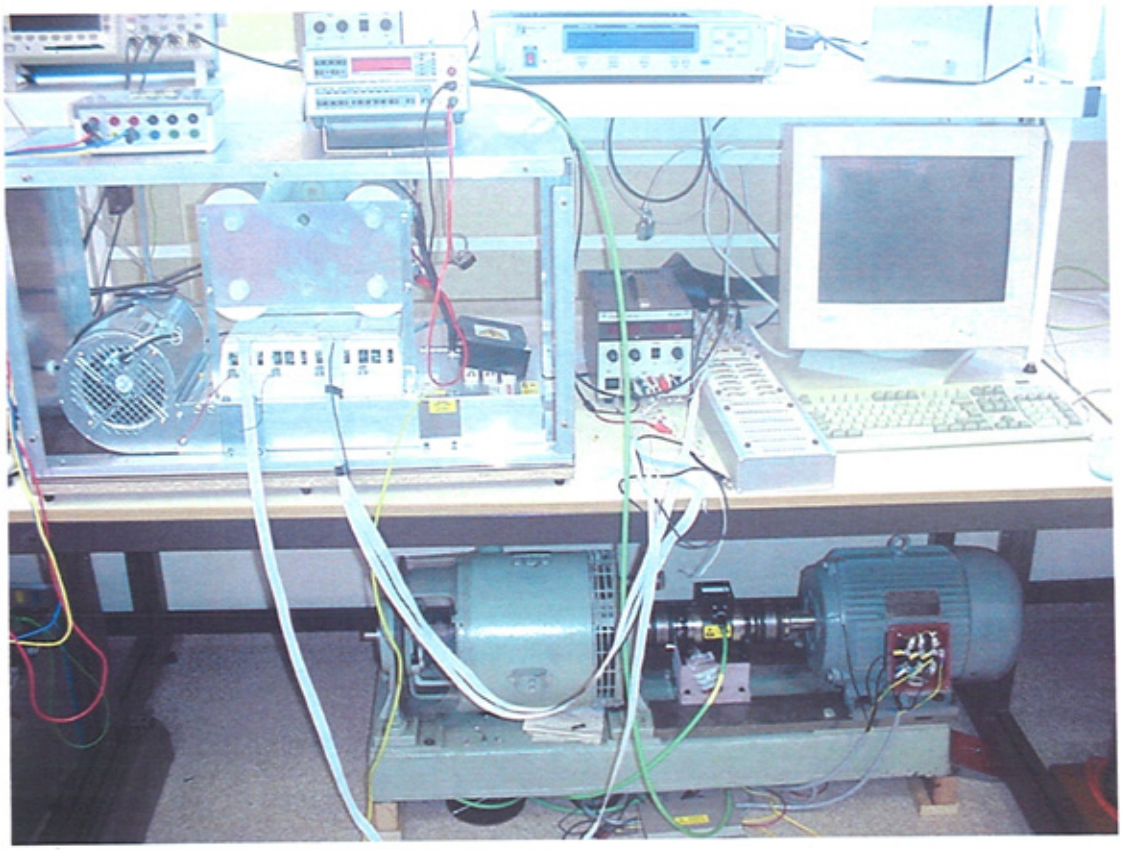

Picture 5: Main part of the connected experiment system

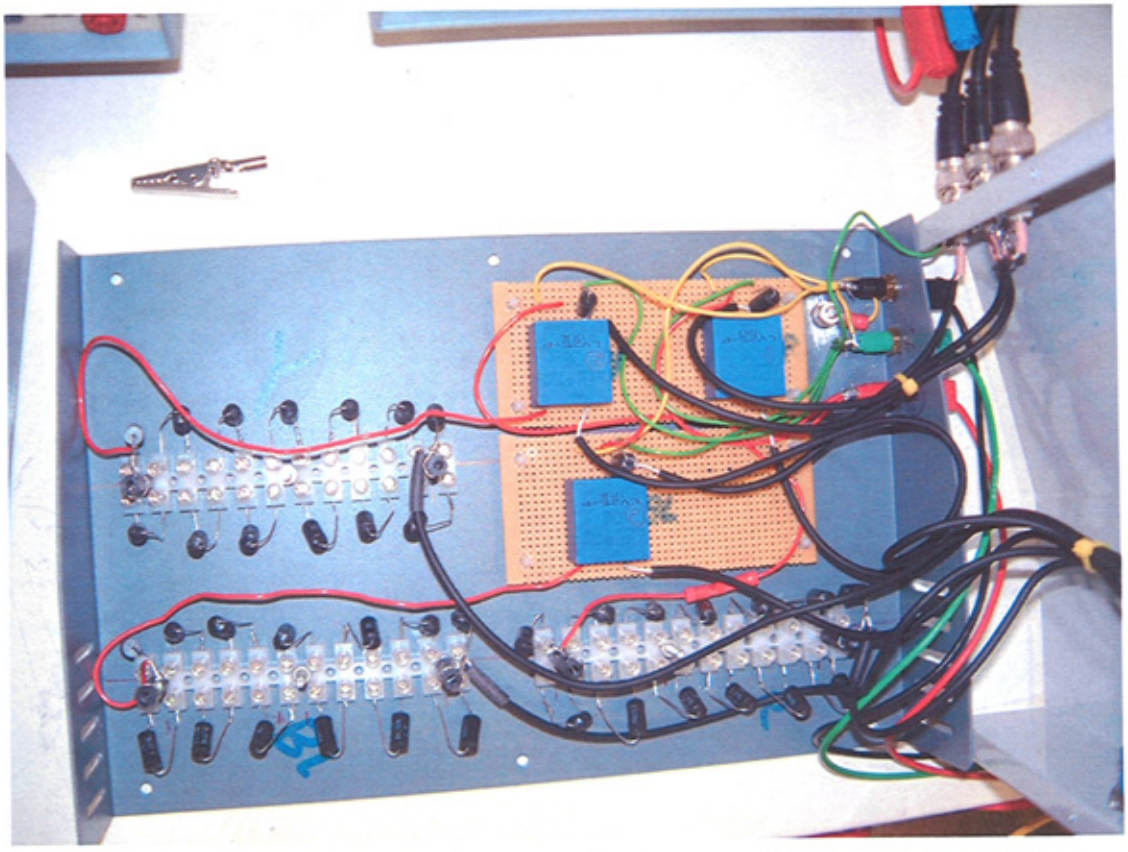

Picture 6: Voltage transducer with serially connected precise resistors

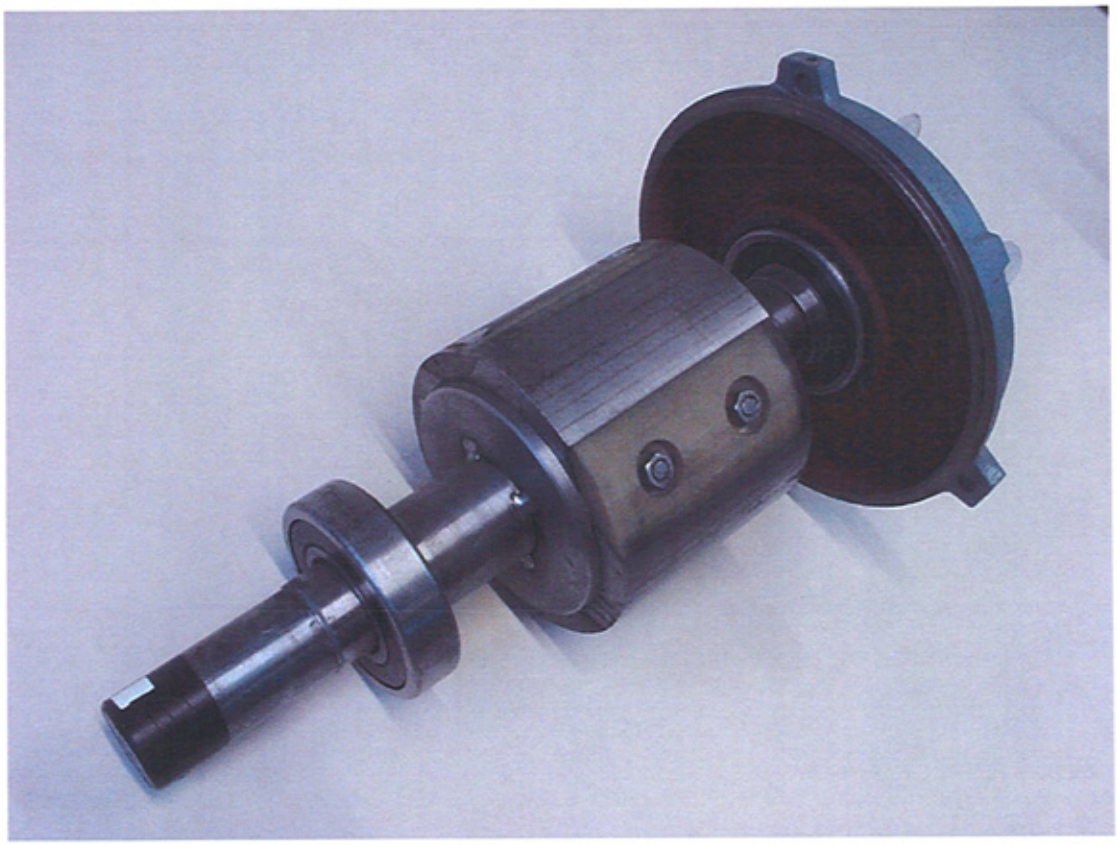

Picture 7: ALA rotor for Brushless doubly fed Reluctance machine

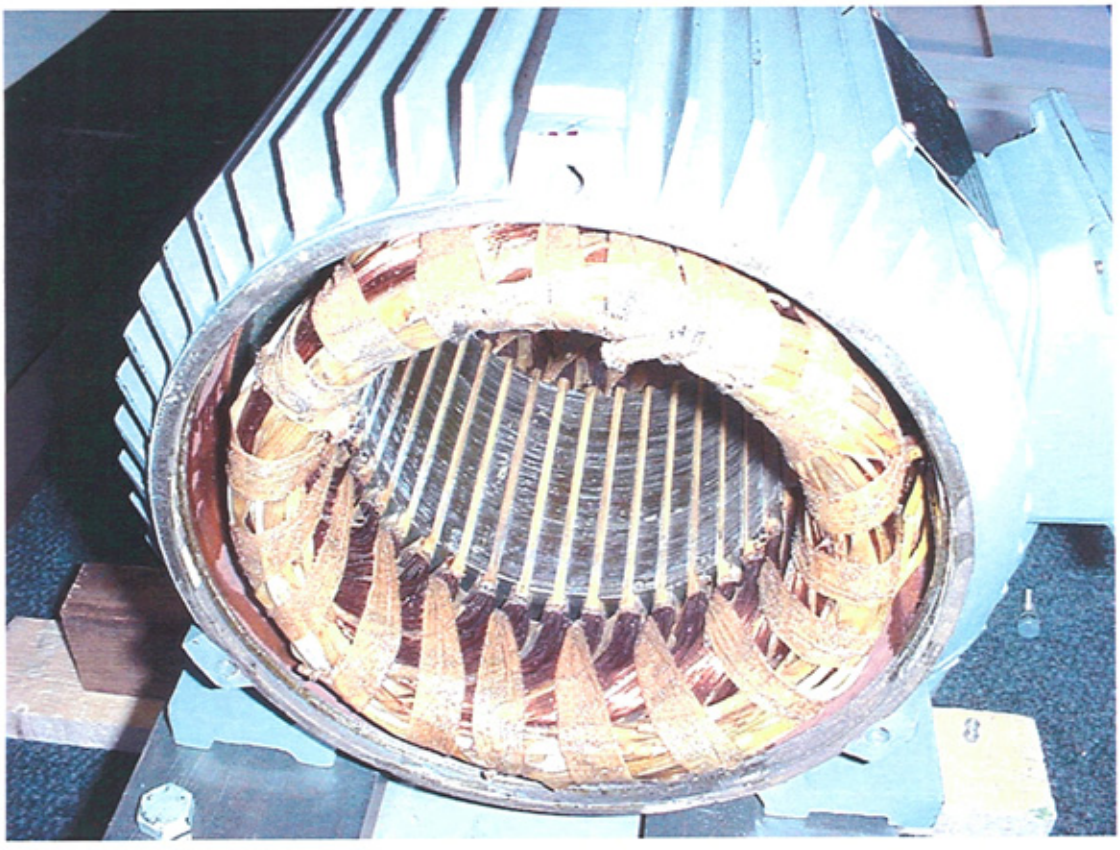

Picture 8: Stator of the machine

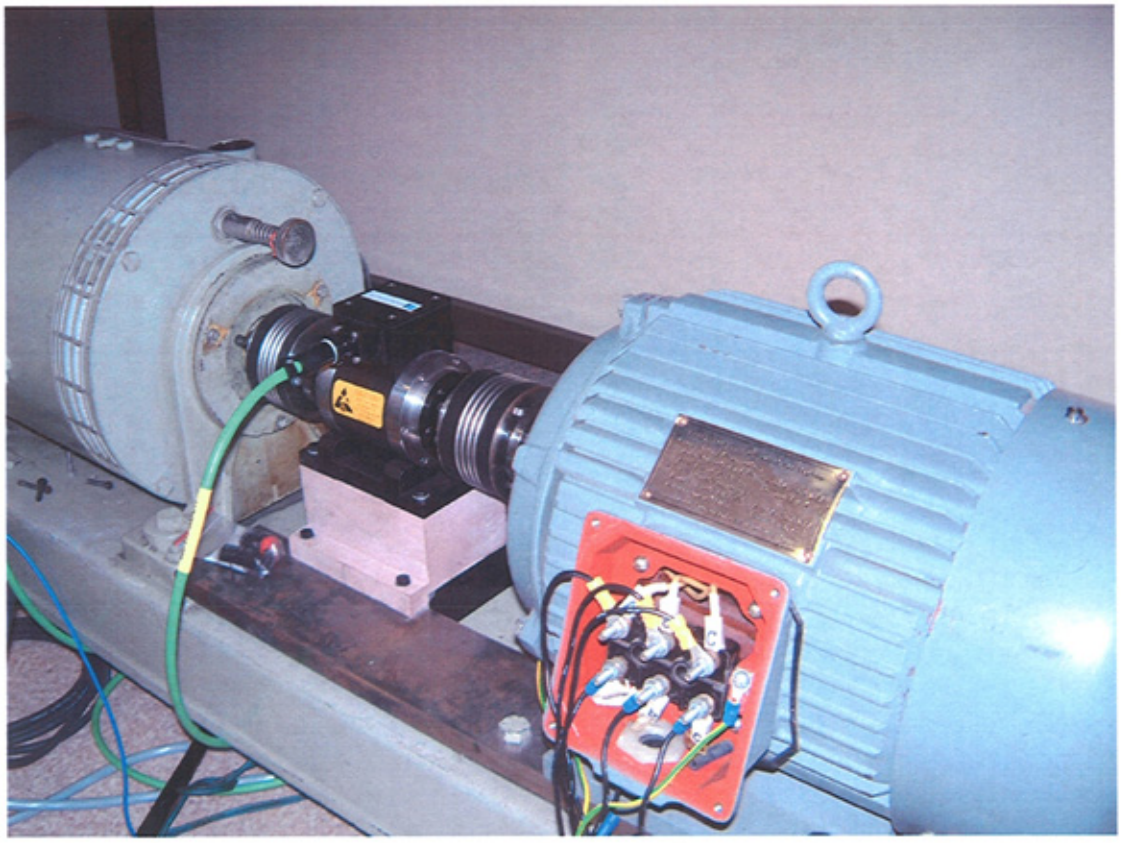

Picture 9: Doubly Fed Reluctance Machine with torque transducer mounted on the shaft

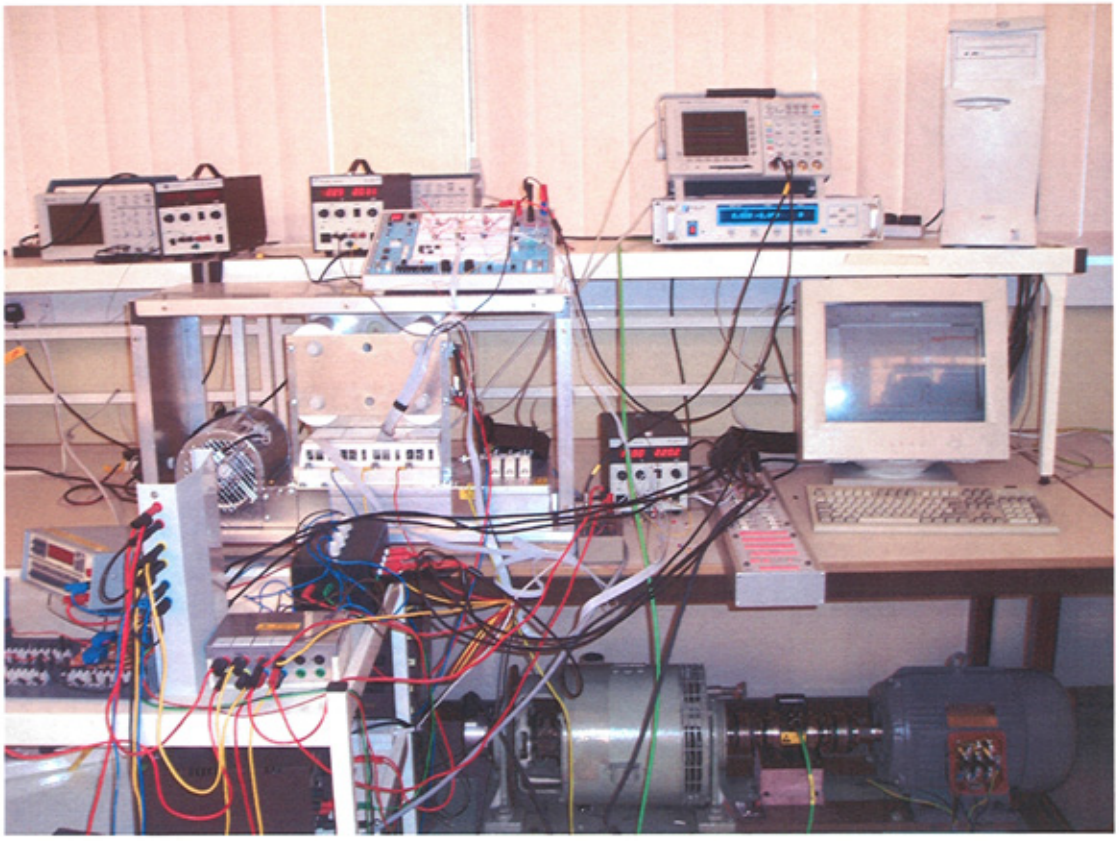

Picture 10: The overall picture of the hardware system

Appendix D Publications

Journal Papers

1. M.Jovanovic, R.E.Betz and J.Yu, "The use of doubly fed reluctance machines for large pumps and wind turbines", *IEEE Transactions on Industry Applications,* Vol.38, No.6, pp.1508-1516, Nov/Dec 2002.

2. M.Jovanovic, J.Yu and E.Levi, "Direct Torque Control of Brushless Doubly-Fed Reluctance Machines", *Electric Power Components and Systems journal*, Vol.32, NO.10, Octorber, 2004,

3. M.Jovanovic, J.Yu and E.Levi, "Sensorless Direct Torque Control of Brushless Doubly-Fed Reluctance Motors", under review for publication in *IEEE Transactions on Energy Conversion.*

Conference Papers

1. J.Yu, M.Jovanovic, " Experiment of Direct Torque Control on Brushless Doubly Fed Reluctance Machine", to be presented at UPEC, Bristal, UK, September 2004

2. M.Jovanovic, J.Yu and E.Levi, "Real-time implementation of direct torque control scheme for Brushless Doubly Fed Reluctance Motors", 2nd int. conf. On Power Electronics, Machines and Drives (PEMD), Edinburgh, 2004

3. M.Jovanovic, J.Yu, " An optimal direct torque control strategy for Brushless Doubly - Fed Reluctance Motors", Power Electronics and Drive Systems(PEDS), Singapore, November, 2003

4. M.Jovanovic, J.Yu and E.Levi, "Direct torque and flux control of brushless doubly-fed reluctance motors", the *European Power Electronics (EPE) conference* in Toulouse, France, September 2003.

5. M.Jovanovic, J.Yu and E.Levi, "A doubly-fed reluctance motor drive with sensorless direct torque control", to be presented at the IEEE *International Electric Machines and Drives Conference (IEMDC)* in Madison, Wisconsin, June 2003.

6. J.Yu and M.Jovanovic, "A switching strategy for direct torque control of brushless doubly-fed reluctance motors", the 38th *Universities Power Engineering Conference (UPEC)*, Thessaloniki, Greece, September 2003.

7. M.Jovanovic and J.Yu, "Maximum efficiency control of brushless doubly-fed reluctance motors for large pump applications", 3rd *International Conference on Energy Efficiency in Motor Driven Systems (EEMODS)*, Treviso, Italy, September 2002.

8. J.Yu, M. Jovanovic and E.Levi, "Simulation of direct torque control of brushless doubly fed reluctance machines", 37th *Universities Power Engineering Conference (UPEC)*, Stafford, UK, September 2002.

9. M.Jovanovic, J.Yu and E.Levi, "Speed control techniques for brushless doubly-fed reluctance machines", 15th *International Conference on Electrical Machines (ICEM)*, Bruges, Belgium, August 2002.

10. M.Jovanovic and J.Yu, "Field oriented and V/f control of brushless doubly-fed reluctance machine drives", *Symposium on Power Electronics, Electrical Drives, Automation & Motion (SPEEDAM)*, Ravello, Italy, June 2002.

11. M.Jovanovic, J.Yu and E.Levi, "A review of control methods for brushless doubly-fed reluctance machines", IEE *Power Electronics Machines and Drives (PEMD) conference*, Bath, April 2002.

12. M.Jovanovic, R.E.Betz, J.Yu and E.Levi, "Aspects of Vector and Scalar Control of Brushless Doubly Fed Reluctance Machines", IEEE *Power Electronics and Drive Systems (PEDS) Conference*, Bali, Indonesia, October 2001.

13. J.Yu and M. Jovanovic, "Scalar control of brushless doubly fed reluctance machines", 36th *Universities Power Engineering Conference (UPEC)*, Swansea, UK, September 2001.

14. J.Yu and J.Finch, "An Alternative Way To The Scalar Control Of Induction Drives", IEEE, 5 th ICEMS, China, August, 2001

15. M.Jovanovic and J.Yu, "An optimal direct torque control strategy for brushless doubly-fed reluctance motors", submitted for *Power Electronics and Drive Systems (PEDS) conference* ,Singapore, November 2003.

speed range including synchronous speed and promising potential for the estimation techniques used in the project.

While both speed and torque are controlled in a feasible way as shown, the flux was not optimal controlled. Control inaccuracies under transient condition are likely due to some problems such as numerical sensitivity of the secondary flux estimator. It is known [43,45,87] that flux reference could be set independently in line with machine's optimal operation condition. This will be further addressed in Chapter 9.

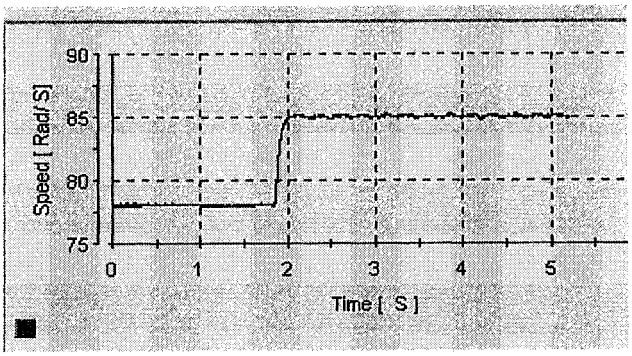

Figure 8.5 Speed plot following a reference to 85 rad/s (super-synchronous speed)

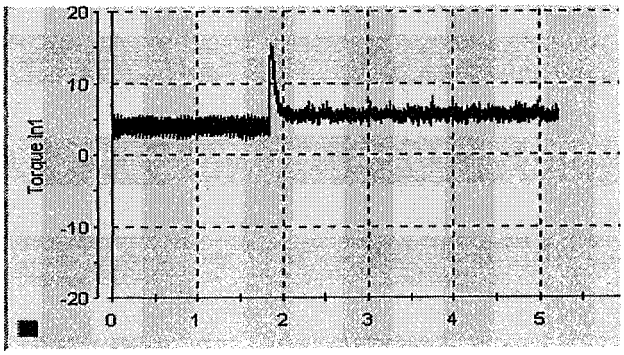

Figure 8.6 Torque response at a speed increment procedure

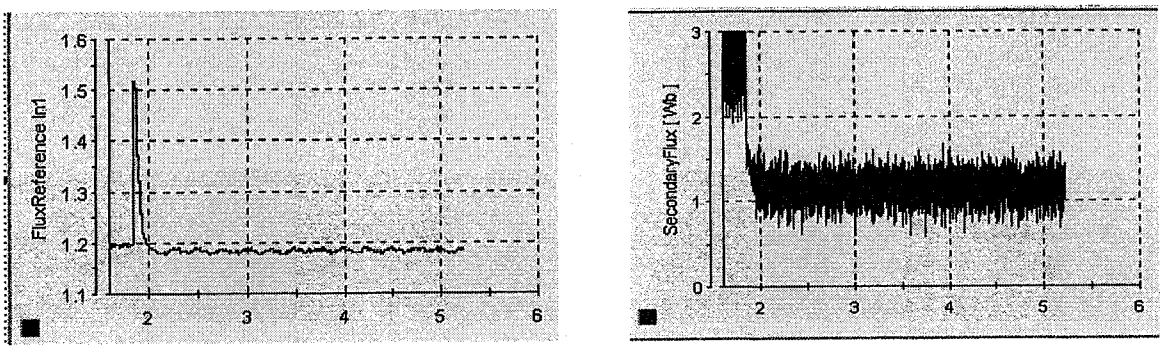

Figure 8.7 The flux control by DTC on BDFRM (start from 1.8 s) left: secondary flux reference; bottom left: secondary flux response

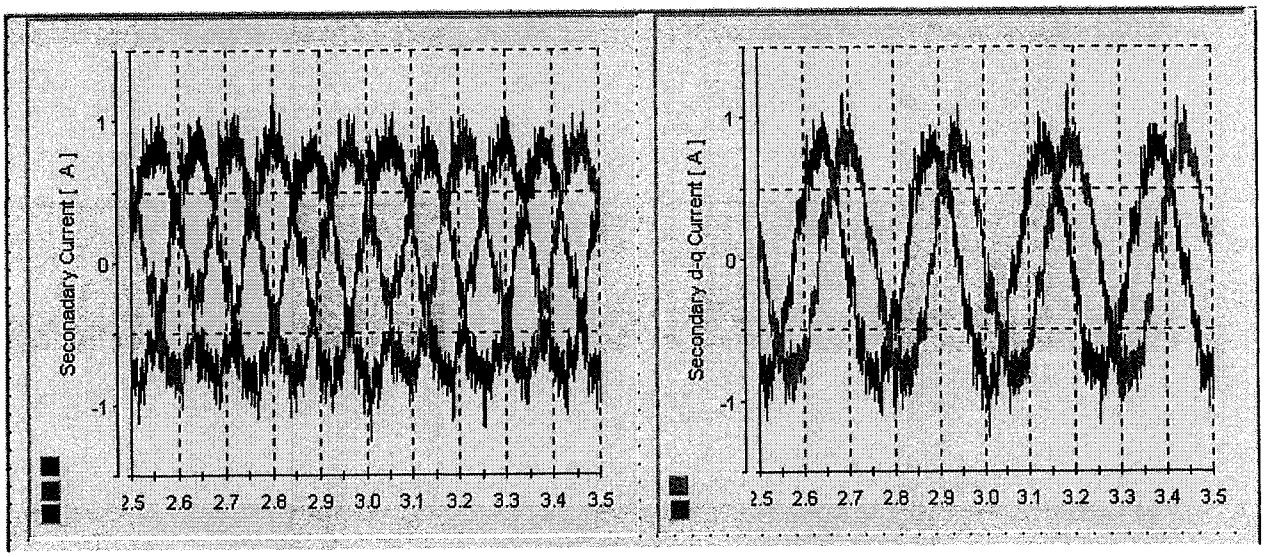

Figure 8.8 The secondary current under control. Left: three-phase currents; right: d-q components of secondary current, d-axis current is in red.

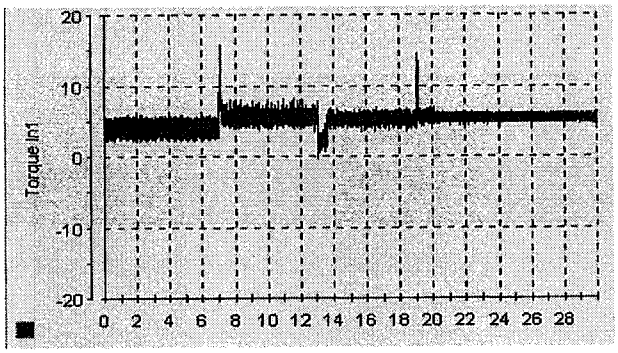

Figure 8.9 Torque response on speed control

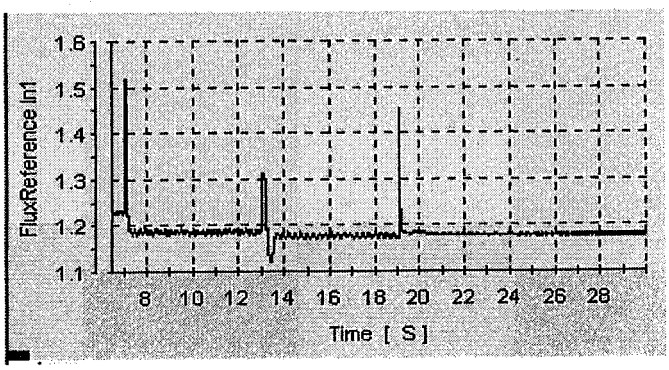

Figure 8.10 reference value for secondary flux

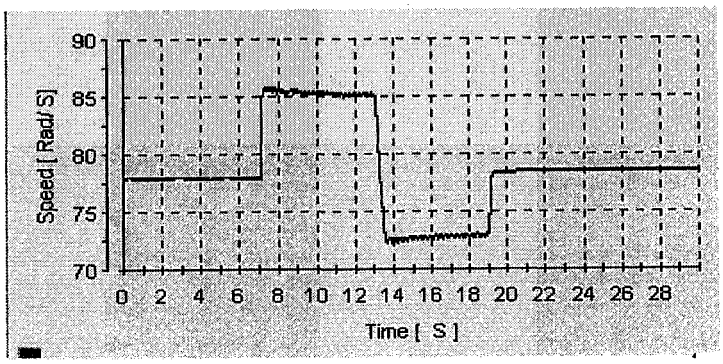

Figure 8.11 the corresponding speed running above, below and at synchronous speed

Figure 8.12 The current in different states

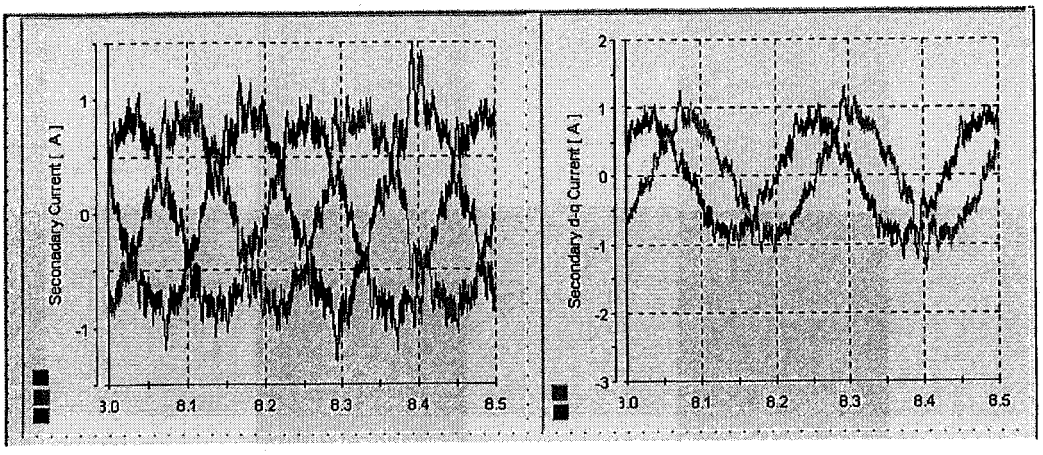

status I: positive secondary current d-axis component is in advance of q-axis component

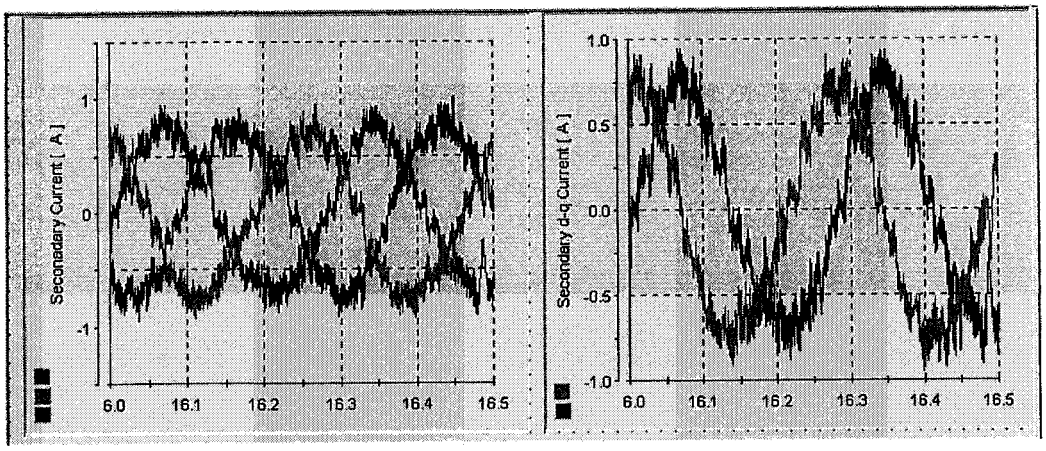

status II: negative secondary frequency when rotor speed is below synchronous speed

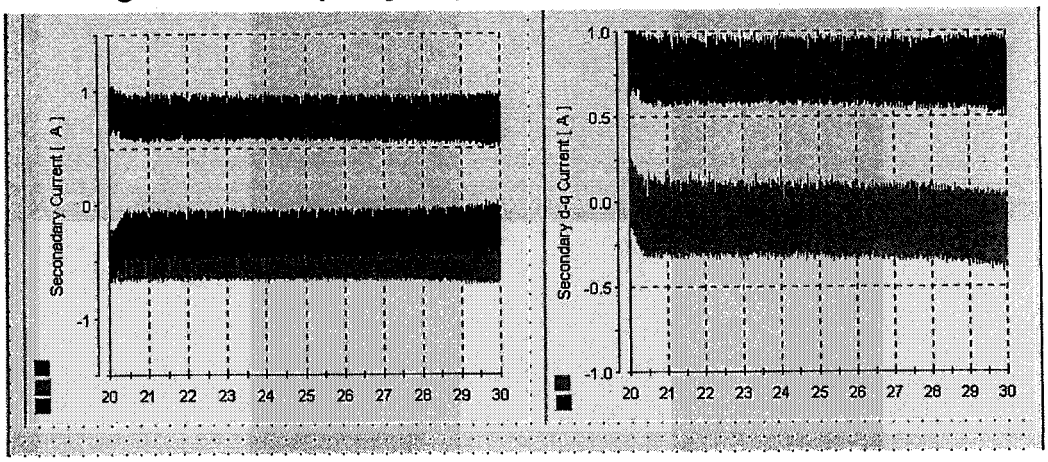

Status III: direct current in secondary when rotor speed is at synchronous speed

speed range including synchronous speed and promising potential for the estimation techniques used in the project.

While both speed and torque are controlled in a feasible way as shown, the flux was not optimal controlled. Control inaccuracies under transient condition are likely due to some problems such as numerical sensitivity of the secondary flux estimator. It is known [43,45,87] that flux reference could be set independently in line with machine's optimal operation condition. This will be further addressed in Chapter 9.

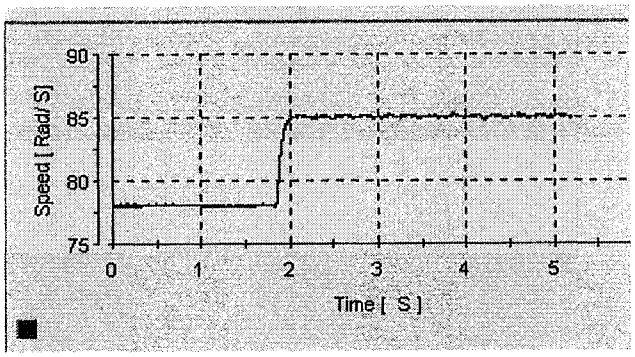

Figure 8.5 Speed plot following a reference to 85 rad/s (super-synchronous speed)

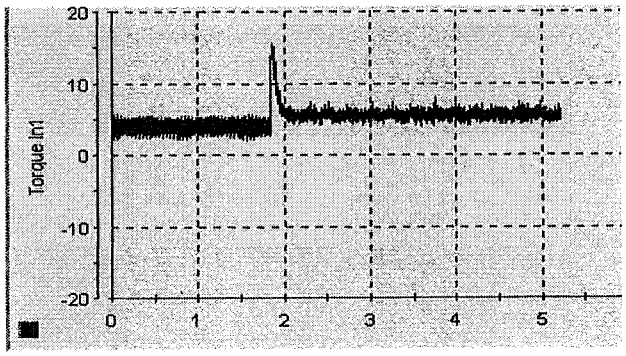

Figure 8.6 Torque response at a speed increment procedure

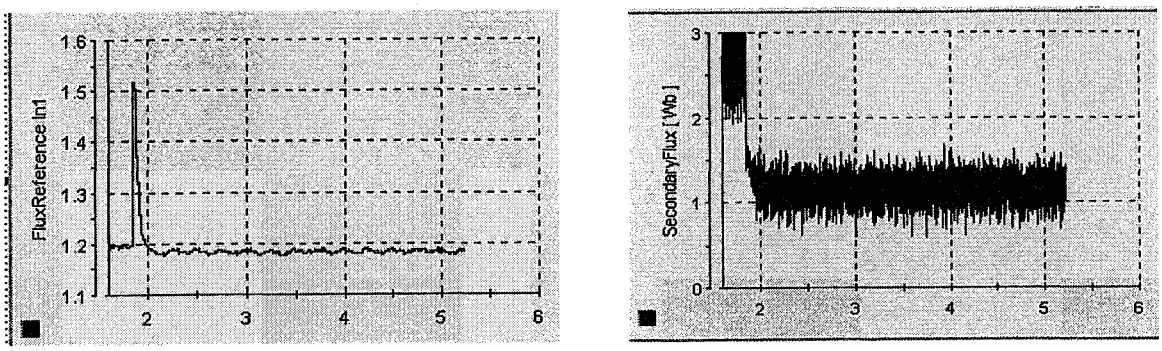

Figure 8.7 The flux control by DTC on BDFRM (start from 1.8 s) left: secondary flux reference; bottom left: secondary flux response

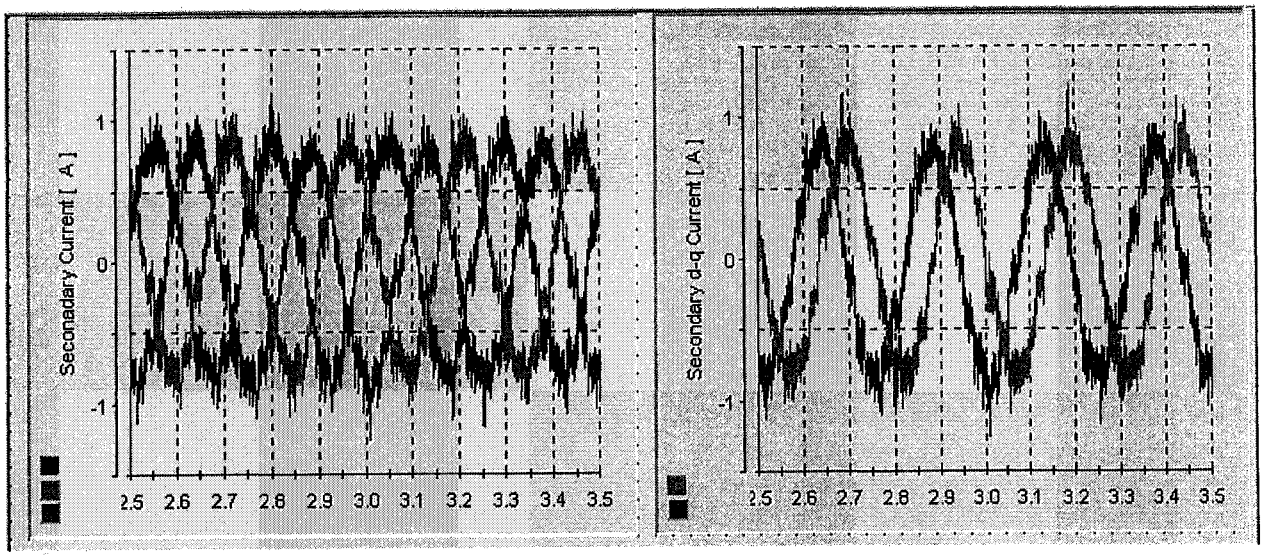

Figure 8.8 The secondary current under control. Left: three-phase currents; right: d-q components of secondary current, d-axis current is in red.

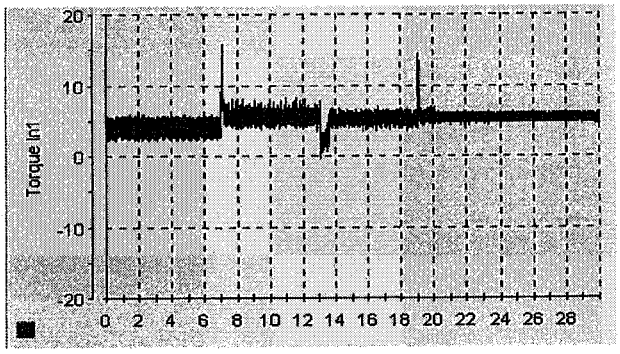

Figure 8.9 Torque response on speed control

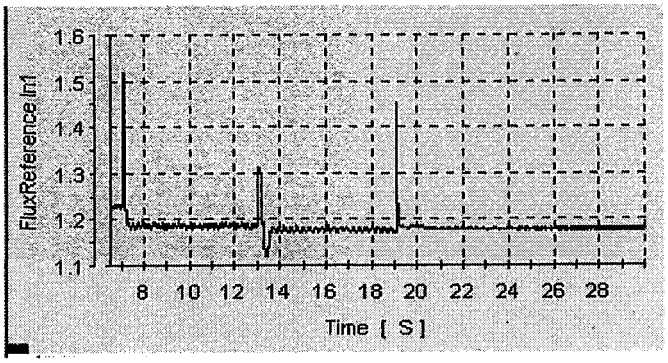

Figure 8.10 reference value for secondary flux

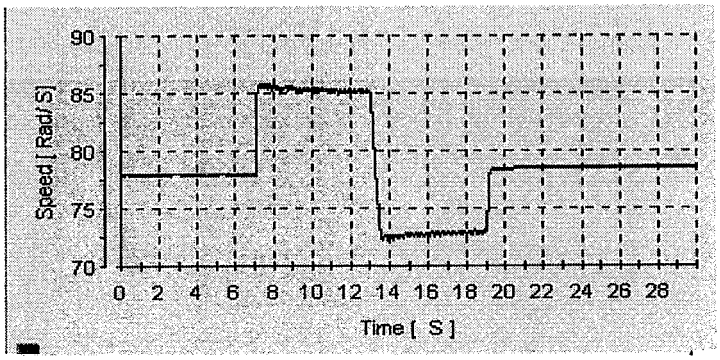

Figure 8.11 the corresponding speed running above, below and at synchronous speed

Figure 8.12 The current in different states

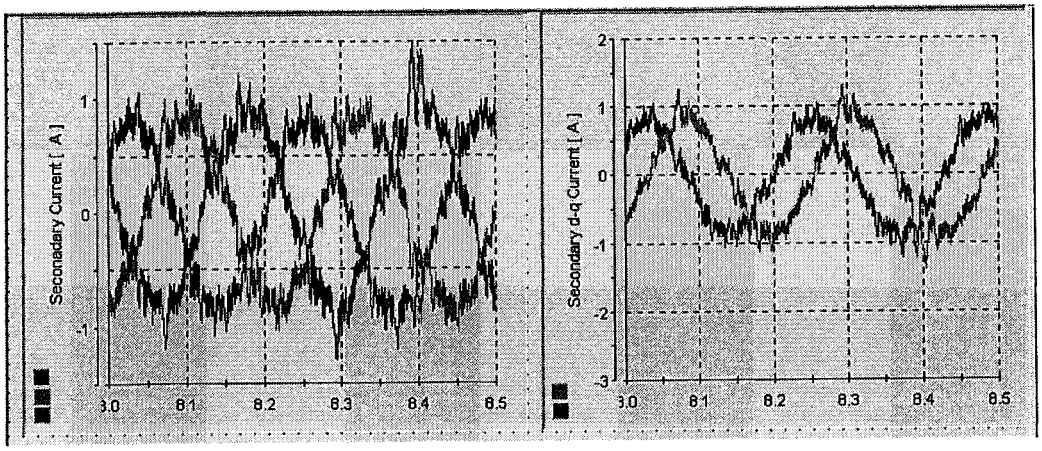

status I: positive secondary current d-axis component is in advance of q-axis component

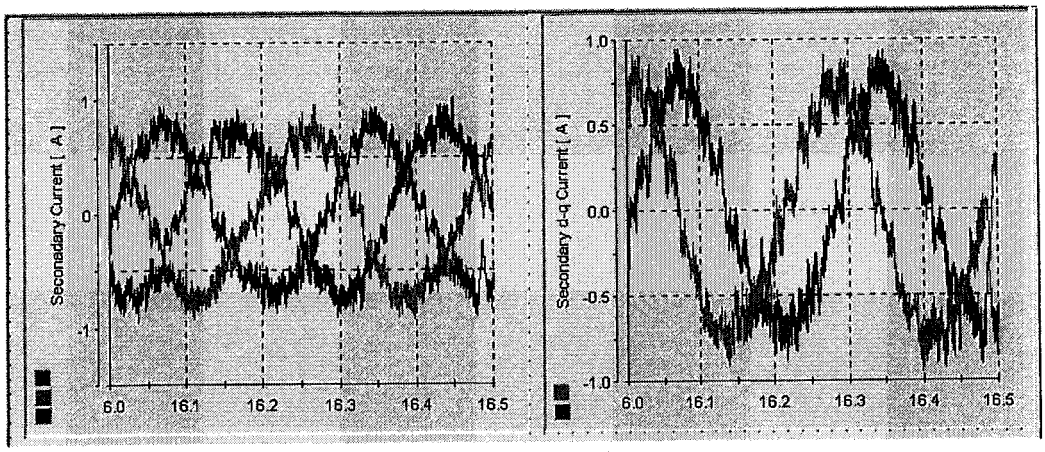

status II: negative secondary frequency when rotor speed is below synchronous speed

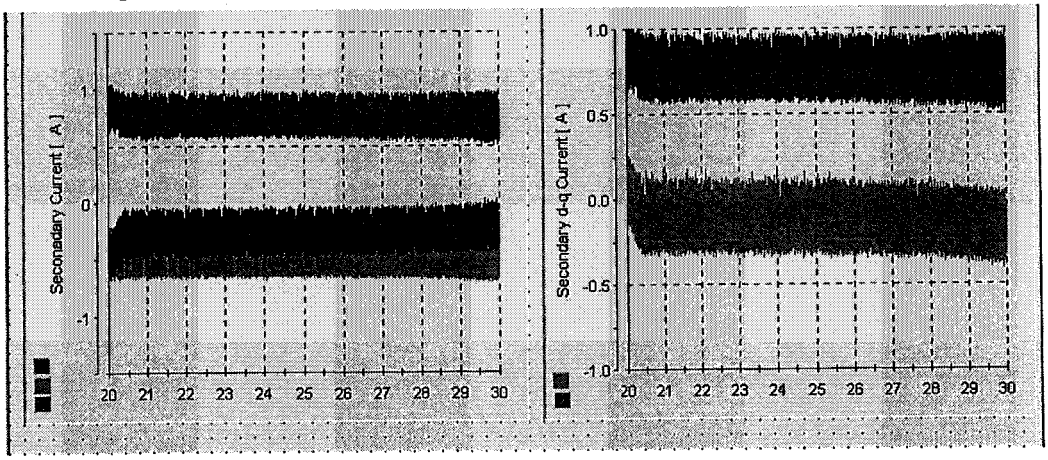

Status III: direct current in secondary when rotor speed is at synchronous speed